

Final Report  
on

**Liquid-Propellant Droplet Dynamics and Combustion in Supercritical  
Forced-Convective Environments**

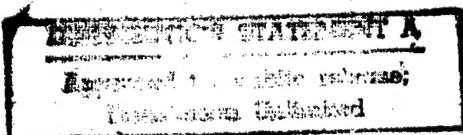
for  
AFOSR Contract/Grant F49620-95-1-0193

Prepared by

Vigor Yang  
Propulsion Engineering Research Center  
and  
Department of Mechanical Engineering  
The Pennsylvania State University  
University Park, PA 16802

Submitted to:

Air Force Office of Scientific Research  
Bolling Air Force Base  
Washington D.C.



August 1998

19980824 181

**REPORT DOCUMENTATION PAGE**

Public reporting burden for this collection of information is estimated to average 1 hour per response, including the time for reviewing instructions, searching existing data sources, gathering the data needed, and completing and reviewing this collection of information. Send comments regarding this burden estimate or any other aspect of this collection of information, including suggestions for reducing this burden to Washington Headquarters Services, Directorate for Information Operations and Reports, 1215 Jefferson Davis Highway, Suite 1204, Arlington, VA 22202-4302, and to the Office of Management and Budget, Paperwork Reduction Project (0704-0188), Washington, DC 20503.

0585

<b>1. AGENCY USE ONLY (Leave blank)</b>		<b>2. REPORT DATE</b> August 10, 1998	<b>3. REPORT TYPE AND DATES COVERED</b> Final Technical Report, 03/01/95-02/28/98	
<b>4. TITLE AND SUBTITLE</b> Liquid-Propellant Droplet Dynamics and Combustion in Supercritical Forced-Convective Environments			<b>5. FUNDING NUMBERS</b> PE-61102F PR-2308 SA-AS G-F49620-95-1-0193	
<b>6. AUTHOR(S)</b> Vigor Yang				
<b>7. PERFORMING ORGANIZATION NAME(S) AND ADDRESS(ES)</b> The Pennsylvania State University 104 Research Building East University Park, PA 16802			<b>8. PERFORMING ORGANIZATION REPORT NUMBER</b>	
<b>9. SPONSORING / MONITORING AGENCY NAME(S) AND ADDRESS(ES)</b> Dr. Mitat A.. Birkan AFOSR/NA 110 Duncan Avenue, Suite 115 Bolling AFB, DC 20332-0001			<b>10. SPONSORING / MONITORING AGENCY REPORT NUMBER</b>	
<b>11. SUPPLEMENTARY NOTES</b>				
<b>12a. DISTRIBUTION / AVAILABILITY STATEMENT</b> Approved for public release; distribution is unlimited			<b>12b. DISTRIBUTION CODE</b>	
<b>13. ABSTRACT (Maximum 200 Words)</b>  A focused research has been conducted to investigate the dynamic behavior of liquid-propellant droplets in supercritical forced-convective environments. The purpose is to establish a solid theoretical basis for enhancing the understanding of liquid-propellant droplet vaporization, combustion, and dynamics at supercritical conditions, with emphasis placed on the effect of forced convection. A variety of liquid propellants and propellant simulants, including hydrocarbon and cryogenic fluids, at both steady and oscillatory conditions were treated systematically. The formulation is based on the full conservation equations for both gas and liquid phases, and accommodates variable properties and finite-rate chemical kinetics. Full account is taken of thermodynamic non-idealities and transport anomalies at high pressures, as well as liquid-vapor phase equilibria for multi-component mixtures. Because the model allows for solutions from first principles, a systematic examination of droplet behavior over wide ranges of temperature and pressure is made possible. Results have not only enhanced the basic understanding of the problem, but also served as a basis for establishing droplet vaporization and combustion correlations for the study of liquid rocket engine combustion, performance, and stability.				
<b>14. SUBJECT TERMS</b> high-pressure combustion, rocket engines, droplet vaporization and combustion, combustion instability			<b>15. NUMBER OF PAGES</b> 170	
			<b>16. PRICE CODE</b>	
<b>17. SECURITY CLASSIFICATION OF REPORT</b> UNCLASSIFIED	<b>18. SECURITY CLASSIFICATION OF THIS PAGE</b> UNCLASSIFIED	<b>19. SECURITY CLASSIFICATION OF ABSTRACT</b> UNCLASSIFIED	<b>20. LIMITATION OF ABSTRACT</b> UL	

## SUMMARY

A focused research program has been conducted to investigate the dynamic behavior of liquid-propellant droplets in supercritical forced-convective environments. The purpose is to establish a solid theoretical basis for enhancing the understanding of liquid-propellant droplet vaporization, combustion, and dynamics at supercritical conditions, with emphasis placed on the effect of forced convection. A variety of liquid propellants and propellant simulants, including hydrocarbon and cryogenic fluids, at both steady and oscillatory conditions are treated systematically. The formulation is based on the full conservation equations for both gas and liquid phases, and accommodates variable properties and finite-rate chemical kinetics. Full account is taken of thermodynamic non-idealities and transport anomalies at high pressures, as well as liquid-vapor phase equilibria for multi-component mixtures. Because the model allows for solutions from first principles, a systematic examination of droplet behavior over wide ranges of temperature and pressure is made possible.

The work represents a series of fundamental studies of liquid-propellant droplet dynamics and combustion at supercritical conditions. Results have not only enhanced the basic understanding of the problem, but can also be used to improve the predictive capabilities of contemporary rocket-engine performance and stability codes. In particular, correlations of droplet mass, momentum, and energy transfer rates over broad ranges of thermodynamic and flow conditions are established for use in the study of spray combustion. Dynamic responses of droplet vaporization and combustion to ambient pressure and velocity oscillations are also treated. The resultant combustion response functions serve as a primary factor in determining the stability characteristics of a rocket engine.

Throughout the program, close collaboration with various experimental groups at the PSU Propulsion Engineering Research Center and the Air Force Research Laboratory is maintained, so that optimal benefit from all efforts are obtained.

## TECHNICAL DISCUSSION

Liquid-droplet vaporization and combustion in supercritical environments have long been matters of serious practical concern in combustion technology, mainly due to the necessity of developing high-pressure combustion devices such as liquid-propellant rocket engines, diesel engines and liquid propellant guns. Although several studies have been devoted to this problem, a number of fundamental issues regarding the attainability of critical conditions and droplet gasification and burning mechanisms at high pressures remain unresolved. Most of the existing theories are based on certain assumptions and empirical correlations that are extrapolated from atmospherical conditions, with their validity for high-pressure applications subject to clarification. Furthermore, no unified analysis of the entire droplet history, in particular the transition from the subcritical to supercritical state, was conducted. Almost all of the models for supercritical combustion have assumed *a priori* that the droplet reaches its critical state instantaneously upon introduction into a supercritical environment. Neither initial heatup transients nor nonuniformities of liquid-phase properties are considered. In addition, the treatment of transport properties and thermodynamics nonidealities is overly simplified to yield complete information. Recent reviews of this subject are given in Refs. 1-4.

The physical model treated here is an isolated liquid-propellant droplet (or an array of droplets) when suddenly confronted with a supercritical fluid flow. The initial temperature of the droplet is subcritical. As the droplet is heated by the ambient gas, its temperature increases and finally exceeds the critical point. Several important aspects must be noted during this process. First, when the droplet surface approaches its thermodynamic critical state, the difference in density between gas and liquid phases becomes smaller. The characteristic times of the transport processes near the droplet surface in both phases have the same order of magnitude. Therefore, the transient effects in the gas phase are as important as those in the liquid phase, and the quasi-steady condition may never be reached during the lifetime of the droplet. Second, the latent heat of vaporization decreases to zero at the critical point. Conventional low-pressure models may erroneously predict the vaporization rate if the variation of latent heat with pressure



is not properly taken into account. In addition, if the droplet is moving, the behavior of liquid deformation and breakup may be altered considerably due to the diminished value of surface tension. Third, at high pressures, effects of thermodynamic non-idealities and property variations play decisive roles in determining transport properties and interfacial thermodynamic relationships. The solubility of the ambient gas in the liquid phase increases with pressure, and the classical Raoult's law for ideal mixtures is not applicable for phase-equilibrium analysis. One must develop a more comprehensive model for vapor-liquid interface conditions in terms of fugacity. Finally, when the droplet exceeds its critical state, it essentially becomes a "puff" of dense fluid. The entire field becomes a continuous medium, and no distinct interfacial boundary can be identified.

The primary purpose of this research project is to establish a theoretical framework within which various issues of supercritical droplet vaporization and combustion can be addressed systematically. Specific tasks conducted include:

1. investigation of supercritical droplet vaporization and combustion in steady convective environments; and
2. study of dynamic responses of droplet vaporization and combustion to ambient flow oscillations.

Major results obtained from these tasks are summarized below.

### **1. Supercritical Droplet Vaporization and Combustion in Steady Convective Environments**

Several comprehensive theoretical analyses have been established to investigate droplet vaporization and combustion in forced convective environments at supercritical conditions. Both hydrocarbon and cryogenic propellant droplets are considered over a pressure range from one to 400 atm. Specific processes treated in this task are:

1. complete time history of droplet gasification, including the transition from the subcritical to supercritical state;
2. ignition and flame development;
3. droplet dynamics, including deformation, stripping, and shattering; and

#### 4. interphase transport between droplet and surrounding flow.

Figure 1 shows the time evolution of the critical surfaces of liquid oxygen (LOX) droplets under various flow conditions at  $p=100$  atm. Owing to the difference between mass and thermal diffusivity, the surface which attains the critical mixing temperature usually regresses faster than that with the critical mixing composition. The dynamic deformation of the droplet is substantially enhanced by increasing the momentum carried by the ambient flow. The effect of pressure on the evolution of the critical surfaces is illustrated in Fig. 2. In addition to enhanced droplet deformation, entrainment of gasified oxygen into the recirculating eddies in the wake region is augmented with increasing pressure. At  $p=400$  atm, the isocomposition skirt even exhibits oscillatory motion. The gaseous oxygen entrapped by the recirculating flow tends to move forward and drives the skirt to expand in the cross stream direction. The convective flow, on the other hand, suppresses this lateral expansion and forces the skirt to bend the stretch downstream. As a result, more oxygen is trapped into the recirculating eddies, leading to another locomotion. Detailed discussions of this phenomenon are given in Refs. 5 and 6.

## 2. Dynamic Responses of Droplet Vaporization and Combustion to Ambient Flow Oscillations

The dynamic responses of supercritical droplet vaporization and combustion to ambient flow oscillations have been examined [7-9]. The analysis extends the droplet combustion model established for steady environments, and accommodates periodic pressure and velocity fluctuations in the ambience. The oscillatory characteristics of droplet gasification and burning mechanisms are studied in detail over a broad range of pressure. Results indicate that the droplet response functions (both pressure- and velocity-coupled responses) increase progressively with pressure due to reduced thermal inertial at high pressures. Furthermore, a rapid amplification of droplet vaporization/combustion response occurs when the droplet surface reaches its critical mixing point. This phenomenon may be attributed to the strong sensitivities of latent

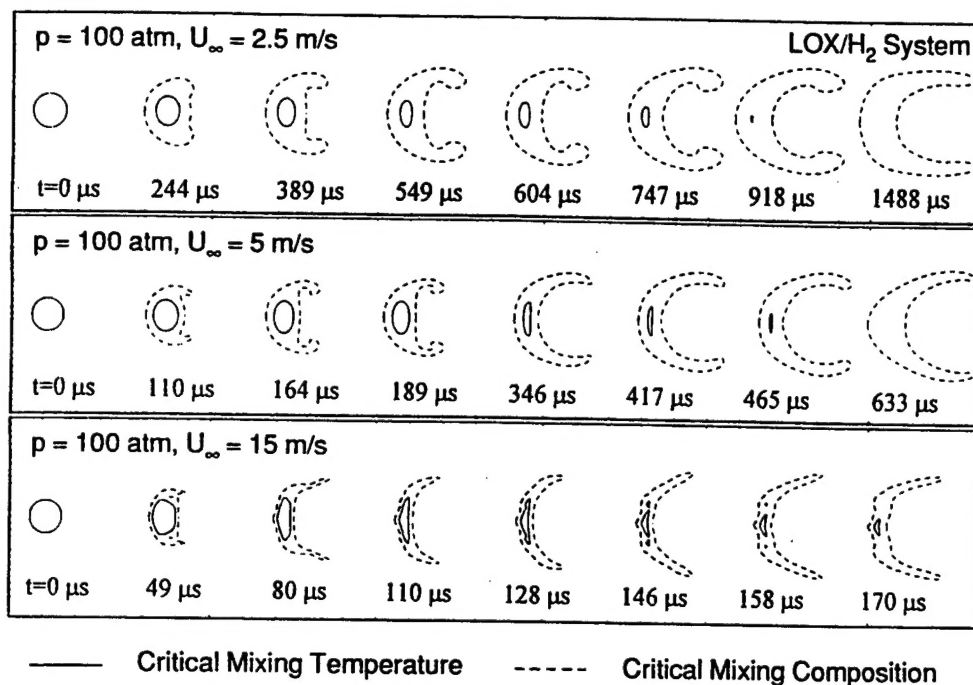


FIGURE 1. Effect of Ambient Velocity on Evolution of Droplet Surface, LOX / H<sub>2</sub> System at p = 100 atm.

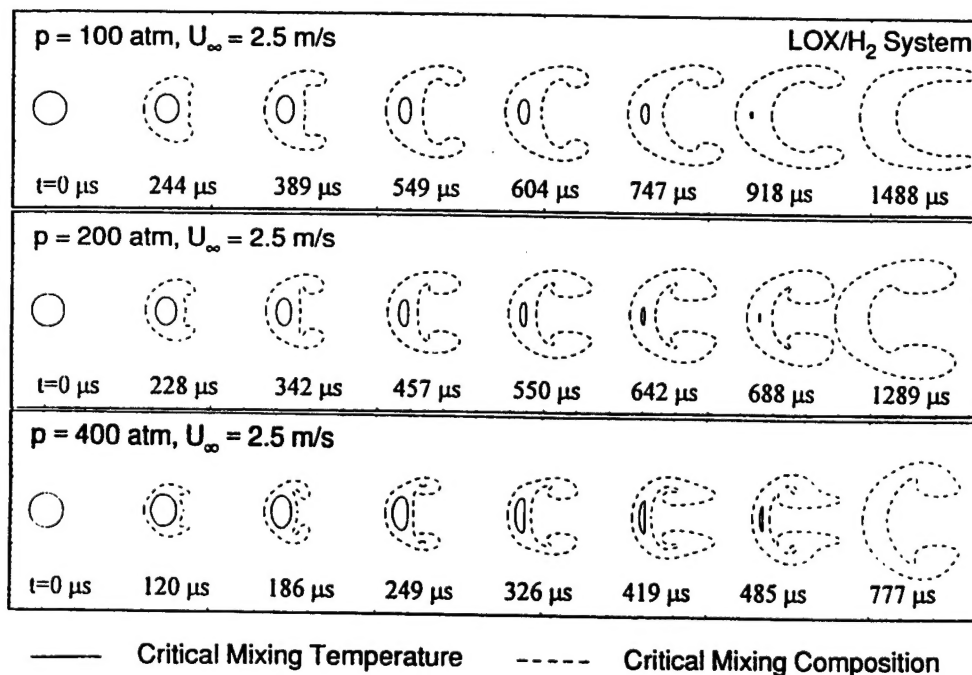


FIGURE 2. Effect of Ambient Pressure on Evolution of Droplet Critical Surface, LOX / H<sub>2</sub> System at U<sub>∞</sub> = 2.5 m/s.

heat of vaporization and fluid transport properties to small perturbations near the critical point.

In addition to basic investigation into the thermophysical processes involved, correlations of droplet response functions are established in terms of droplet and oscillatory flow properties. This information can be effectively used in liquid rocket engine combustion instability analysis.

## REFERENCES

- [1]. Hsieh, K.C., Shuen, J.S., and Yang, V. (1991). Droplet Vaporization in High Pressure Environment. I: Near Conditions. *Combustion Science and Technology*, 76, 111.
- [2]. Shuen, J.S., Yang, V., and Hsiao, G.C. (1992). Combustion of Liquid-Fuel Droplets at Supercritical Conditions. *Combustion and Flame*, 89, 299.
- [3]. Yang, V., Lin, N.N., and Shuen, J.S. (1994). Vaporization of Liquid Oxygen (LOX) Droplets in Supercritical Hydrogen Environments. *Combustion Science and Technology*, 97, 247.
- [4]. Yang, V., Lafon, P., Hsiao, G.C., Habiballah, M., and Zhuang, F. (1995). Liquid-Propellant Droplet Vaporization and Combustion. *Proceedings of 2nd International Symposium on Liquid Rocket Propulsion*, Châtillon, France.
- [5]. Yang, V., Hsiao, G.C., and Shuen, J.S. (1996). Droplet Behavior at Supercritical Conditions. Chapter 17, *Recent Advances in Spray Combustion*, AIAA Progress in Astronautics and Aeronautics Series, Vol. 166, 413.
- [6]. Hsiao, G.C., Yang, V., and Shuen, J.S. (1998). Gasification of Liquid Oxygen Droplets in Supercritical Hydrogen Streams. Submitted to *Journal of Fluid Mechanics*.
- [7]. Lafon, P., Yang, V., and Habiballah, M. (1998). Supercritical Vaporization of Liquid Oxygen Droplets in Hydrogen and Water Environments. Submitted to *Journal of Fluid Mechanics*.
- [8]. Lafon, P., Yang, V., and Habiballah, M. (1998). Pressure-Coupled Vaporization and Combustion Responses of Liquid Oxygen (LOX) Droplets in Supercritical Hydrogen Environments. AIAA Paper 95-2432, also submitted to *Journal of Propulsion and Power*.
- [9]. Hsiao, G.C., Yang, V., and Shuen, J.S. (1998). Pressure-Coupled Vaporization Response of Liquid Hydrocarbon Droplets at High Pressures. Submitted to *Journal of Propulsion and Power*.

## PUBLICATIONS

The present work has led to several archival publications as follows. The manuscripts of the technical papers are given in the Appendices.

### Book

1. Habiballah, M., Popp, M., and Yang, V., (eds.), *Liquid Rocket Combustion Devices: Aspects of Modeling, Analysis, and Design*, Proceedings of 2nd International Symposium on Liquid Rocket Propulsion, Châtillon, France, June 19-21, 1995.

### Book Chapters

2. Yang, V., Hsiao, G.C., and Shuen, J.S., "Droplet Behavior at Supercritical Conditions," Chapter 17, *Recent Advances in Spray Combustion (Vol. I)*, Progress in Astronautics and Aeronautics, Vol. 166, 1996, pp. 413-437.
3. Yang, V., Lafon, P., Hsiao, G.C., and Zhuang, F., "Liquid-Propellant Droplet Vaporization and Combustion," Chapter 7, *Liquid Rocket Combustion Devices: Aspects of Modeling, Analysis, and Design*, Progress in Astronautics and Aeronautics, 1999.

### Technical Papers

4. Hsiao, G.C., Yang, V., and Shuen, J.S., "Gasification of Liquid Oxygen Droplets in Supercritical Hydrogen Streams," submitted to *Journal of Fluid Mechanics*, 1998.
5. Lafon, P., Yang, V., and Habiballah, M., "Supercritical Vaporization of Liquid Oxygen Droplets in Hydrogen and Water Environments," submitted to *Journal of Fluid Mechanics*, 1998.
6. Lafon, P., and Yang, V., "Effect of Pressure on Hydrocarbon Fuel Droplet Vaporization," submitted to *International Journal of Heat and Mass Transfer*, 1998.
7. Lafon, P., and Yang, V., "Droplet Vaporization at Thermodynamic Non-equilibrium Conditions," submitted to *International Journal of Heat and Mass Transfer*, 1998.
8. Lafon, P., Yang, V., and Habiballah, M., "Pressure-Coupled Vaporization and Combustion Responses of Liquid Oxygen (LOX) Droplets in Supercritical Hydrogen Environments," AIAA Paper 95-2432, also submitted to *Journal of Propulsion and Power*, 1998.

## APPENDICES

1. Habiballah, M., Popp, and Yang, V., *Liquid Rocket Combustion Devices: Aspects of Modeling, Analysis, and Design*, Proceedings of 2nd International Symposium on Liquid Rocket Propulsion, Châtillon, France, June 19-21, 1995.
2. Hsiao, G.C., Yang, V., and Shuen, J.S. (1998). Gasification of Liquid Oxygen Droplets in Supercritical Hydrogen Streams. Submitted to *Journal of Fluid Mechanics*.
3. Lafon, P., Yang, V., and Habiballah, M., "Supercritical Vaporization of Liquid Oxygen Droplets in Hydrogen and Water Environments," submitted to *Journal of Fluid Mechanics*, 1998.
4. Lafon, P., and Yang, V., "Effect of Pressure on Hydrocarbon Fuel Droplet Vaporization," submitted to *International Journal of Heat and Mass Transfer*, 1998.
5. Lafon, P. and Yang, V., "Droplet Vaporization at Thermodynamic Non-Equilibrium Conditions," submitted to *Journal of Fluid Mechanics*, 1998.
6. Lafon, P., Yang, V., and Habiballah, M. "Pressure-Coupled Vaporization and Combustion Responses of Liquid Oxygen (LOX) Droplets in Supercritical Hydrogen Environments," AIAA Paper 95-2432, also submitted to *Journal of Propulsion and Power*, 1998.



# **LIQUID ROCKET COMBUSTION DEVICES**

## **Aspects of Modeling, Analysis, and Design**

**Edited by**

**M. Habiballah, M. Popp, and V. Yang**

**Proceedings of the Second International Symposium on Liquid  
Rocket Propulsion**

**ONERA - Châtillon, France  
June 19 - 21, 1995**



# LIQUID ROCKET COMBUSTION DEVICES

## Aspects of Modeling, Analysis, and Design

### Edited by

Vigor Yang  
Pennsylvania State University  
111 Research Building East  
University Park, PA 16802  
U.S.A.

Mohammed Habiballah  
ONERA  
Direction de l'Energétique  
BP 72  
92322 Châtillon Cedex  
FRANCE

Michael Popp  
DASA Space Transportation and  
Propulsion  
Dept. RIT72  
PO Box 801168  
81663 Muenchen  
GERMANY

### Section 1. Injection and Atomization Processes

1. **Propellant Injection Systems and Processes**  
*J. Ito, Aerojet, USA*
2. **Atomization of Coaxial-Jet Injectors**  
*M. Ledoux, Caré, CORIA, France; M. Micci, M. Glogowski, Penn State, USA; L. Vingert, P. Gicquel, ONERA, France*
3. **Atomization of Impinging-Liquid Jets**  
*W. Anderson, Penn State, USA; P. Berthoumieu, ONERA/CERT, France; C. Huang, The 11th Research Institute of China Aerospace Corporation, China; R. Lecourt, ONERA/CFM, France; N. Yatsuyanagi, NAL, Japan; N. Zhu, The 11th Research Institute of China Aerospace Corporation, China*
4. **Dynamics of Liquid Rocket Injectors**  
*V. Bazarov, Moscow State Aviation Institute, Russia*

### Section 2. Droplet Vaporization and Spray Combustion

5. **Modeling of Liquid-Propellant Combustion in Rocket Engine Combustor**  
*To be determined*
6. **Liquid-Propellant Droplet Vaporization and Combustion**  
*V. Yang, P. Lafon, C.C. Hsiao, Penn State, USA; M. Habiballah, ONERA, France; F. Zhuang, China*
7. **Droplet Cluster Behavior in Dense and Dilute Regions of a Spray**  
*J. Bellan, JPL, USA*
8. **Modeling of Turbulent Mixing in Liquid-Propellant Spray**  
*C. Chen, UAH, USA; Y. Chen, H. Shang, ESI, USA; S. Jeng, UC, USA*
9. **Spray Combustion in Storable-Propellant Rocket Motors**  
*D. Preclik, DASA, Germany; D. Estublier, DASA Consultant, Germany; D. Wennerberg, Battelle, Germany; O. de Bonn, DASA, Germany*
10. **Experimental Investigation of Liquid Propellant Spray Combustion**  
*O. Haidn, A. Vogel, DLR, Germany; W. Mayer, NAL, Japan; S. Pal, Penn State, USA; E. Gokalp, C. Chauveau, LCSR, France*
11. **Propellant Ignition and Flame Propagation**  
*E. Hurlbert, R. Moreland, NASA JSC, USA; S. Candel, ECP-EM2C, France*

### Section 3. Thrust Chamber Performance and Heat Transfer

#### 12. Assessment of Thrust Chamber Performance

*D. Coats, SEA, USA; K. Denisov, NIICHIMMASH, RUSSIA; N. Girard, CNES, France*

#### 13. Numerical Analysis of Combustor and Nozzle Flows

*C. Merkle, S. Venkateswaran, Penn State, USA; P. Liang, Rocketdyne, USA; M. Onofri, F. Nasuti, University of La Sapienza, Italy*

#### 14. Thrust Chamber Cooling and Heat Transfer

*S. Fisher, Rocketdyne, USA; M. Popp, DASA, Germany; D. Quentmeyer, NASA LeRC, USA*

### Section 4. Experimental Diagnostics and Testing

#### 15. Planar Laser Diagnostics in the Early Stages of a Burning Spray with Substitute Fluids

*D. Stepowski, A. Cessou, R. Bazile, CORIA, France*

#### 16. Laser Diagnostics for Cryogenic Propellant Combustion Studies

*U. Brummund, A. Cessou, M. Oschwald, A. Vogel, DLR, Germany; F. Grish, P. Bouchardy, M. Péalat, L. Vingert, M. Habiballah, ONERA, France; R. Snyder, G. Herding, P. Scouflair, C. Rolon, S. Candel, ECP-EM2C, France*

#### 17. Scaling Techniques in Liquid Rocket Engine Combustion Devices Testing

*C. Dexter, M. Fisher, NASA MSFC, USA; J. Hulka, Aerojet, USA; K. Denisov, A. Shibanov, A. Agrkov, NIICHIMMASH, RUSSIA*

### Section 5. Design and Development

#### 18. Thermodynamic Power Cycles of Liquid Rocket Engines

*R. Parsley, Pratt & Whitney, USA; B. Zhang, China; P. Pempie, CNES, France*

#### 19. Combustion Devices Design and Optimization

*D. Herbeaux, D. Sion, SEP, France*

#### 20. Advanced Nozzle Technology for Cryogenic Engines

*P. Vuillermoz, CNES, France; C. Weiland, DASA, Germany; B. Aupoix, ONERA/CERT, France; H. Grosdemange, SEP, France; M. Bigert, Volvo, Sweden*

#### 21. Tripropellant Liquid Rocket Engine Technology

*N. Gontcharov, V. Orlov, V. Rachuk, M. Rudis, A. Shostak, CADB, Russia; M. McIlwain, R. Starke, J. Hulka, Aerojet, USA*

#### 22. Oxidizer-Rich Preburner Technology for Full Flow Cycle Applications

*R. Jensen, S. Farhangi, L. Tuegel, T. Roberts, Rocketdyne, USA*

# **GASIFICATION OF LIQUID OXYGEN DROPLETS IN SUPERCRITICAL HYDROGEN STREAMS**

By G. C. HSIAO<sup>1</sup>, V. YANG<sup>1</sup> AND J. S. SHUEN<sup>2</sup>

<sup>1</sup>Department of Mechanical Engineering, The Pennsylvania State University, PA 16802, U.S.A.

<sup>2</sup>U.S. Department of Energy, Richland Operations Office, Richland, WA 99352, U.S.A.

(Received 29 February 1996)

The gasification and dynamics of an isolated liquid oxygen (LOX) droplet in a supercritical hydrogen stream has been numerically studied based on the complete conservation equations. The approach employs a state-of-the-art treatment of thermophysical properties, and accommodates thermodynamic nonideality and transport anomaly at high pressure. The analysis allows for a rigorous investigation into droplet behavior over broad ranges of pressure and Reynolds number. Detailed flow structures and transport phenomena are examined to reveal various key mechanisms underlying droplet gasification in a supercritical, forced-convective environment. In addition, correlations of droplet lifetime and drag coefficient are established in terms of fluid thermodynamic state, Reynolds number, and gasification transfer number.

## **Nomenclature**

$a$	Acceleration of droplet center of gravity
$B$	Spalding transfer number
$B_D$	Transfer number for drag correlation
$C_D$	Drag coefficient
$C_p$	Constant-pressure specific heat
$D$	Molecular diameter
$E, F$	Convective-flux vectors in axial and radial directions, respectively

$E_v, F_v$	Diffusion-flux vectors in axial and radial directions, respectively
$e$	Specific internal energy
$e_t$	Specific total internal energy
$\mathcal{F}$	Scaling factor for transport property
$f, \hbar$	Scaling factors for corresponding state principle
$h$	Specific enthalpy
$k_{ij}, \ell_{ij}$	Binary interaction constants for energy and volume, respectively
$M$	Droplet mass or molecular weight
$N$	Number of species
$p$	Pressure
$q_e$	Energy diffusion flux
$q_{m,i}$	Mass diffusion flux of species $i$
$Q$	Dependent variable vector
$r$	Radial coordinate
$R$	Universal gas constant
$R_c$	Radius of mass-equivalent sphere
$Re$	Reynolds number
$S$	Source vector
$t$	Time
$T$	Temperature
$u, v$	Velocities in axial and radial directions, respectively
$U_{drop}$	Velocity of droplet center of gravity
$v$	Specific volume
$x$	Axial coordinate
$V$	Molar volume

$\mathcal{X}$	Correction factor for noncorrespondence
$X_i$	Mole fraction of species $i$
$Y_i$	Mass fraction of species $i$
$Z$	Compressibility
$\hat{Z}$	Pseudo-time variable vector

#### Greek Symbols

$\beta$	Scaling factor for pseudo-time variable
$\Gamma$	Preconditioning matrix
$\Delta\lambda$	Dense-fluid correction for thermal conductivity
$\Delta\mu$	Dense-fluid correction for viscosity
$\xi, \eta$	Generalized coordinates
$\theta$	Shape factor for energy
$\lambda$	Thermal conductivity
$\mu$	Viscosity
$\rho$	Density
$\tau$	Shear stress tensor or pseudo time
$\tau_f$	Droplet lifetime
$\phi$	Shape factor for molecular size
$\omega$	Pitzer's acentric factor

#### Subscripts

0	Reference fluid or initial condition
<i>big</i>	Large molecule
<i>c</i>	Critical condition

<i>drop</i>	Droplet
<i>i</i>	Species <i>i</i>
<i>l</i>	Averaged quantity of liquid droplet
<i>m</i>	Mixture
<i>r</i>	Reduced thermodynamic property
<i>s</i>	Droplet surface
<i>small</i>	Small molecular
$\infty$	Ambient flow

#### Superscripts

<i>crit</i>	Critical enhancement
<i>exc</i>	Dense fluid correction
<i>T</i>	Transpose of vector
*	Reduced by value at critical point
0	Ideal gas property or hard sphere
-	Vector in generalized coordinates

## 1. Introduction

Supercritical droplet gasification and combustion have long been of serious concern in the development of high-pressure combustion devices such as diesel engines, liquid rocket engines, and gas turbines. Most of previous studies (e.g., Hsieh *et al.* 1991; Shuen *et al.* 1992; Yang *et al.* 1994; Lafon 1995; Lafon *et al.* 1996) focused on droplet behavior at quiescent conditions. Effects of free-stream velocity on droplet gasification and dynamics in forced-convective environments have not yet been addressed in detail. The present work attempts to conduct a comprehensive investigation into supercritical liquid oxygen (LOX) droplet gasification in a hydrogen stream. The approach is based on a state-of-the-art treatment of thermodynamic and transport properties, and allows for a rigorous analysis from first principles. Various fundamental issues associated with droplet dynamics and related transport phenomena at high pressures are examined systematically, with emphasis placed on the distinct characteristics of cryogenic fluids.

In the first part of this study, a series of calculations are carried out to investigate LOX droplet gasification in hydrogen over broad ranges of pressure (100-400 atm) and Reynolds number (2.5-300). Detailed flow structures and transport phenomena are examined to reveal various underlying mechanisms involved in supercritical droplet gasification. Secondly, correlations of mass and momentum transfer rates between droplet and free stream are established in terms of fluid thermodynamic state, Reynolds number, and gasification transfer number. Results can be effectively used as a physical submodel for high-pressure spray combustion analyses.

## 2. Theoretical Formulation

The physical model of interest includes an isolated LOX droplet in a hydrogen stream, as shown in Fig. 1. The initial droplet temperature is uniformly distributed at a subcriti-

cal value, but the ambient hydrogen pressure and temperature are in the thermodynamic supercritical regime of oxygen. Owing to the cryogenic fluid property of oxygen, the droplet surface reaches its thermodynamic critical-mixing state almost instantaneously upon introduction into the hydrogen flow. Once this occurs, the enthalpy of vaporization and surface tension vanish. The entire flowfield (including both the droplet interior and surrounding gases) becomes essentially a continuous medium, and no well-defined liquid/gas interfacial boundary exists <sup>in the case</sup> for a subcritical droplet. The temperature and density, as well as their spatial gradients, vary smoothly throughout the domain from the liquid core to the far field. As a consequence, a single-phase fluid model is used herein to facilitate the analysis.

The flowfield is assumed to be laminar and axisymmetric. If body forces and thermal radiation are ignored, the conservation laws of mass, momentum, energy, and species concentration can be written in the following vector form.

$$\frac{\partial Q}{\partial t} + \frac{\partial(E - E_v)}{\partial x} + \frac{\partial(F - F_v)}{\partial r} = S \quad (2.1)$$

The conservative-variable vector  $Q$  is defined as

$$Q = r(\rho, \rho u, \rho v, \rho e_t, \rho Y_i)^T \quad (2.2)$$

where superscript  $T$  denotes the transpose of vector. The physical properties  $\rho$ ,  $(u, v)$ , and  $Y_i$  are the density, velocity components in the axial and radial directions, and mass fraction of species  $i$ , respectively. The specific total internal energy is written as

$$e_t = h - \frac{p}{\rho} + \frac{1}{2}(u^2 + v^2) \quad (2.3)$$



where  $h$  denotes the specific enthalpy and  $p$  the pressure. The convective-flux vectors,  $E$  and  $F$ , in the axial and radial directions, respectively, take the forms

$$E = r \left( \rho u, \rho u^2 + p, \rho uv, (\rho e_t + p)u, \rho u Y_i \right)^T \quad (2.4)$$

$$F = r \left( \rho v, \rho uv, \rho v^2 + p, (\rho e_t + p)v, \rho v Y_i \right)^T \quad (2.5)$$

The corresponding diffusion-flux vectors are

$$E_v = r \left( 0, \tau_{xx}, \tau_{xr}, u\tau_{xx} + v\tau_{xr} + (q_e)_x, (q_{m,i})_x \right)^T \quad (2.6)$$

$$F_v = r \left( 0, \tau_{xr}, \tau_{rr}, u\tau_{xr} + v\tau_{rr} + (q_e)_r, (q_{m,i})_r \right)^T \quad (2.7)$$

where the normal stresses ( $\tau_{xx}$  and  $\tau_{rr}$ ) and shear stresses ( $\tau_{xr}$  and  $\tau_{rx}$ ) are

$$\tau_{xx} = 2\mu \frac{\partial u_x}{\partial x} - \frac{2}{3}\mu \left[ \frac{\partial u_x}{\partial x} + \frac{1}{r} \frac{\partial}{\partial r}(ru_r) \right] \quad (2.8)$$

$$\tau_{rr} = 2\mu \frac{\partial u_r}{\partial r} - \frac{2}{3}\mu \left[ \frac{\partial u_x}{\partial x} + \frac{1}{r} \frac{\partial}{\partial r}(ru_r) \right] \quad (2.9)$$

$$\tau_{xr} = \tau_{rx} = \mu \left[ \frac{\partial u_x}{\partial r} + \frac{\partial u_r}{\partial x} \right] \quad (2.10)$$

The energy and mass diffusion terms ( $q_e$  and  $q_{m,i}$ ) are calculated using Fourier's and Fick's laws, respectively. The source vector  $S$  results from the axisymmetric geometry and can be written as

$$S = \left( 0, 0, p - \tau_{\theta\theta}, 0, 0 \right)^T \quad (2.11)$$

where

$$\tau_{\theta\theta} = 2\mu \frac{u_r}{r} - \frac{2}{3}\mu \left[ \frac{\partial u_r}{\partial x} + \frac{1}{r} \frac{\partial}{\partial r}(ru_r) \right] \quad (2.12)$$

### 3. Property Evaluation

One major challenge in the analysis of supercritical droplet behavior is the establishment of a unified property evaluation scheme capable of treating thermophysical properties of pure substances and mixtures over the entire fluid thermodynamic state from compressed liquid to dilute gas. At high pressures, models normally used to represent ideal-gas behavior may encounter significant difficulties. From the microscopic point of view, the intermolecular mean free paths tend to decrease with increasing pressure, and consequently the molecular volume and intermolecular forces are no longer negligible as in the case for idealized fluids. For convenience, each property may be expressed as the sum of an ideal-gas property at the same temperature and a thermodynamic departure function which takes into account the dense-fluid correction.

In the current study, a modified Benedict-Webb-Rubin (BWR) equation of state proposed by Jacobsen and Stewart (1973) is used to represent the fluid  $p$ - $V$ - $T$  behavior due to its superior performance over conventional cubic equations of state (Prausnitz *et al.* 1986). This equation of state has been extremely valuable in correlating both liquid and vapor thermodynamic and volumetric data; however, the temperature constants involved are available only for a limited number of pure substances (Cooper *et al.* 1967; Orye 1969; Perry *et al.* 1984). To overcome this constraint, an extended corresponding-state (ECS) principle (Ely & Hanley 1981, 1983) is used herein. The basic idea is to assume that the properties of a single-phase fluid can be evaluated via conformal mappings of temperature and density to those of a given reference fluid. As a result, only the BWR constants for the reference fluid are needed. For a multicomponent system, accounting for changes in properties due to mixing is much more complicated. A pseudo pure-substance model is adopted to evaluate the properties of a mixture, treating the mixture as a single-phase pure substance with its own set of properties evaluated via the ECS

principle. This method improves prediction accuracy and requires only limited data (i.e., critical properties and Pitzer's acentric factor) for each constituent component.

Successful application of the corresponding-state argument for the evaluation of fluid p-V-T properties also encourages similar improvement in the prediction of thermophysical data. In the following, a brief summary of the corresponding-state method in conjunction with the mixture combining rule is first given, followed by the BWR equation of state for the reference fluid. Finally, the techniques for evaluating thermodynamic and transport properties are addressed.

### 3.1. *Extended Corresponding-State Principle*

The extended corresponding-state model of Ely and Hanley (1981, 1983) is used to evaluate volumetric and transport properties of a mixture over its entire thermodynamic fluid state. The scheme assumes that the configurational properties (such as temperature, density, viscosity, thermal conductivity, etc.) of a single-phase mixture can be equated to those of a hypothetical pure fluid, which are then evaluated via corresponding states with respect to a given reference fluid. For example, the viscosity of a mixture,  $\mu_m$ , can be related to that of a reference fluid,  $\mu_0$ , at the corresponding thermodynamic state as

$$\mu_m(\rho, T) = \mu_0(\rho_0, T_0) \mathcal{F}_\mu \quad (3.1)$$

where  $\mathcal{F}_\mu$  represents the mapping function. The correspondence of temperature and density between the mixture of interest and the reference fluid (denoted respectively by subscripts  $m$  and  $0$ ) can be characterized by the following two scaling factors.

$$f_m = \frac{T}{T_0} \quad ; \quad h_m = \frac{\rho_0}{\rho} \quad (3.2)$$

The former represents the conformation of potential distribution of energy, while the latter characterizes the effect of mixture molecular size. Assuming that all components

in a mixture obey the ECS principle, the mixing rules for a multi-component system can be expressed as

$$\begin{aligned}\bar{h}_m &= \sum_i^N \sum_j^N X_i X_j \bar{h}_{ij} \\ f_m &= \bar{h}_m^{-1} \sum_i^N \sum_j^N X_i X_j f_{ij} \bar{h}_{ij}\end{aligned}\quad (3.3)$$

where  $N$  is the number of species and  $X_i$  the mole fraction of species  $i$ . The two binary scaling factors,  $f_{ij}$  and  $\bar{h}_{ij}$ , are defined as

$$\begin{aligned}f_{ij} &= (f_i f_j)^{1/2} (1 - k_{ij}) \\ \bar{h}_{ij} &= \frac{1}{8} (\bar{h}_i^{1/3} + \bar{h}_j^{1/3})^3 (1 - \ell_{ij})\end{aligned}\quad (3.4)$$

where  $k_{ij}$  and  $\ell_{ij}$  are binary interaction parameters reflecting the effects of energy and molecular size, respectively. In order to model the quantum behavior of hydrogen, interaction parameters for a hydrogen-containing mixture are specially treated by a generalized correlation proposed by Valderrama and Reyes (1983).

$$\begin{aligned}k_{ij} &= A - B/T_j^* \\ \ell_{ij} &= 1 + 0.07 \ln[(D_{big}/D_{small})]\end{aligned}\quad (3.5)$$

and

$$\begin{aligned}[D_{big}/D_{small}] &= [V_{c,big}/V_{c,small}]^{1/3} \\ A &= 0.1805 + 3.21\omega_j + 2.437\omega_j^2 \\ B &= 0.1323 + 0.5507\omega_j + 3.5994\omega_j^2\end{aligned}\quad (3.6)$$

where  $[D_{big}/D_{small}]$  is always greater than 1 and  $V_c$  is the critical molar volume. The variable  $T^*$  is the reduced temperature and  $\omega$  Pitzer's acentric factor. The subscripts  $i$  and  $j$  denote the hydrogen and non-hydrogen components, respectively.

The scaling factors ( $f_i$  and  $h_i$ ) for each individual component can be obtained by a two-parameter corresponding state principle (Ely & Hanley 1981, 1983).

$$\begin{aligned} f_i &= (T_{c,i}/T_{c,0}) \theta_i(T_i^*, V_i^*, \omega_i) \\ h_i &= (V_{c,i}/V_{c,0}) \phi_i(T_i^*, V_i^*, \omega_i) \end{aligned} \quad (3.7)$$

where  $T_c$  is the critical temperature, and  $\theta_i$  and  $\phi_i$  are the so-called shape factors which are functions of Pitzer's acentric factor ( $\omega_i$ ) and reduced temperature and molar volume ( $T_i^*$  and  $V_i^*$ ). The analytical expressions for  $\theta_i$  and  $\phi_i$  proposed by Leach *et al.* (1968) take the forms

$$\begin{aligned} \theta_i(T_i^*, V_i^*, \omega_i) &= 1 + (\omega_i - \omega_0) F(T_i^*, V_i^*) \\ \phi_i(T_i^*, V_i^*, \omega_i) &= [1 + (\omega_i - \omega_0) G(T_i^*, V_i^*)] Z_{c,0}/Z_{c,i} \end{aligned} \quad (3.8)$$

where  $Z$  is the compressibility factor. The variables  $F$  and  $G$  are

$$\begin{aligned} F(T_i^*, V_i^*) &= a_1 + b_1 \ln T_i^+ (c_1 + d_1/T_i^+) (V_i^+ - 0.5) \\ G(T_i^*, V_i^*) &= a_2(V_i^+ + b_2) + c_2(V_i^+ + d_2) \ln T_i^+ \end{aligned} \quad (3.9)$$

$$\begin{aligned} T_i^+ &= \min\{2, \max\{T_i^*, 0.5\}\} \\ V_i^+ &= \min\{2, \max\{V_i^*, 0.5\}\} \end{aligned} \quad (3.10)$$

where constants  $a_i$ ,  $b_i$ ,  $c_i$ , and  $d_i$  are coefficients for shape-factor correlations.

## 3.2. Equation of State

Under the assumption of the ECS principle, the density of a mixture can be evaluated by

$$\rho_m(T, p) = \frac{\rho_0(T_0, p_0)}{\hat{h}_m(T, p)} \quad (3.11)$$

where  $\rho_0$ ,  $T_0$ , and  $p_0$  denote the corresponding density, temperature, and pressure of the reference fluid, respectively. Since the temperature at the conformal state is calculated by Eq. (3.2), the corresponding pressure can be derived based on the general compressibility theory (i.e.,  $Z=Z(T^*, \rho^*)$ ),

$$p_0 = p \left( \frac{\hat{h}_m}{f_m} \right) \quad (3.12)$$

To ensure the accuracy of the density prediction, a generalized BWR equation of state (Jacobsen & Stewart 1973) is adopted for the reference fluid.

$$p_0(T, \rho) = \sum_{n=1}^9 a_n(T) \rho^n + \sum_{n=10}^{15} a_n(T) \rho^{2n-17} e^{-\gamma \rho^2} \quad (3.13)$$

where  $\gamma$  is 0.04, and the temperature coefficients  $a_i(T)$  depend on the reference fluid of concern.

Although this equation of state must be solved iteratively for density at given pressure and temperature, the prediction covers wide ranges of thermodynamic states, and as such promotes the establishment of a unified evaluation scheme of thermophysical properties. Figure 2 shows the comparison of oxygen density between experimental data (Sychev *et al.* 1987) and the prediction by the BWR equation of state in conjunction with the ECS principle. The reference fluid is selected as propane herein due to the availability of sufficiently reliable data correlated over a wide range of experimental conditions. The result

shows excellent agreement over the entire fluid state, from compressed liquid to dilute gas. Figure 3 presents the relative errors of density prediction based on three commonly used equations of state, namely, the Benedict-Webb-Rubin (BWR), Peng-Robinson (PR), and Soave-Redlich-Kwong (SRK). The ECS principle is embedded into the evaluation procedure of the BWR equation of state and shows its superior performance with the maximum relative error at 1.5% for the pressure and temperature ranges under consideration. On the other hand, the SRK and PR equations of state yield maximum errors around 13% and 17%, respectively.

### 3.3. Thermodynamic Properties

Thermodynamic properties are of vital importance in the analysis of supercritical droplet behavior. Variations in these properties can often be related to local fluid properties of pressure, temperature, and species concentration. Properties like enthalpy, internal energy, and specific heat of a mixture are expressible as the sum of the ideal-gas property and a correction term accounting for thermodynamic nonideality.

$$h = h^0 + \left\{ \int_{\infty}^v \left[ T \left( \frac{\partial p}{\partial T} \right)_v - p \right] dv + RT(Z - 1) \right\} \quad (3.14)$$

$$e = e^0 + \left\{ \int_{\infty}^v \left[ T \left( \frac{\partial p}{\partial T} \right)_v - p \right] dv \right\} \quad (3.15)$$

$$C_p = C_p^0 + \left\{ \int_{\infty}^v T \left( \frac{\partial^2 p}{\partial T^2} \right)_v dv - T \left( \frac{\partial p}{\partial T} \right)_v^2 / \left( \frac{\partial p}{\partial v} \right)_T - R \right\} \quad (3.16)$$

where superscripts 0 refer to ideal-gas properties. The second terms on the right sides of Eqs. (3.14)-(3.16) denote the thermodynamic departure functions, and can be obtained from the equation of state described previously.

## 3.4. Transport Properties

Estimation of viscosity and thermal conductivity can be made by means of the corresponding-state method described in Sec. 3.1. The corresponding-state argument for the viscosity of a mixture can be written in its most general form as

$$\mu_m(\rho, T) = \mu_0(\rho_0, T_0) \mathcal{F}_\mu \chi_\mu \quad (3.17)$$

The quantity  $\chi_\mu$  is a correction factor accounting for the effect of noncorrespondence. Its magnitude is always close to unity, based on the modified Enskog theory (Ely 1981). The scaling factor  $\mathcal{F}_\mu$  takes the form

$$\mathcal{F}_\mu = (M_m/M_0)^{\frac{1}{2}} f_m^{\frac{1}{2}} \bar{h}_m^{-\frac{2}{3}} \quad (3.18)$$

where  $M_0$  is the molecular weight of the reference fluid, and the value of the mixture denoted by  $M_m$  can be evaluated by

$$M_m = \bar{h}_m^{-8/3} f_m^{-1} \left[ \sum_{i=1}^N \sum_{j=1}^N X_i X_j \bar{h}_{ij}^{4/3} f_{ij}^{1/2} M_{ij}^{1/2} \right]^2 \quad (3.19)$$

The scaling factors  $f_m$ ,  $\bar{h}_m$ ,  $f_{ij}$ , and  $\bar{h}_{ij}$  follow the same definitions in Eqs. (3.2) and (3.4). A binary mixing rule is used for the molecular weight.

$$M_{ij} = 2M_i M_j / (M_i + M_j) \quad (3.20)$$

where  $M_i$  is the molecular weight of component  $i$ .

Because of the lack of a complete molecular theory for describing transport properties over a broad regime of fluid phases, it is generally accepted that viscosity and thermal conductivity be divided into three contributions and correlated in terms of density and



temperature (Vesovic & Wakeham 1991). For instance, the viscosity of the reference fluid is written as follows.

$$\mu_0(\rho_0, T_0) = \mu_0^0(T_0) + \Delta\mu_0^{exc}(\rho_0, T_0) + \Delta\mu_0^{crit}(\rho_0, T_0) \quad (3.21)$$

The first term on the right-hand side represents the value in the dilute-gas limit, which is independent of density and can be accurately predicted by kinetic-theory equations (Ely & Hanley 1981, 1983). The second term is the excess viscosity which, with the exclusion of unusual variations near the critical point, characterizes the deviation from  $\mu_0$  for a dense fluid. The third term refers to the critical enhancement which accounts for the anomalous increase above the background viscosity (i.e., the sum of  $\mu_0^0$  and  $\Delta\mu_0^{exc}$ ) as the critical point is approached. However, the theory of nonclassical critical behavior predicts that, in general, properties that diverge strongly in pure fluids near the critical points will diverge only weakly in mixtures due to the different physical criteria for criticality in a pure fluid and a mixture (Levelt Sengers 1991). Because the effect of critical enhancement is not well-defined for a mixture and is likely to be small, the third term  $\Delta\mu_0^{crit}$  is not considered in the existing analyses of supercritical droplet gasification.

Evaluation of thermal conductivity must be carefully conducted for two reasons: (1) the one-fluid model must ignore the contribution of diffusion to conductivity, and (2) the effect of internal degrees of freedom on thermal conductivity cannot be correctly taken into account by the corresponding-state argument. As a result, thermal conductivity of a pure substance or mixture is generally divided into two contributions (Ely & Hanley 1983),

$$\lambda_m(\rho, T) = \lambda'_m(T) + \lambda''_m(\rho, T) \quad (3.22)$$

The former,  $\lambda'_m(T)$ , arises from transfer of energy via the internal degrees of freedom,

while the latter,  $\lambda''_m(\rho, T)$ , is due to the effects of molecular collision or translation. For a mixture,  $\lambda'_m(T)$  can be evaluated by a semi-empirical mixing rule.

$$\lambda'_m(T) = \sum_i \sum_j X_i X_j \lambda'_{ij}(T) \quad (3.23)$$

where  $\lambda'_{ij}$  is a binary thermal conductivity defined as

$$\lambda'_{ij}(T)^{-1} = 2 \left[ \lambda'_i(T)^{-1} + \lambda'_j(T)^{-1} \right] \quad (3.24)$$

The internal contribution of component  $i$  is calculated by the modified Eucken correlation (Ely & Hanley 1983) for polyatomic gases as

$$\lambda'_i(T) = 1.32 \frac{\mu_i^0}{M_i} \left( C_{p,i}^0 - \frac{5}{2} R \right) \quad (3.25)$$

where the properties,  $\mu_i^0$ ,  $R$ , and  $C_{p,i}^0$ , are the dilute-gas viscosity, gas constant, and ideal-gas heat capacity of component  $i$ , respectively. The collisional/translational contribution,  $\lambda''_m(\rho, T)$ , is evaluated via the extended corresponding-state method.

$$\lambda''_m(\rho, T) = \lambda''_0(\rho_0, T_0) \mathcal{F}_\lambda \chi_\lambda \quad (3.26)$$

where  $\mathcal{F}_\lambda$  is the scaling factor identical to that used in Eq. (3.18) for mixture viscosity. A small correction factor  $\chi_\lambda$  is used to compensate the noncorrespondent behavior of the mixture, and can be estimated using the modified Enskog theory and fluid p-V-T properties. The quantity  $\lambda''_0(\rho_0, T_0)$  is the equivalent contribution for the reference fluid at the corresponding state, which can be further divided into three parts:

$$\lambda''_0(\rho_0, T_0) = \lambda_0^*(T) + \Delta\lambda_0^{exc}(\rho_0, T_0) + \Delta\lambda_0^{crit}(\rho_0, T_0) \quad (3.27)$$

where  $\lambda_0^*(T)$  is the value in the dilute-gas limit,  $\Delta\lambda_0^{exc}$  the excess thermal conductivity,

and  $\Delta\lambda_0^{crit}$  the critical enhancement. Since the effect of the anomalous variation of thermal conductivity appears to be small for a mixture near its critical locus, the account for critical enhancement,  $\Delta\lambda_0^{crit}$ , is not included in the present work.

Estimation of the binary mass diffusivity for a mixture gas at high density represents a more challenging task than evaluating the other transport properties, due to the lack of a formal theory or even a theoretically based correlation. Takahashi (1974) has suggested a simple scheme for predicting the binary mass diffusivity of a dense fluid by means of a corresponding-state approach. This scheme appears to be the most complete to date, and has demonstrated moderate success in the limited number of tests conducted. The approach proceeds in two steps. First, the binary mass diffusivity of a dilute gas is obtained using the Chapman-Enskog theory in conjunction with the inter-molecular potential function. The calculated data is then corrected in accordance with a generalized chart in terms of reduced temperature and pressure.

#### 4. Numerical Algorithm

Droplet vaporization and combustion typically involve fluid motions in a velocity range from molecular diffusion to low subsonic speed. Contemporary numerical algorithms developed for compressible flows are often ineffective at such a low-velocity condition. There are two well-recognized reasons for this difficulty (Merkle & Choi 1985). First, the eigenvalues of the system become stiff at low flow velocities, thereby adversely affecting the convergence characteristics of numerical solutions. Second, the pressure terms in the momentum equations become singular as the Mach number approaches zero and consequently result in a large round-off error.

In order to circumvent the above computational difficulties, a fully implicit dual time-stepping integration method (Withington *et al.* 1991; Shuen *et al.* 1992) is adopted in the present study. The scheme is established in two steps. First, rescaled pressure

terms are used in the momentum equations to minimize round-off errors at low Mach numbers. The second step incorporates a set of well-conditioned artificial terms into the conservation laws to enhance numerical efficiency and stability. An implicit iterative procedure follows to achieve a converged solution in the pseudo-time domain, which corresponds to a temporal-accurate solution in the physical-time domain. The resulting conservation laws in generalized coordinates  $(\xi, \eta)$  are written as

$$\Gamma \frac{\partial \hat{Z}}{\partial \tau} + \frac{\partial \tilde{Q}}{\partial t} + \frac{\partial(\tilde{E} - \tilde{E}_v)}{\partial \xi} + \frac{\partial(\tilde{F} - \tilde{F}_v)}{\partial \eta} = \tilde{S} \quad (4.1)$$

where  $\tau$  represents the pseudo time. The vectors  $\tilde{Q}$ ,  $\tilde{E}$ ,  $\tilde{E}_v$ ,  $\tilde{F}$ , and  $\tilde{F}_v$  are defined as

$$\begin{aligned} \tilde{Q} &= \frac{\tau}{J} Q \\ \tilde{E} &= \frac{\tau}{J} (\xi_t Q + \xi_x E + \xi_r F) \\ \tilde{E}_v &= \frac{\tau}{J} (\xi_x E_v + \xi_r F_v) \\ \tilde{F} &= \frac{\tau}{J} (\eta_t Q + \eta_x E + \eta_r F) \\ \tilde{F}_v &= \frac{\tau}{J} (\eta_x E_v + \eta_r F_v) \end{aligned} \quad (4.2)$$

where  $J$  is the Jacobian matrix for coordinate transformation. Variables  $\xi_t$  and  $\eta_t$  are the grid-speed terms, and  $\xi_x$ ,  $\xi_r$ ,  $\eta_x$ , and  $\eta_r$  the metric terms. The primitive variable vector,  $\hat{Z}$ , the preconditioning matrix,  $\Gamma$ , and the source term,  $\tilde{S}$ , are expressed as

$$\begin{aligned} \hat{Z} &= \frac{\tau}{J} \begin{pmatrix} p_g \\ u \\ v \\ h \\ Y_1 \end{pmatrix}, \quad \Gamma = \begin{pmatrix} 1/\beta & 0 & 0 & 0 & 0 \\ u/\beta & \rho & 0 & 0 & 0 \\ v/\beta & 0 & \rho & 0 & 0 \\ h/\beta - 1 & \rho u & \rho v & \rho & 0 \\ Y_1/\beta & 0 & 0 & 0 & \rho \end{pmatrix} \\ \tilde{S} &= \frac{1}{J} \begin{pmatrix} 0 \\ -\frac{2}{3}(\xi_x \frac{\partial \mu v}{\partial \xi} + \eta_x \frac{\partial \mu v}{\partial \eta}) \\ p_g - \frac{4}{3} \frac{\mu v}{r} + \frac{2}{3} \mu (\xi_x \frac{\partial u}{\partial \xi} + \eta_x \frac{\partial u}{\partial \eta}) - \frac{2}{3} v (\xi_r \frac{\partial \mu}{\partial \xi} + \eta_r \frac{\partial \mu}{\partial \eta}) \\ -\frac{2}{3} (\xi_x \frac{\partial \mu u v}{\partial \xi} + \eta_x \frac{\partial \mu u v}{\partial \eta} + \xi_r \frac{\partial \mu v^2}{\partial \xi} + \eta_r \frac{\partial \mu v^2}{\partial \eta}) \\ 0 \end{pmatrix} \end{aligned} \quad (4.3)$$

where  $p_g$  and  $\beta$  are the gauge pressure and its scaling factor, respectively.

One significant advantage of the dual time-stepping integration method is that the convergence of the iterative process is determined by the eigenvalue characteristics in the pseudo-time domain, not by the original eigenvalues which become disparate at low flow velocity. This feature allows flexibility in the selection of time step sizes in both time frames. The physical-time step is determined based on the characteristic evolution of the unsteady flow under consideration, while the pseudo-time step depends on the numerical stability of the algorithm and can be adjusted to obtain optimum convergence.

## 5. Results and Discussions

The model described in the preceding sections has been applied to study the gasification characteristics of liquid oxygen (LOX) droplets in supercritical hydrogen streams. The ambient hydrogen temperature is taken to be 1000 K. The initial droplet diameter is 100  $\mu\text{m}$ , and the initial droplet temperature is 100 K, which corresponds to the LOX injection temperature in many operational rocket engines such as the Space Shuttle main engines and the Vulcain engines used in the Ariane 5 launch vehicles. In order to examine the effects of ambient flow conditions on droplet behavior and associated interphase transport, a parametric study covering a wide range of pressure (100–400 atm) and velocity (0.1–15 m/s) is conducted. The solid dots in Fig. 4 mark the scenarios under consideration, with the corresponding free-stream Reynolds number based on the initial droplet diameter ( $Re = U_\infty D_0 / \nu_\infty$ ) shown in the y-axis.

Within the pressure range of the current interest, the droplet initial temperature is slightly lower than the critical mixing temperature of the oxygen/hydrogen system (i.e.,  $T_c = 142.79 \text{ K}$  at  $p = 100 \text{ atm}$ ). Thermodynamic criticality is reached at the droplet surface almost instantaneously upon its introduction to the flow due to rapid heat transfer from the ambient flow (Yang *et al.* 1994, Lafon *et al.* 1996). Once this occurs, both the

liquid and gas phases coexist on the droplet surface at the critical mixing condition. The enthalpy of vaporization and surface tension reduce to zero, and the mixture properties as well as their spatial gradients vary smoothly across the surface. However, the droplet interior still remains at the liquid state with a subcritical temperature distribution. The subsequent gasification process becomes diffusion/convection controlled, and the effect of interfacial thermodynamics diminishes.

Several snapshots of the flowfields under various conditions are presented in Figs. 5-7. Figure 5 shows six frames of isotherms and isopleths of oxygen concentration at a convective velocity of 2.5 m/s and an ambient pressure of 100 atm. The free stream Reynolds number  $Re$  is 30.56 based on the initial droplet diameter. Soon after the introduction of the droplet into the hydrogen stream, the flow adjusts to form a boundary layer near the surface. The gasified oxygen can not accumulate on the front surface of the droplet, and is carried downstream through convection and mass diffusion. The evolution of the temperature field exhibits features distinct from that of the concentration field due to the disparate time scales associated with thermal and mass diffusion processes (i.e., Lewis number  $\neq 1$ ). The thermal wave penetrates into the droplet interior with a pace faster than does the surrounding hydrogen species. Since the liquid core possesses large momentum inertia and moves slower compared with the gasified oxygen, at  $t = 0.79$  ms, the droplet (delineated by the dark region in the temperature contours) reveals an olive shape while the oxygen concentration contours deform into a crescent shape with the edge bent to the streamwise direction. At  $t = 1.08$  ms, the subcritical liquid core disappears, leaving behind a puff of dense oxygen fluid which is convected further downstream with increasing velocity until it reaches the momentum equilibrium with the ambient hydrogen flow.

Figure 6 presents a sequence of droplet evolution as does Fig. 5, but at an ambient

pressure of 400 atm. The effect of pressure on droplet dynamics can be determined by a direct comparison between these two figures. Several distinct phenomena are observed. First, the droplet deformation is enhanced by increasing the ambient pressure. Here, the corresponding Reynolds number is 3.75 times larger than that at 100 atm. The hydrogen stream carries higher momentum and consequently exerts stronger force on the droplet, and as such promotes its deformation. Second, the droplet lifetime decreases with increasing ambient pressure because the higher convective momentum increases the contact surface exposed to the hot stream, thereby facilitating the transfer of thermal energy. Third, the increased ambient pressure advances the gradients of temperature and oxygen concentration. Although the blowing effect due to droplet gasification is stronger in a high-pressure environment, the large momentum transfer reduces the convective resident time and forms a thinner boundary layer near the surface.

Figure 7 depicts a scenario identical to that of Fig. 5, but with an increased convective velocity of 15 m/s. The droplet evolution is substantially different, exhibiting several distinct modes such as deformation, viscous stripping, and breakup. When the droplet is introduced into this strong convective flow ( $Re = 200$ ), fast vorticity generation caused by the velocity difference between the liquid core and ambient flow promotes the formation of an attached eddy behind the droplet and induces a slightly higher pressure region. Meanwhile, the free stream exerts dynamic loading continuously to the front surface. As a result, the droplet deforms and extends in the direction normal to the external flow. The flattened edge then turns to the streamwise direction, stretches downstream, and forms a skirt. The length of the skirt increases with time, and is dictated by the momentum transfer with the ambient flow. At  $t=92 \mu s$ , an annulus of gaseous oxygen is detached from the growing skirt due to the local flow motion and volume dilatation resulting from the penetration of thermal wave into the skirt. The stripped oxygen,

entrained by the recirculating flow, further bends toward the rear surface of the droplet. It carries the momentum from the attached eddy and consequently causes the droplet to deform into a spherical-cape or crescent shape. The associated cusp-like rim may catalyze the vorticity generation and further enhance the strength of the recirculating eddy. Since the viscosity of the droplet interior is greatly reduced by the energy transfer from the hot stream, at certain stage during the droplet lifetime, the liquid oxygen breaks up and forms a secondary ring around its core. Another significant phenomenon is the distribution of oxygen concentration. The gasified oxygen stripped from the edge of the droplet leaves the recirculating region and is swept downstream, forming a cylindrical tail.

Figures 8(a)-(d) summarize the streamline patterns and oxygen concentration contours of the four different modes commonly observed in supercritical droplet gasification. The droplet may either remains in a spherical configuration, deforms to an olive shape, or even breaks up into fragments, depending on the local flow conditions. Unlike low-pressure cases in which the large shear stress at the gas-liquid interface induces internal flow circulation in the liquid core (Prakash & Sirignano 1978,1980), no discernible recirculation takes place in the droplet interior, regardless of the Reynolds number and deformation mode. This may be attributed to the diminishment of surface tension at supercritical conditions. In addition, the droplet regresses so fast that a fluid element in the interphase region may not acquire the time sufficient for establishing an internal vortical flow before it gasifies. The rapid deformation of the droplet configuration further precludes the existence of stable shear stress in the liquid core and consequently obstructs the formation of recirculation.

The spherical mode shown in Fig. 8(a) typically occurs at very low Reynolds numbers. Although flow separation is encouraged by LOX gasification, no recirculating eddy is



found in the wake behind the droplet. The vorticity generated is too weak to form any confined eddy. When the ambient velocity increases to 1.5 m/s, the droplet deforms into an olive shape with a recirculating ring attached behind it, as shown in Fig. 8(b). Owing to the droplet deformation and gasification, the threshold Reynolds number above which the recirculating eddy forms is considerably lower than that for a hard sphere. The latter case requires a minimum Reynolds number of 20 based on the numerical results of LeClair *et al.* (1970) and Dennis *et al.* (1971). Figure 8(c) depicts the flow structure with viscous stripping at an ambient velocity of 5 m/s, showing an oblate droplet with a stretched vortex ring. The flattened edge of the droplet enhances the strength of the recirculating eddies and as such increases the viscous shear stress dramatically. Consequently, a thin sheet of fluid is stripped off from the edge of the droplet and swept toward the outer boundary of the recirculating eddy. At a very high ambient velocity of 15 m/s, droplet breakup takes place, as clearly shown in Fig. 8(d). The hydrogen flow penetrates through the liquid phase, and divides the droplet into two parts: the core disk and surrounding ring. The vortical structure in the wake region expands substantially as a result of the strong shear stress.

Owing to the difference between mass and thermal diffusivity, the critical mixing state cannot be sustained on the droplet surface after the occurrence of thermodynamic criticality. The surface which attains the critical mixing temperature usually regresses faster than that with the critical mixing composition. Fig. 9 shows the temporal evolution of these two types of critical surfaces under various flow conditions at  $p = 100 \text{ atm}$ . The solid lines represent the instantaneous isotherms of the critical mixing temperature, while the dashed lines mark the surfaces of the critical mixing composition. The values of critical mixing properties can be obtained through a phase equilibrium analysis (Yang *et al.* 1994) and are given in Table 1. The dynamic deformation of the droplet

TABLE 1. Critical Mixing Properties of  $O_2/H_2$  System.

	pressure (atm)	critical mixing temperature (K)	critical mixing composition of $O_2$
	100	142.79	0.735
	200	127.21	0.561
	400	116.0	0.496

is substantially enhanced by increasing the momentum carried by the ambient flow. For example, at one half of the droplet lifetime, the droplet aspect ratio based on the surface of the critical mixing temperature (defined as the ratio of the length in the vertical axis to the thickness in the axis of symmetry) increases from 2.1 at  $U_\infty = 2.5 \text{ m/s}$  to 3.2 at  $U_\infty = 5 \text{ m/s}$ . The effect of pressure on the evolution of the critical surfaces is illustrated in Fig. 10. In addition to enhanced droplet deformation, entrainment of gasified oxygen into the recirculating eddies in the wake region is augmented with increasing pressure. At  $p = 400 \text{ atm}$ , the isocomposition skirt even exhibits oscillatory motion. The gaseous oxygen entrapped by the recirculating flow tends to move forward and drives the skirt to expand in the cross stream direction. The convective flow, on the other hand, suppresses this lateral expansion and forces the skirt to bend and stretch downstream. As a result, more oxygen is trapped into the recirculating eddies, leading to another locomotion.

Figure 11 presents the effect of free-stream velocity on the instantaneous variation of droplet residual mass at  $p=100 \text{ atm}$ , defined herein as the mass confined by the isothermal surface at the critical mixing temperature. In a slowly convective stream (e.g.,  $U_\infty = 0.2 \text{ m/s}$ ), heat conduction plays an important role in determining the gasification characteristics. The rapid gasification in the early stage of the droplet lifetime results from the large temperature gradient near the liquid/gas interphase. The gasified oxygen then diffuses outward and hinders the penetration of thermal wave into the droplet, consequently rendering a slower gasification rate. At high Reynolds numbers, enhanced heat

and mass transfer, along with severe droplet deformation caused by the strong dynamic loading from the approaching flow, considerably facilitates the gasification process. The droplet disappears within a much shorter period of time. Figure 12 shows the effect of pressure on droplet gasification behavior. As the pressure increases, the convective heat transfer also increases since the freestream Reynolds number ( $Re = \rho U L / \mu$ ) varies almost linearly with pressure, the viscosity being a weak function of pressure. In addition, the critical mixing temperature used to define the droplet surface decreases with increasing pressure. These two combined effects apparently favor droplet gasification at high pressure.

To summarize the overall effect of ambient flow conditions on droplet lifetime, a simple correlation shown in Fig. 13 is developed as

$$\frac{\tau_f}{\tau_{f, Re=0}} = \frac{1}{1 + 0.166 Re^{1.1} (p_{r, O_2})^{-0.88}} \quad (5.1)$$

where  $Re$  is the Reynolds number based on the initial droplet diameter and  $p_{r, O_2}$  the reduced pressure in reference to the critical pressure of oxygen. Equation 5.1 bears a resemblance to the classical Ranz-Marshall correlation (1952) for droplet vaporization in convective environments, which takes the form

$$\frac{\tau_f}{\tau_{f, Re=0}} = \frac{1}{1 + 0.276 Re^{1/2} Pr^{1/3}} \quad (5.2)$$

The Ranz-Marshall correlation is only applicable to low-pressure conditions, and shows a weaker Reynolds-number dependency.

Because of lack of distinct gas/liquid interface at supercritical conditions, droplet motion is best characterized based on the locus of the center of gravity which can be obtained from the first moment of inertia of the mass confined by the critical mixing-temperature surface in reference to a fixed axis. Figures 14(a) and (b) present the results for various

ambient freestream velocities and pressures, respectively. The droplet travel distance depends on both the net momentum transfer and the time duration over which the force acts on the droplet. For instance, at  $p = 100 \text{ atm}$ , although the convective Reynolds number at  $U_\infty = 5 \text{ m/s}$  is larger than that at  $1.5 \text{ m/s}$ , the droplet moves farther in the low-velocity case, simply due to its longer lifetime.

The motion of a droplet is essentially a result of net momentum transfer to it. Following common practice, the drag coefficient is defined as follows.

$$C_D = \frac{M \frac{dU_{drop}}{dt}}{\frac{1}{2} \rho_\infty (U_\infty - U_{drop})^2 \pi R_c^2} \quad (5.3)$$

where  $(U_\infty - U_{drop})$  is the droplet relative velocity, and  $R_c$  the radius of the mass-equivalent sphere with a uniform distribution of density at its initial value. The denominator in Eq. (5.3) represents the aerodynamic loading. The total drag acting on a droplet includes form, friction, and thrust drag, of which form drag is usually found to be the dominant component (Haywood *et al.* 1989). Thrust drag arising from the momentum transfer with the ambient flow due to evaporation is always negligibly small. Figure 15 presents the time histories of the total drag coefficient, drag force, and aerodynamic loading at  $p = 100 \text{ atm}$  and  $U_\infty = 5 \text{ m/s}$ , where the asterisk denotes the quantity normalized by the initial aerodynamic loading. The early increase in  $C_D$  is caused by the increasing form drag associated with droplet deformation. This effect is then counterbalanced by the strong surface blowing due to gasification which weakens both friction and form drag. The total drag force diminishes to zero at the end of the droplet lifetime.

The drag coefficient of an evaporating droplet is usually smaller than that of a hard sphere at the same Reynolds number (Chen & Yuen, 1976). This phenomenon may be attributed to the modification of the flowfield and transport properties in the vicinity of the droplet surface. The gasification process often leads to a thickened boundary layer,

thereby reducing shear stress and resultant drag. Several researchers (e.g., Renksizbulut & Haywood 1988; Haywood *et al.* 1989; Chiang *et al.* 1992) numerically studied this issue by solving the Navier-Stokes equations for a spherical droplet at low to moderate pressures. No deformation was considered to simplify the analysis. The results lead to the following correlation

$$C_D = \frac{C_D^0}{(1+B)^b} \quad (5.4)$$

where  $C_D^0$  is the reference drag coefficient for a hard sphere (Putnam 1961) and takes the form

$$C_D^0 = \frac{24}{Re} \left[ 1 + \frac{1}{6} Re^{\frac{2}{3}} \right] \quad (5.5)$$

The coefficient  $b$  has a value of 0.2 in Renksizbulut's model (1988) and 0.32 in Chiang's model (1992). The Spalding transfer number defined below is adopted to account for the effect of evaporation on drag coefficient.

$$B = \frac{C_p(T_\infty - T_s)}{\Delta h_v} \quad (5.6)$$

Apparently, the above correlation becomes invalid in the present study of supercritical droplet gasification. The enthalpy of vaporization  $\Delta h_v$  diminishes to zero when the thermodynamic critical state is reached, rendering a singular value of the transfer number.

To establish a generalized correlation for supercritical conditions, the instantaneous drag force was calculated throughout the entire droplet lifetime for all the scenarios under consideration. The data was then correlated through the use of a transfer number  $B_D$  taking into account the rapid transient during the gasification process, defined as

$$B_D = \left( \frac{T_\infty - T_c}{T_c - T_l} \right) \quad (5.7)$$

where  $T_l$  is the instantaneous average temperature of droplet, and  $T_c$  the critical mixing temperature. Since  $B_D$  diverges at  $T_c = T_l$  at the end of droplet lifetime, the calculation of drag force was terminated when  $T_c - T_l$  becomes less than 1 K, at which the droplet residual mass is usually less than one thousandth of the initial mass. The influence on the accuracy of data reduction is quite limited. Following the procedure leading to Eq. (5.4), a correlation shown in Fig. 16 for LOX droplet drag coefficient is obtained.

$$C_D = \frac{C_D^0}{(1 + aB_T)^b} \quad (5.8)$$

where  $a$  and  $b$  are selected to be 0.05 and  $1.592 (p_{r,O_2})^{-0.7}$ , respectively. The data clusters along the classical drag curve, Eq. (5.5), in the low Reynolds-number region, but deviates considerably at high Reynolds numbers (i.e.,  $Re > 10$ ). Although a shape factor may be employed to account for this phenomenon arising from the increased form drag due to droplet deformation, the difficulty of calculating this factor and conducting the associated data analysis precludes its use in correlating the drag coefficient herein. Instead, a simple correction factor  $Re^{0.3}$  is incorporated into Eq. (5.8) to provide the compensation. The final result shown in Fig. 17 is given below.

$$C_D = \frac{C_D^0 Re^{0.3}}{(1 + aB_T)^{1.592 (p_{r,O_2})^{-0.7}}} \quad 0 < Re < 300 \quad (5.9)$$

## 6. Conclusion

Gasification of LOX droplets in supercritical hydrogen streams has been analyzed numerically. The model treats the complete conservation equations in an axisymmetric coordinate, and accommodates thermodynamic nonideality and transport anomaly. The

analysis enables a comprehensive investigation into droplet behavior over a broad range of thermodynamic state. Various key processes involved in droplet gasification in a supercritical, forced-convective environment were identified, including flow structures, droplet dynamics, and interphase transport phenomena. In addition, a parametric study of droplet mass and momentum transfer as a function of ambient pressure (100-400 atm) and Reynolds number (0-300) was conducted. The resultant correlations of droplet lifetime and drag coefficient can be effectively used as a physical submodel in high-pressure spray combustion analyses.

### **Acknowledgement**

This work was sponsored in part by the U.S. NASA Marshall Space Flight Center and in part by the U.S. Air Force Office of Scientific Research. The support and encouragement of Dr. Charles F. Schafer, Mr. Marvin Rocker, and Dr. Mitat A. Birkan were greatly appreciated.

## REFERENCES

- Chen, L. W. & Yuen, M. C., "On Drag of Evaporating Liquid Droplets," *Combustion Science and Technology*, Vol. 14, 1976, pp. 147-154.
- Chiang, C. H., Raju, M. S. & Sirignano, W. A., "Numerical Analysis of Convecting, Vaporizing Fuel Droplets with Variable Properties," *International Journal of Heat and Mass Transfer*, Vol. 35, 1992, pp. 1307-1324.
- Cooper, H. W. & Goldfrank, J. C., "B-W-R Constants and New Correlations," *Hydrocarbon Processing and Petroleum Refiners*, Vol. 46, No. 12, 1967, pp. 141-146.
- Dennis, S. C. R. & Walker, J. D. A., "Calculation of the Steady Flow Past a Sphere at Low and Moderate Reynolds Numbers," *Journal of Fluid Mechanics*, Vol. 48, 1971, pp. 771-789.
- Ely, J. F., "An Enskog Correction for Size and Mass Difference Effects in Mixture Viscosity Prediction," *Journal of Research of the National Bureau of Standards*, Vol. 86, No. 6, 1981, pp. 597-604.
- Ely, J. F. & Hanley, H. J. M., "Predictions of Transport Properties. 1. Viscosity of Fluids and Mixtures," *Industrial and Engineering Chemistry Fundamentals*, Vol. 20, No. 4, 1981, pp. 323-332.
- Ely, J. F. & Hanley, H. J. M., "Predictions of Transport Properties. 2. Thermal Conductivity of Pure Fluids and Mixtures," *Industrial and Engineering Chemistry Fundamentals*, Vol. 22, No. 1, 1983, pp. 90-97.
- Haywood, R. J., Nafziger, R. & Renksizbulut, M., "A Detailed Examination of Gas and Liquid Phase Transient Processes in Convective Droplet Evaporation," *Journal of Heat Transfer*, Vol. 111, 1989, pp. 495-502.
- Hsiao, G. C., *Supercritical Droplet Vaporization and Combustion in Quiescent and Forced-Convective Environments*, Ph.D. Thesis, The Pennsylvania State University, 1995.
- Hsieh, K. C., Shuen, J. S. & Yang, V., "Droplet Vaporization in High-Pressure Environments, I: Near-Critical Conditions," *Combustion Science and Technology*, Vol. 76, 1991, pp. 111-132.
- Jacobsen, R. T. & Stewart, R. B. J., "Thermodynamic Properties of Nitrogen Including Liquid and Vapor Phases from 63K to 2000K with Pressure to 10,000 Bar," *Journal of Physical and Chemical Reference Data*, Vol. 2, No. 4, 1973, pp. 757-922.
- Lafon, P., *Modélisation et Simulation Numérique de L'Evaporation et de la Combustion de Gouttes à Haute Pression*, Ph.D thesis, à L'Université D'Orléans, 1995.
- Lafon, P., Yang, V. & Habiballah, M., "Supercritical Vaporization of Liquid Oxygen in Hydrogen and Water Environments," submitted to *Journal of Fluid Mechanics*, 1996.
- Leach, J. W., Chapple, P. S. & Leland, T. W., "Use of Molecular Shape Factors in Vapor-Liquid Equilibrium Calculations with the Corresponding States Principle," *AIChE Journal*, Vol. 14, No. 4, 1968, pp. 568-576.
- LeClair, B. P., Hamielec, A. E. & Pruppacher, H. R., "A Numerical Study of the Drag on a Sphere at Low and Intermediate Reynolds Numbers," *Journal of the atmospheric sciences*, Vol. 27, 1970, pp. 308-315.
- Levelt Sengers, J. M. H., "Thermodynamics of Solutions Near the Solvent's Critical Point," *Supercritical Fluid Technology*, edited by Bruno, T. J. and Ely, J. F., CRC Press, Boca Raton, Florida, 1991, p. 25.
- Merkle, C. L. & Choi, Y. H., "Computation of Low-Speed Flow with Heat Addition," *AIAA Journal*, Vol. 23, 1987, pp. 831-838.
- Orye, R. V., "Prediction and Correlation of Phase Equilibria and Thermal Properties with the BWR Equation of State," *Industrial and Engineering Chemistry Process Design and Development*, Vol. 8, 1969, pp. 579-588.
- Perry, R. H., Gree, D. W. & Maloney, J. O., *Perry's Chemical Engineers' Handbook*, McGraw-Hill, New York, 1984.
- Prakash, S. & Sirignano, W. A., "Liquid Fuel Droplet Heating and Internal Circulation," *International Journal of Heat and Mass Transfer*, Vol. 21, 1978, pp. 885-895.
- Prakash, S. & Sirignano, W. A., "Theory of Convective Droplet Vaporization with Unsteady Heat Transfer in the Circulating Liquid Phase," *International Journal of Heat and Mass Transfer*, Vol. 23, No. 3, 1980, pp. 253-268.
- Prausnitz, J. M., Lichtenthaler, R. N. & de Azevedo, E. G., *Molecular Thermodynamics of Fluid-Phase Equilibria*, Prentice-Hall, Englewood Cliffs, NJ, 1986.
- Putnam, A., "Integratable Form of Droplet Drag Coefficient," *ARS Journal*, Vol. 31, 1961,



- pp. 1467-1468.
- Ranz, W. E. & Marshall, W. R. "Evaporization from Drops I and II," *Chemical Engineering Progress*, Vol. 48, 1952, pp. 141-146.
- Renksizbulut, M. & Haywood, R. J. "Transient Droplet Evaporation with Variable Properties and Internal Circulation at Intermediate Reynolds Numbers," *Internal Journal of Multiphase Flow*, Vol. 14, No. 2, 1988, pp. 189-202.
- Shuen, J. S., Yang, V. & Hsiao, G. C., "Combustion of Liquid-Fuel Droplets in Supercritical Conditions," *Combustion and Flame*, Vol. 89, 1992, pp. 299-319.
- Shuen, J. S., Chen, K.-H. & Choi, Y., "A Coupled Implicit Method for Chemical Non-equilibrium Flows at All Speeds," *Journal of Computational Physics*, Vol. 106, 1992, pp. 306-318.
- Sychev, V. V., Vasserman, A. A., Kozlov, A. D. & Spiridonov, G. A., "Liquid and Gaseous Oxygen," *Property Data Update*, Vol. 1, No. 3-4, 1987, pp. 529-536.
- Takahashi, S., "Preparation of a Generalized Chart for the Diffusion Coefficients of Gases at High Pressures," *Journal of Chemical Engineering (Japan)*, Vol. 7, 1974, pp. 417-420.
- Valderrama, J. O. & Reyes, L. R., "Vapor-Liquid Equilibria of Hydrogen-Containing Mixtures," *Fluid Phase Equilibria*, Vol. 13, 1983, pp. 195-202.
- Vesovic, V., and Wakeham, W. A., "Transport Properties of Supercritical Fluids and Fluid Mixtures," *Supercritical Fluid Technology*, edited by Bruno, T. J. and Ely, J. F., CRC Press, Boca Raton, Florida, 1991, p. 253.
- Withington, J. P., Shuen, J. S. & Yang, V., "A Time Accurate, Implicit Method for Chemically Reacting Flows at All Mach Numbers," AIAA Paper 91-0581, AIAA 29th Aerospace Sciences Meeting, January, 1991.
- Yang, V., Lin, N. N. & Shuen, J. S., "Vaporization of Liquid Oxygen (LOX) Droplets in Supercritical Hydrogen Environments," *Combustion Science and Technology*, Vol. 97, 1994, pp. 247-270.

## List of Figures

- Fig. 1 Schematic Diagram of Droplet Vaporization in Forced Convective Environment.
- Fig. 2 Comparison of Oxygen Density Predicted by the BWR Equation of State and Measured by Sychev *et al.* (1987).
- Fig. 3 Relative Errors of Density Predictions by Three Different Equations of State, Experimental Data from Sychev *et al.* (1987).
- Fig. 4 Droplet Reynolds Number as a Function of Freestream Velocity and Ambient Pressure;  $LOX/H_2$  System with  $D_0 = 100\mu m$  and  $T_\infty = 1000K$ .
- Fig. 5 LOX Droplet Gasification in Supercritical Hydrogen Flow;  $p = 100$  atm,  $U_\infty = 2.5$  m/s.
- Fig. 6 LOX Droplet Gasification in Supercritical Hydrogen Flow;  $p = 400$  atm,  $U_\infty = 2.5$  m/s.
- Fig. 7 LOX Droplet Gasification in Supercritical Hydrogen Flow;  $p = 100$  atm,  $U_\infty = 15$  m/s.
- Fig. 8 LOX Droplet Gasification in Supercritical Hydrogen Flow at  $p = 100$  atm: (a) Spherical Mode;  $U_\infty = 0.2$  m/s,  $t=0.61$  ms. (b) Deformation Mode;  $U_\infty = 1.5$  m/s,  $t=0.61$  ms. (c) Stripping Mode;  $U_\infty = 5$  m/s,  $t=0.17$  ms. (d) Breakup Mode;  $U_\infty = 15$  m/s,  $t=0.17$  ms.
- Fig. 9 Effect of Ambient Velocity on Evolution of Droplet Critical Surfaces,  $LOX/H_2$  System at  $p = 100$  atm.
- Fig. 10 Effect of Ambient Pressure on Evolution of Droplet Critical Surfaces,  $LOX/H_2$  System at  $U_\infty = 2.5$  m/s.
- Fig. 11 Effect of Ambient Velocity on Time Variation of Droplet Residual Mass;  $LOX/H_2$  System at  $p = 100$  atm.
- Fig. 12 Effect of Ambient Pressure on Time Variation of Droplet Residual Mass;  $LOX/H_2$  System at  $U_\infty = 2.5$  m/s.
- Fig. 13 Correlation of Droplet Lifetime as a Function of Free-Stream Reynolds Number and Pressure.
- Fig. 14 Locus of Droplet Center of Gravity,  $LOX/H_2$  System: (a) Effects of Convective Velocity at  $p = 100$  atm. (b) Effects of Ambient Pressure at  $U_\infty = 2.5$  m/s.
- Fig. 15 Time Variation of Total Drag Force, Aerodynamic Loading, and Drag Coefficient;  $LOX/H_2$  System at  $p=100$  atm and  $U_\infty = 5$  m/s.
- Fig. 16 Effect of Reynolds Number and Pressure on Droplet Drag Coefficient.
- Fig. 17 Correlation of Droplet Drag Coefficient.

## List of Figures

- Fig. 1 Schematic Diagram of Droplet Vaporization in Forced Convective Environment.
- Fig. 2 Comparison of Oxygen Density Predicted by the BWR Equation of State and Measured by Sychev *et al.* (1987).
- Fig. 3 Relative Errors of Density Predictions by Three Different Equations of State, Experimental Data from Sychev *et al.* (1987).
- Fig. 4 Droplet Reynolds Number as a Function of Freestream Velocity and Ambient Pressure;  $LOX/H_2$  System with  $D_0 = 100\mu m$  and  $T_\infty = 1000K$ .
- Fig. 5  $LOX$  Droplet Gasification in Supercritical Hydrogen Flow;  $p = 100$  atm,  $U_\infty = 2.5$  m/s.
- Fig. 6  $LOX$  Droplet Gasification in Supercritical Hydrogen Flow;  $p = 400$  atm,  $U_\infty = 2.5$  m/s.
- Fig. 7  $LOX$  Droplet Gasification in Supercritical Hydrogen Flow;  $p = 100$  atm,  $U_\infty = 15$  m/s.
- Fig. 8  $LOX$  Droplet Gasification in Supercritical Hydrogen Flow at  $p = 100$  atm: (a) Spherical Mode;  $U_\infty = 0.2$  m/s,  $t=0.61$  ms. (b) Deformation Mode;  $U_\infty = 1.5$  m/s,  $t=0.61$  ms. (c) Stripping Mode;  $U_\infty = 5$  m/s,  $t=0.17$  ms. (d) Breakup Mode;  $U_\infty = 15$  m/s,  $t=0.17$  ms.
- Fig. 9 Effect of Ambient Velocity on Evolution of Droplet Critical Surfaces,  $LOX/H_2$  System at  $p = 100$  atm.
- Fig. 10 Effect of Ambient Pressure on Evolution of Droplet Critical Surfaces,  $LOX/H_2$  System at  $U_\infty = 2.5$  m/s.
- Fig. 11 Effect of Ambient Velocity on Time Variation of Droplet Residual Mass;  $LOX/H_2$  System at  $p = 100$  atm.
- Fig. 12 Effect of Ambient Pressure on Time Variation of Droplet Residual Mass;  $LOX/H_2$  System at  $U_\infty = 2.5$  m/s.
- Fig. 13 Correlation of Droplet Lifetime as a Function of Free-Stream Reynolds Number and Pressure.
- Fig. 14 Locus of Droplet Center of Gravity,  $LOX/H_2$  System: (a) Effects of Convective Velocity at  $p = 100$  atm. (b) Effects of Ambient Pressure at  $U_\infty = 2.5$  m/s.
- Fig. 15 Time Variation of Total Drag Force, Aerodynamic Loading, and Drag Coefficient;  $LOX/H_2$  System at  $p=100$  atm and  $U_\infty = 5$  m/s.
- Fig. 16 Effect of Reynolds Number and Pressure on Droplet Drag Coefficient.
- Fig. 17 Correlation of Droplet Drag Coefficient.

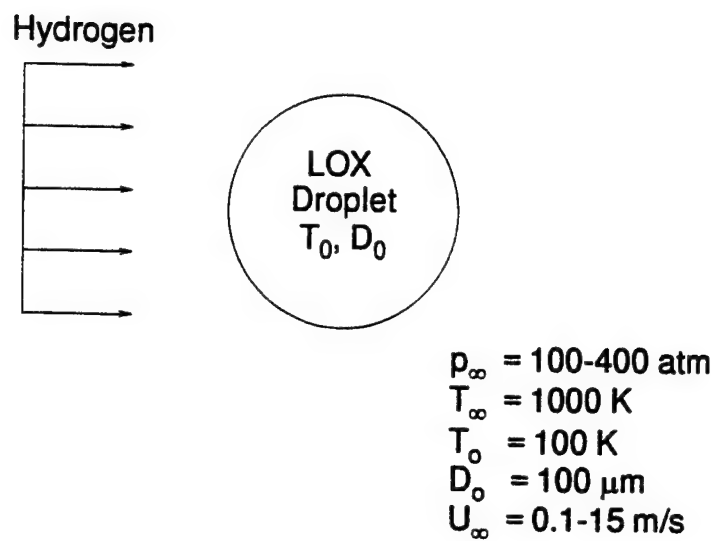


FIGURE 1. Schematic Diagram of Droplet Vaporization in Forced Convective Environment.

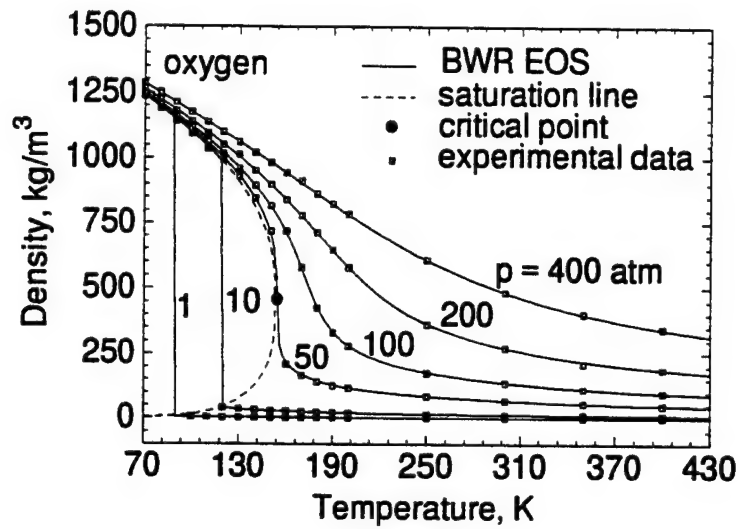


FIGURE 2. Comparison of Oxygen Density Predicted by the BWR Equation of State and Measured by Sychev *et al.* (1987).

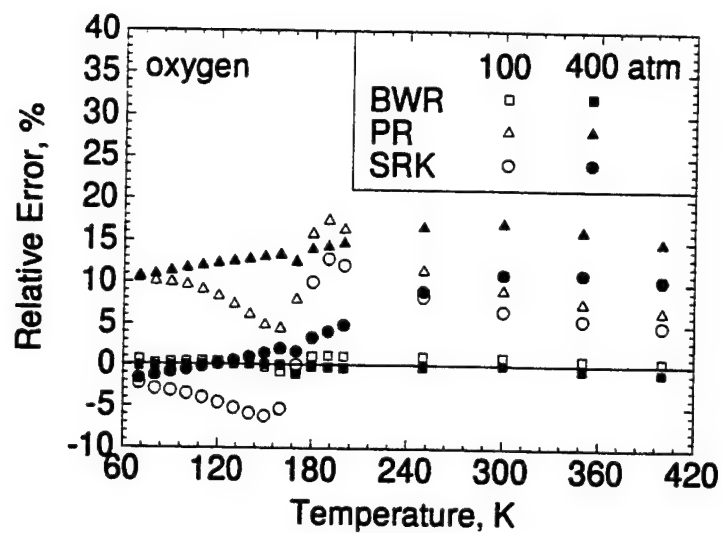


FIGURE 3. Relative Errors of Density Predictions by Three Different Equations of State, Experimental Data from Sychev *et al.* (1987).

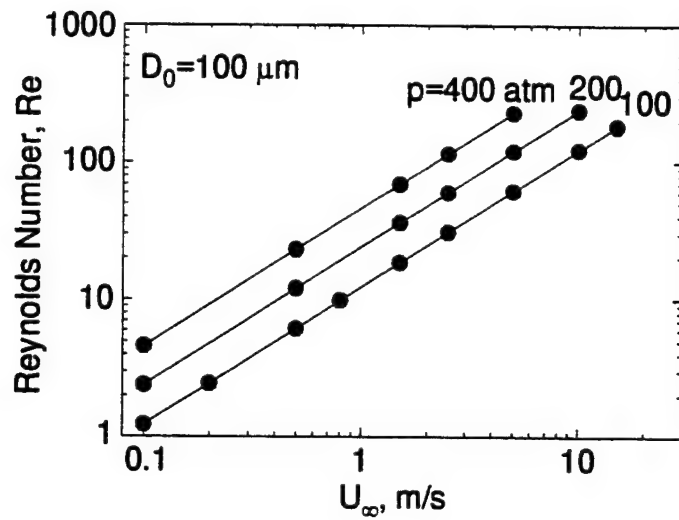


FIGURE 4. Droplet Reynolds Number as a Function of Freestream Velocity and Ambient Pressure; LOX/H<sub>2</sub> System with  $D_0 = 100 \mu\text{m}$  and  $T_\infty = 1000\text{K}$ .

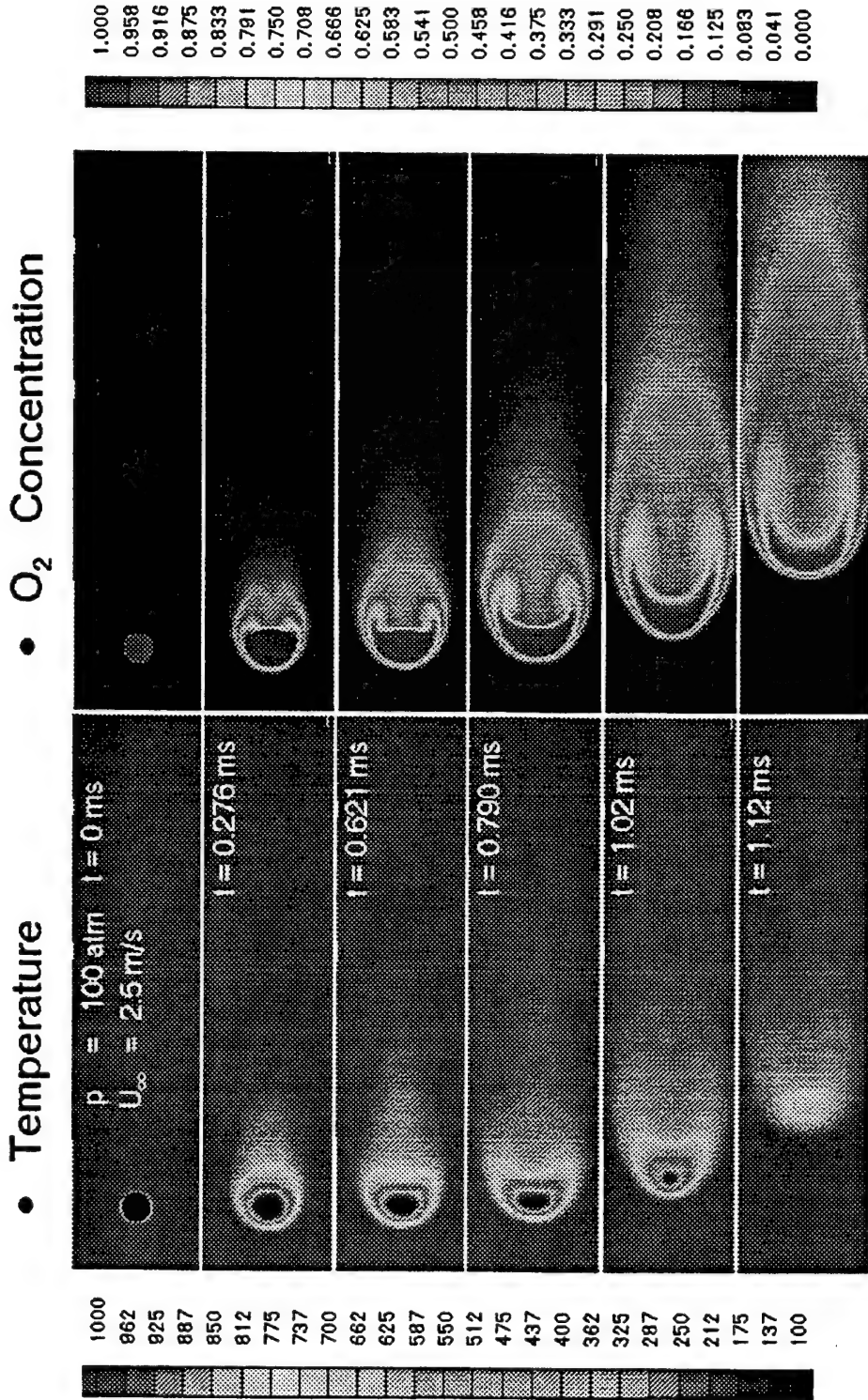


FIGURE 5. LOX Droplet Gasification in Supercritical Hydrogen Flow;  $p = 100 \text{ atm}$ ,  $U_\infty = 2.5 \text{ m/s}$ .



# LOX DROPLET GASIFICATION IN SUPERCRITICAL HYDROGEN FLOWS

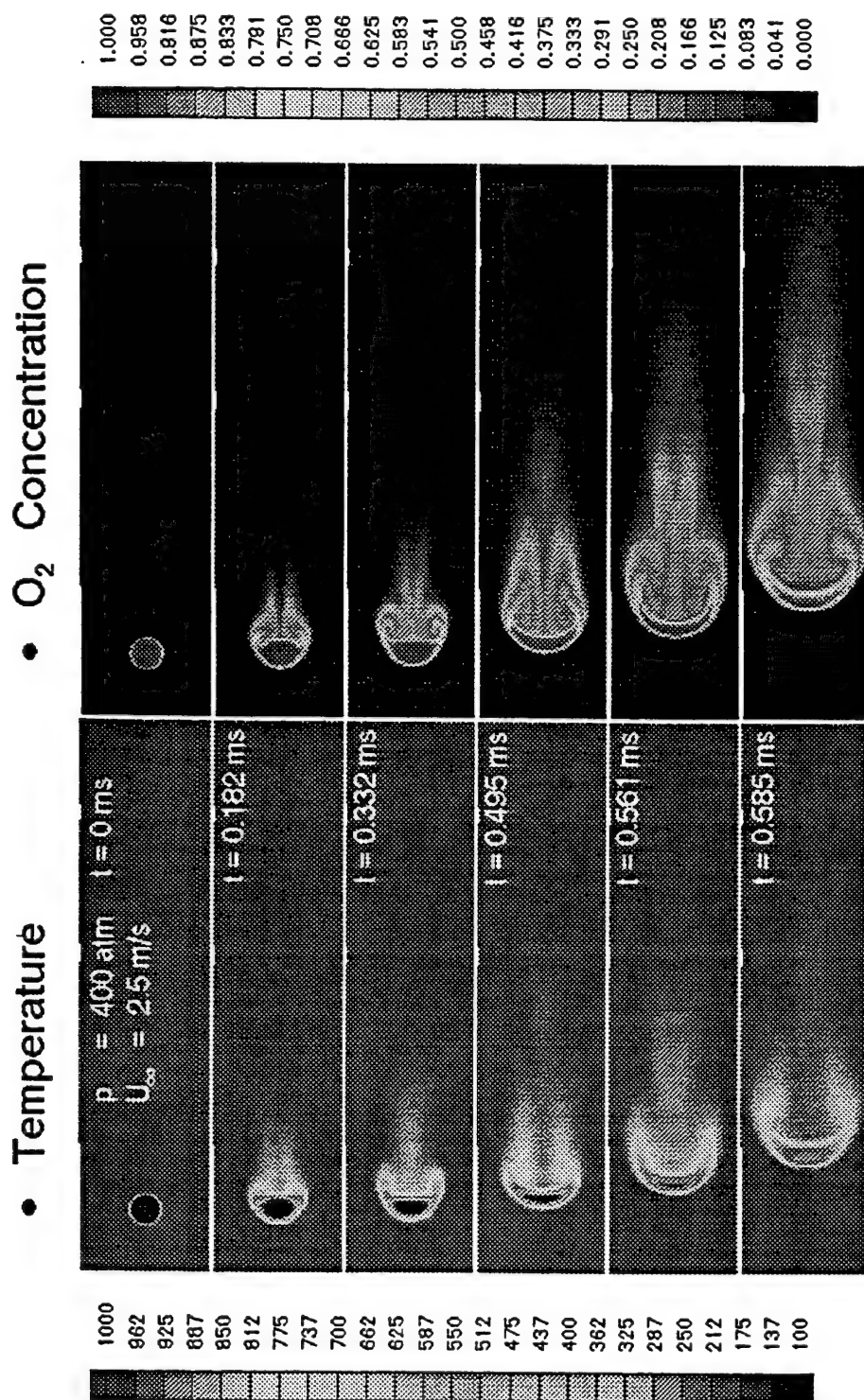


FIGURE 6. LOX Droplet Gasification in Supercritical Hydrogen Flow;  $p = 400 \text{ atm}$ ,  $U_{\infty} = 2.5 \text{ m/s}$ .

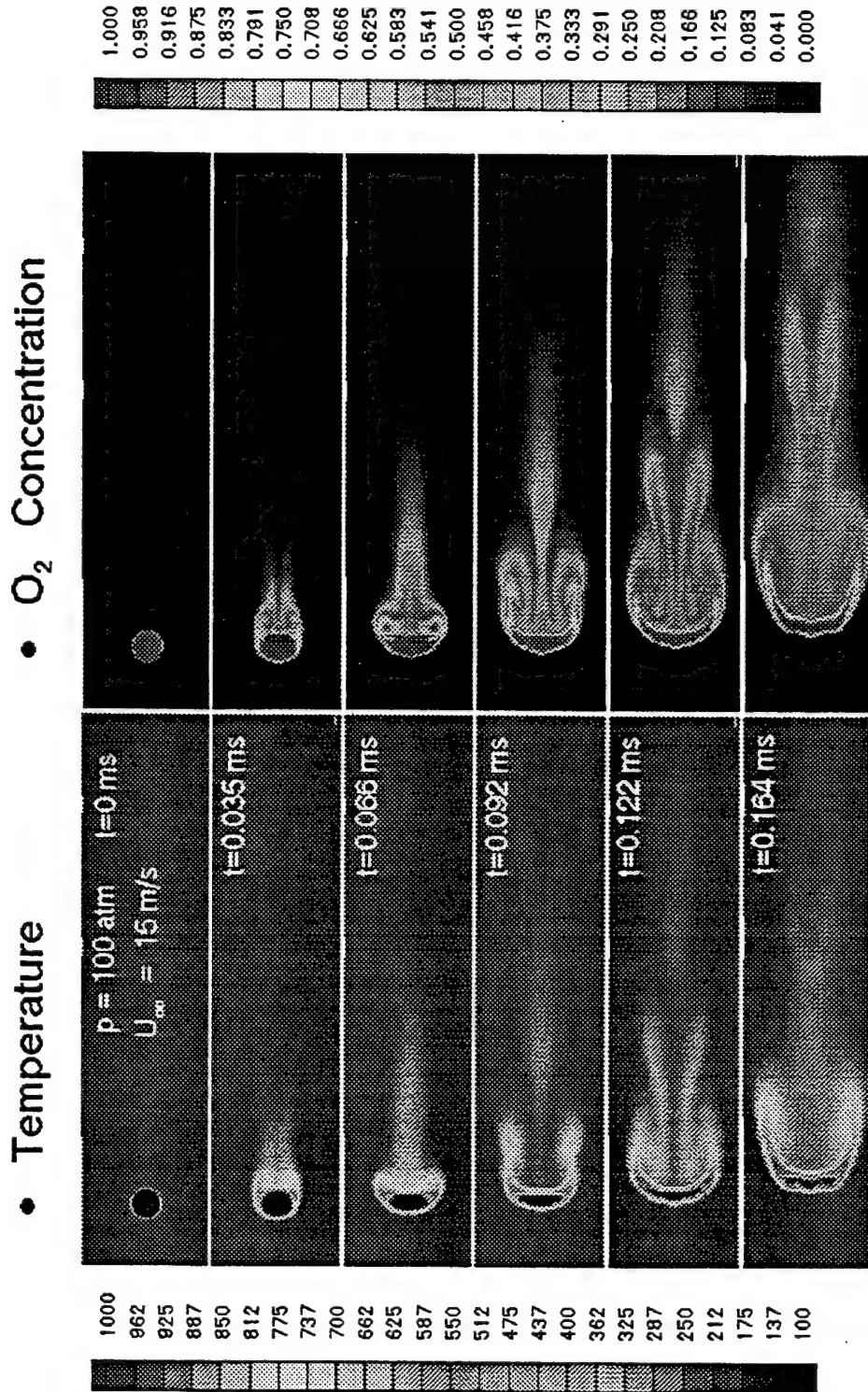


FIGURE 7. LOX Droplet Gasification in Supercritical Hydrogen Flow;  $p = 100 \text{ atm}$ ,  $U_{\infty} = 15 \text{ m/s}$ .

# LOX DROPLET GASIFICATION IN SUPERCRITICAL HYDROGEN FLOWS

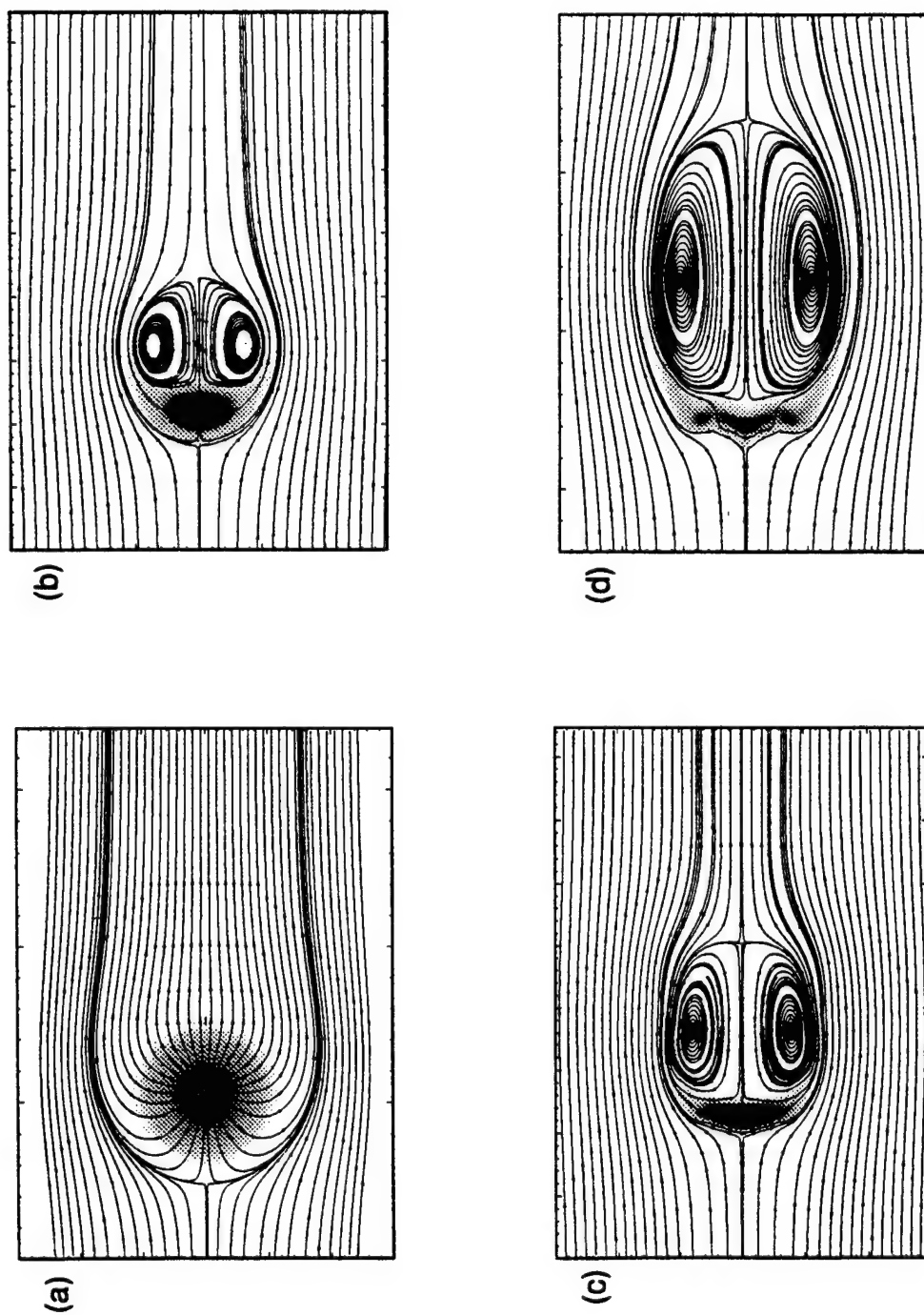
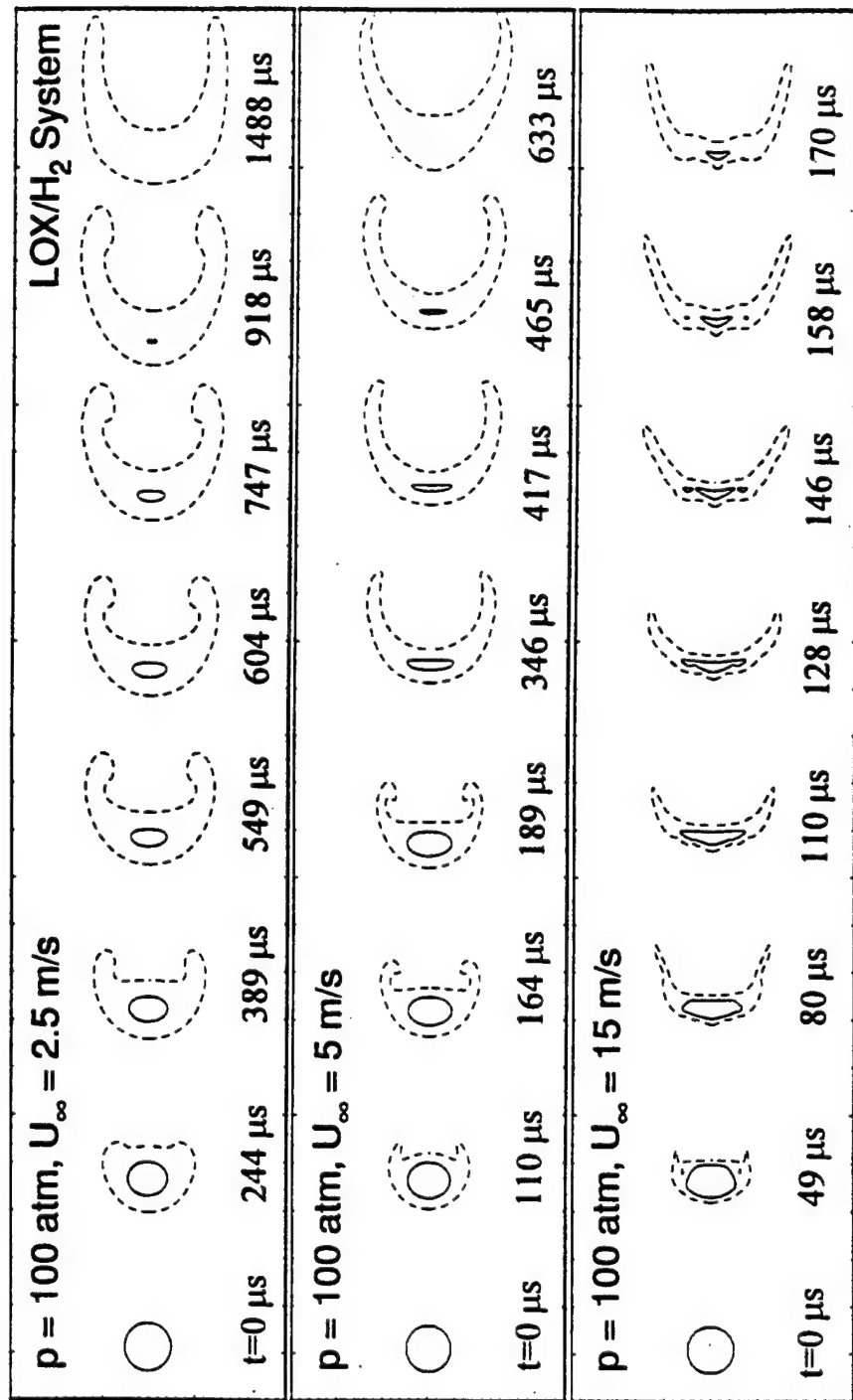


FIGURE 8. LOX Droplet Gasification in Supercritical Hydrogen Flow at  $p = 100$  atm: (a) Spherical Mode;  $U_{\infty} = 0.2$  m/s,  $t = 0.61$  ms. (b) Stripping Mode;  $U_{\infty} = 5$  m/s,  $t = 0.17$  ms. (c) Deformation Mode;  $U_{\infty} = 1.5$  m/s,  $t = 0.61$  ms. (d) Breakup Mode;  $U_{\infty} = 15$  m/s,  $t = 0.17$  ms.



— Critical Mixing Temperature      - - - - Critical Mixing Composition

FIGURE 9. Effect of Ambient Velocity on Evolution of Droplet Critical Surfaces, LOX/H<sub>2</sub> System at p = 100 atm.

LOX DROPLET GASIFICATION IN SUPERCRITICAL HYDROGEN FLOWS

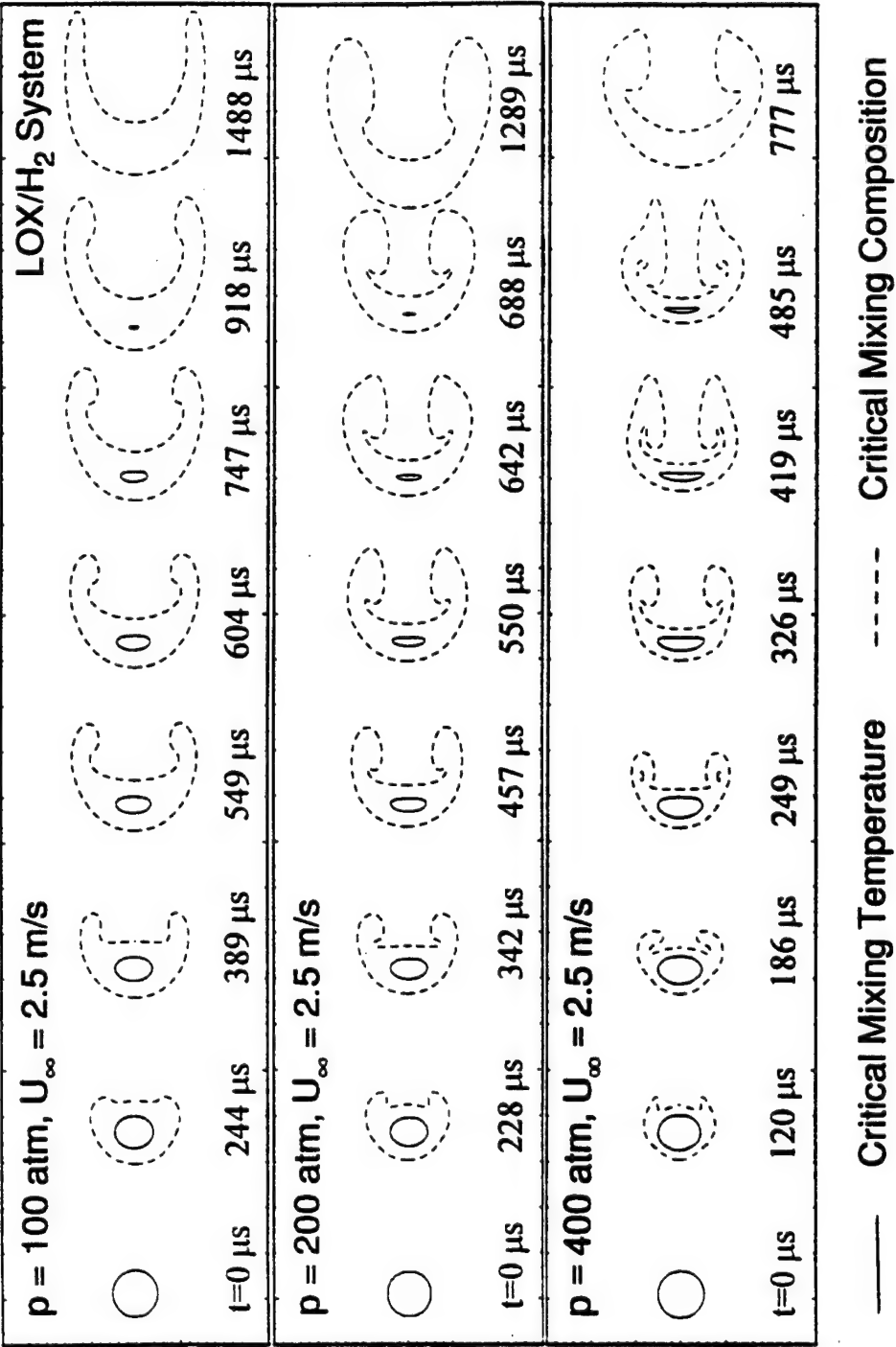


FIGURE 10. Effect of Ambient Pressure on Evolution of Droplet Critical Surfaces, LOX/H<sub>2</sub> System at  $U_\infty = 2.5$  m/s.

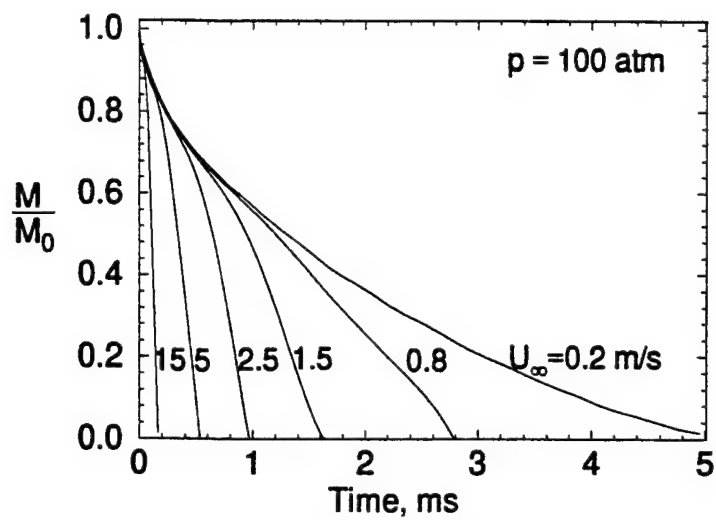


FIGURE 11. Effect of Ambient Velocity on Time Variation of Droplet Residual Mass;  $LOX/H_2$  System at  $p = 100$  atm.

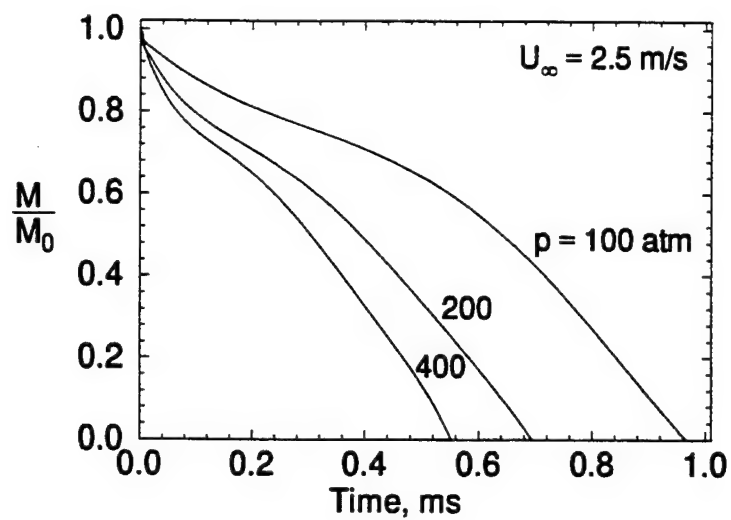


FIGURE 12. Effect of Ambient Pressure on Time Variation of Droplet Residual Mass;  
LOX/ $H_2$  System at  $U_\infty = 2.5 \text{ m/s}$ .

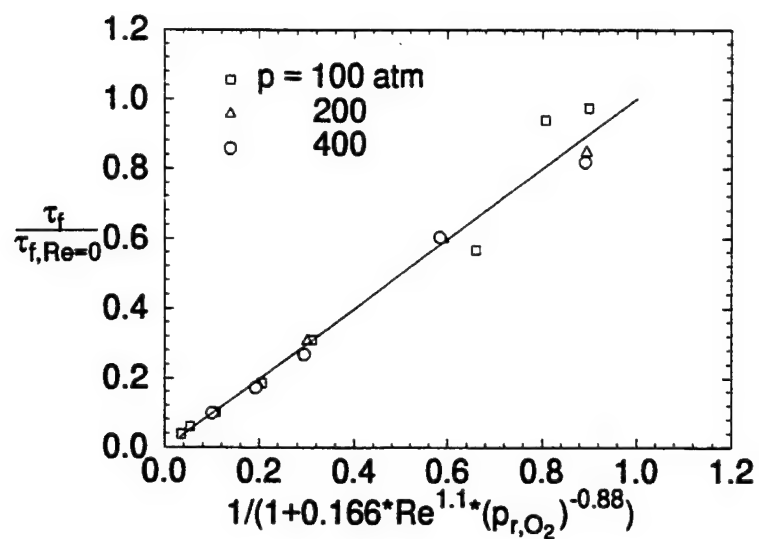


FIGURE 13. Correlation of Droplet Lifetime as a Function of Free-Stream Reynolds Number and Pressure.



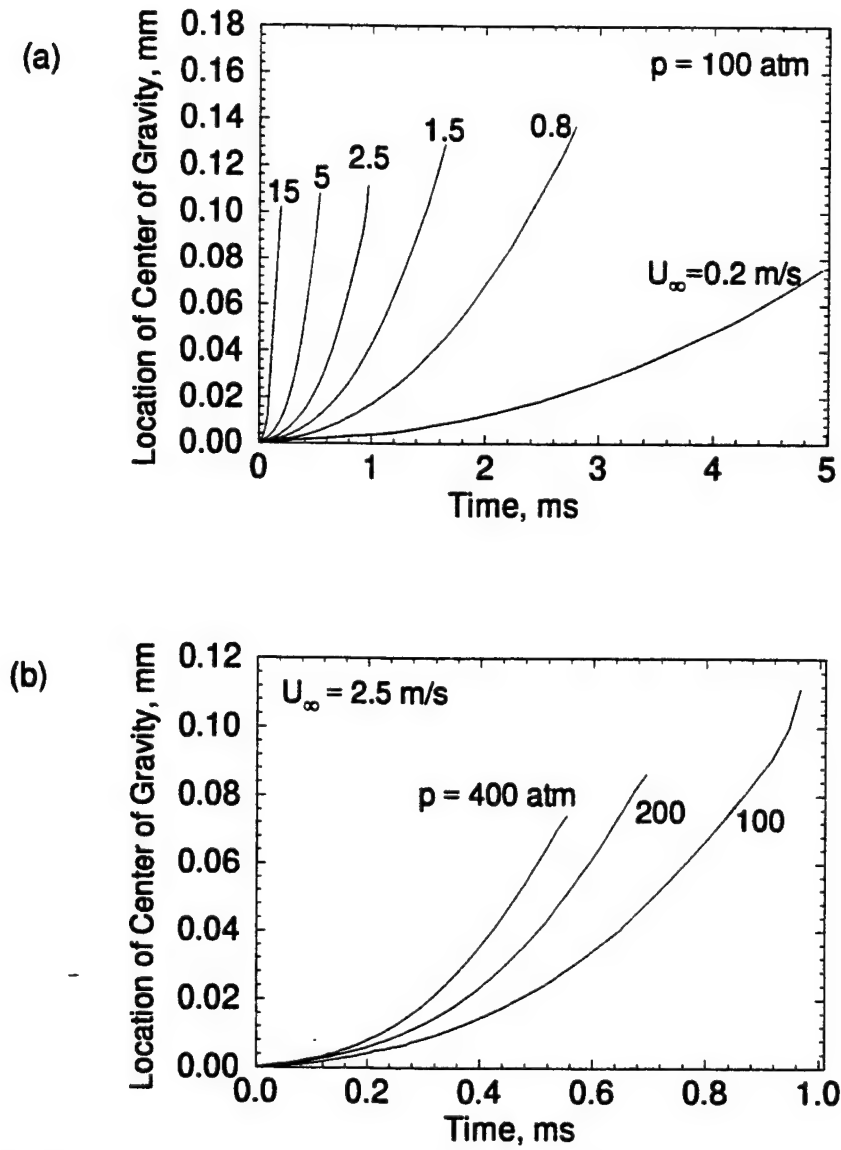


FIGURE 14. Locus of Droplet Center of Gravity,  $LOX/H_2$  System: (a) Effect of Convective Velocity at  $p = 100 \text{ atm}$ . (b) Effect of Ambient Pressure at  $U_\infty = 2.5 \text{ m/s}$ .

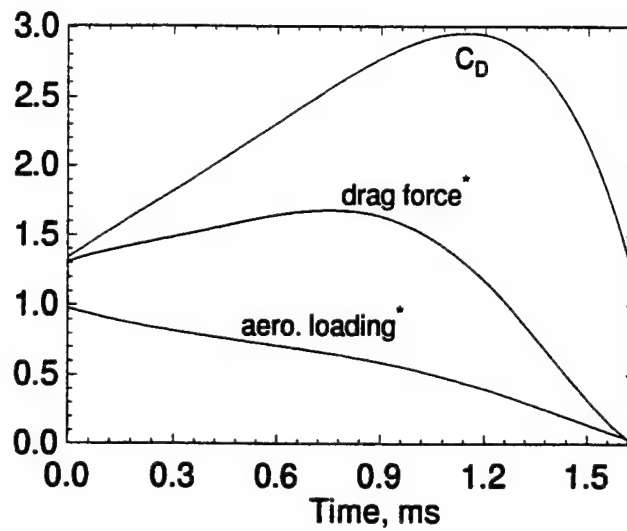


FIGURE 15. Time Variation of Total Drag Force, Aerodynamic Loading, and Drag Coefficient;  
*LOX/H<sub>2</sub>* System at  $p=100$  atm and  $U_\infty = 5$  m/s.

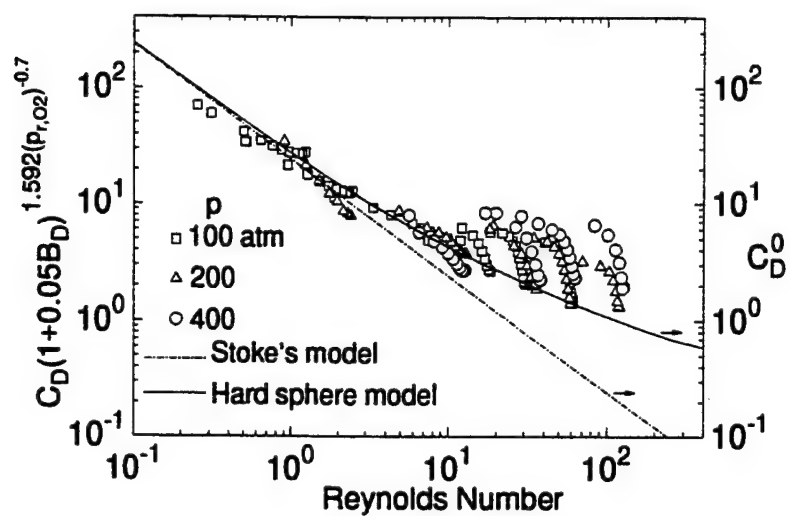


FIGURE 16. Effect of Reynolds Number and Pressure on Droplet Drag Coefficient.

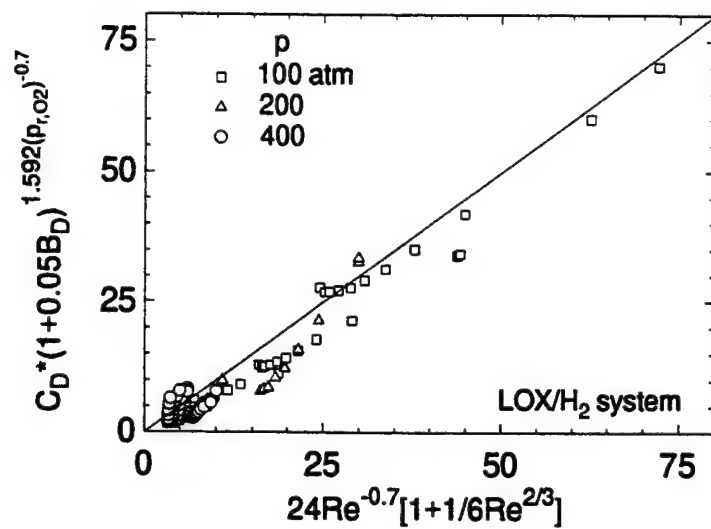


FIGURE 17. Correlation of Droplet Drag Coefficient.

# Supercritical vaporization of liquid oxygen droplets in hydrogen and water environments

By P. LAFON<sup>1</sup> V. YANG<sup>2</sup> M. HABIBALLAH<sup>3</sup>

<sup>1</sup>European Space Agency Post-Doctoral Fellow, Department of Mechanical Engineering, The Pennsylvania State University, University Park, PA, 16802, USA

<sup>2</sup> Department of Mechanical Engineering, The Pennsylvania State University, University Park, PA, 16802, USA

<sup>3</sup>Office National d'Etudes et de Recherches Aérospatiales, Châtillon, France

(Received )

This paper presents a comprehensive theoretical analysis conducted to study liquid oxygen (LOX) droplet vaporization for a broad range of ambient conditions in either hydrogen or water/hydrogen quiescent environments. An important effort has been devoted to the estimation of transport and thermodynamic properties. In addition, influence of cross-diffusion effects (Dufour and Soret effects) is studied, showing that these effects may be neglected in droplet vaporization studies at high pressures. Condensation of gaseous water in the low-temperature zone close to oxygen droplet surface is taken into account by means of a detailed sub-model. Predictions show that condensation occurs in the neighborhood of the oxygen droplet. However, the condensed particles do not reach droplet surface but are blown away by the convection flow induced by the vaporization process. Thus, water condensation has only a small influence on the vaporization process. A correlation of the droplet lifetime valid for the oxygen/hydrogen/water system and for ambient conditions such that supercritical vaporization regime occurs in the early stages of the droplet lifetime is presented.

---

## NOMENCLATURE

<i>a</i>	Equation of state constant in Eq.(2.8)
<i>A</i>	Surface area
<i>b</i>	Equation of state constant in Eq.(2.8)
<i>B</i>	Spalding number

$C_p$	Constant-pressure specific heat
$D$	Droplet diameter
$D_{ij}$	Binary mass diffusion coefficient
$D_{im}$	Effective mass diffusion coefficient
$D_{Ti}$	Thermal diffusion coefficient of species $i$
$e$	Specific total internal energy
$F_T$	Thermophoretic force
$F_v$	Viscous force
$G$	Gibbs free energy per mole
$g$	Gibbs free energy per unit mass
$\bar{h}_i$	Specific enthalpy of species $i$
$J$	Homogeneous nucleation rate
$K_{vap}$	Vaporization kinetic coefficient in Eq.(3.3)
$\dot{m}$	Droplet mass evaporation rate
$N$	Number of species
$p$	Pressure
$q_e$	Energy diffusion flux
$q_i$	Mass diffusion flux of species $i$
$r$	Radial coordinate
$R$	Droplet radius
$R_u$	Universal gas constant
$S$	Saturation ratio
$s$	Specific total entropy
$v$	Velocity
$v_s$	Control surface moving velocity
$V$	Total volume
$V_i$	Diffusion velocity of species $i$
$X_i$	Mole fraction of species $i$
$Y_i$	Mass fraction of species $i$
$W$	Molecular weight

$Z$  Compressibility factor

*Greek Symbols*

$\alpha$  Thermal diffusivity

$\alpha(T)$  Soave temperature function in Eq.(2.8)

$\lambda$  Thermal conductivity

$\lambda$  Molecular mean free path

$\mu$  Viscosity

$\mu_i$  Chemical potential of species  $i$

$\rho$  Density

$\sigma$  Surface tension

$\tau$  Droplet lifetime

$\omega$  Acentric factor

*Subscripts*

$c$  Critical condition

$i$  Species  $i$

$p$  Condensed particle

$r$  Reduced thermodynamic property

$rf$  Reference fluid

$sat$  Saturation value

$\infty$  Ambient condition

*Superscripts*

$g$  Gaseous phase

$l$  Liquid phase

$0$  Dilute gas limit

$()$  Time derivative

$*$  Dimensionless quantity

## 1. Introduction

Droplet vaporization is a physical process occurring in many liquid-fueled combustion devices. Atomization of liquid fuel leads to the formation of a spray of droplets that then undergoes a sequence of vaporization, ignition, and combustion processes. In the past few decades, combustor performance has been substantially enhanced by increasing the operating temperature and pressure in the thermodynamic supercritical state of the fuel species. The conventional models developed for low-pressure applications could no longer be applied. Recently, several theoretical works have been devoted to the understanding of droplet vaporization and combustion under high pressure conditions. Both hydrocarbon droplets in air, see for example Hsieh *et al.* (1991), Shuen *et al.* (1992), Curtis & Farrel (1992), and Jia & Gogos (1993), and liquid oxygen droplets in hydrogen environments, see for example Litchford & Jeng (1990), Delplanque & Sirignano (1991), Lin *et al.* (1994), and Daou *et al.* (1995), are treated comprehensively, with emphasis placed on the effects of transient diffusion, interfacial thermodynamics with dissolution of gaseous components in the liquid phase. The work of Lin *et al.* (1994) appears to be the most comprehensive to date because of the attention devoted to transport properties modelization.

The present work is concerned with the vaporization of liquid oxygen in either pure hydrogen or mixed hydrogen/water environments due to its broad applications in cryogenic rocket engines using hydrogen and oxygen as propellants, such as the VULCAIN engine (Ariane 5 main stage engine), space shuttle main engine (SSME), J-2 engine (Saturn V 3<sup>rd</sup>-stage engine, and R?-10 engine (?). In these engines, the chamber pressure and temperature overpass the critical values of oxygen and hydrogen.

In the present study, we present an unified treatment of transport properties, thermal conductivity and molecular diffusion coefficient valid for a wide range of thermodynamic states. This treatment has been formulated in such a generalized manner that the results can be practically applied to any types of liquid-fueled propellant couples. The Soret and Dufour's effects have been estimated carefully, since they are expected to be significant for the our problem, because of the important disparity in molecular weight between oxygen and hydrogen, and because of the large temperature gradients involved. In ad-



dition, in the presented analysis, all the thermodynamic properties are derived from the chosen equation of state in a very self-consistent manner. This self-consistent treatment of thermodynamic properties renders the numerical scheme very efficient. For subcritical regimes of vaporization, it allows the use of a kinetic-like expression for evaluation of subcritical vaporization rate, which avoids any iterative matching procedure. All the previous features constitute prolongations and improvements of the work of Lin *et al.* (1994).

Condensation of gaseous water diffusing to the oxygen droplet surface is a subject of interest for many years, see for example Litchford & Jeng (1990) and Powell (1988). This phenomenon, due to the concomitant effects of the low temperature of the oxygen droplet surface and of the diffusion of the gaseous water towards this surface, is expected to affect the surface conditions and thus the vaporization process. All the numerical analyses mentioned previously have eluded this, and we can only make reference to the simplified analyses of Yoset (1992), Lafon & Prud'homme (1994), and Lin *et al.* (1994). In this study, a comprehensive analysis of the water condensation process is carried out by estimating all the different mechanisms involved in this process.

Finally, we have kept in mind that the objective of any single-droplet vaporization study is to provide sub-models used in spray computations, therefore we have conducted a large series of computations corresponding to a variety of initial and ambient conditions. A correlation of the droplet lifetime has been deduced, it is valid for the oxygen/hydrogen/water system when the supercritical vaporization regime occurs in the early stage of the droplet lifetime.

In this paper, we first describe the theoretical formulation with emphasis on transport and thermodynamic properties, the numerical methods used are thereafter briefly presented. The model is first applied to the vaporization of oxygen droplets in pure hydrogen environments and, after presenting the water condensation sub-model, it is then applied to the vaporization of oxygen droplets in mixed hydrogen/water environments.

## 2. Theoretical Formulation

We consider the situation where a droplet initially with a uniform distribution of subcritical temperature is suddenly injected in a supercritical, quiescent environment. The

problem is entirely governed by a complete set of conservation equations. Because buoyancy effects and forced convection are not considered, the problem is one-dimensional.

### 2.1. Conservation Equations

Balance equations are valid for both phases. Let us consider an arbitrary control volume  $V_a(t)$  delimited by a surface  $A_a(t)$  moving in an absolute referential at speed  $\mathbf{v}_s$ . The mass balance equation may be written as follows

$$\frac{d}{dt} \int_{V_a(t)} \rho dV + \int_{A_a(t)} \rho(\mathbf{v} - \mathbf{v}_s) \cdot d\mathbf{A} = 0 \quad (2.1)$$

The momentum and energy conservation equations are simplified with the following hypotheses. The velocities involved are very small, so that total energy is almost equal to internal energy and viscous dissipation can be neglected. The momentum equation is then reduced to a space-constant pressure equation

$$\nabla p = 0 \quad (2.2)$$

From the first law of the thermodynamics applied to the control volume, we derive the conservation of energy

$$\frac{d}{dt} \int_{V_a(t)} \rho e dV + \int_{A_a(t)} \rho e(\mathbf{v} - \mathbf{v}_s) \cdot d\mathbf{A} = - \int_{A_a(t)} p \mathbf{v} \cdot d\mathbf{A} - \int_{A_a(t)} q_e \cdot d\mathbf{A} \quad (2.3)$$

Species conservation does not involve any simplifying hypotheses

$$\frac{d}{dt} \int_{V_a(t)} \rho Y_i dV + \int_{A_a(t)} \rho Y_i(\mathbf{v} - \mathbf{v}_s) \cdot d\mathbf{A} = - \int_{A_a(t)} \mathbf{q}_i \cdot d\mathbf{A} \quad (2.4)$$

### 2.2. Diffusion Fluxes

The energy and mass diffusion fluxes,  $q_e$  and  $q_i$ , in Eqs.(2.3) and (2.4) need to be modeled. To set the analysis in its most general form, the Soret (thermal-diffusion) effect which accounts for heat diffusion due to concentration gradients is considered along with its reciprocal Dufour phenomenon. The Soret effect is evidenced by the observation that light molecules tend to diffuse towards high-temperature regions and vice versa. This phenomenon may be significant in the present study because of the disparity of molecular weight between hydrogen and oxygen and the steep temperature gradient involved. The

overall diffusion fluxes take the form

$$q_e = -\lambda \nabla T - \sum_i^N q_i \bar{h}_i + R_u T \sum_i^N \sum_j^N \frac{X_j D_{Ti}}{W_i D_{ij}} (V_i - V_j) \quad (2.5)$$

$$q_i = \rho Y_i V_i = -\rho D_{im} \nabla Y_i - D_{Ti} \frac{\nabla T}{T} \quad (2.6)$$

where Fourier's and Fick's laws are used to approximate the ordinary energy and mass diffusion, respectively. As it was mentioned in Bird, Steward & Lightfoot (1960), for systems involving more than 2 species, Fick's law is only an approximation of the molecular diffusion velocity system which necessitates the use of a mass averaged diffusion coefficient

$$D_{im} = (1 - X_i) / \sum_{i \neq j}^N (X_j / D_{ij}) \quad (2.7)$$

### 2.3. Property Evaluation

Transport and thermodynamic properties play a decisive role in droplet vaporization process. The former rule mass and energy transfer, whereas the latter affect the equilibrium conditions and energy needed for phase change. Both properties dictate the conditions of occurrence of supercritical regimes. Thus, if accurate predictions of the droplet lifetime are wanted, precise modelization of thermodynamic behavior and transport properties is needed. In addition, since the two initial phases may collapse to a single phase, the property evaluation must be unified over the entire range of temperatures, pressures and compositions.

#### 2.3.1. Thermodynamic Properties

All the thermodynamic properties are derived from the Soave-Redlich-Kwong equation of state, see Graboski & Daubert (1979). It represents a good compromise between computation complexity and physical accuracy, as was mentioned by Lin *et al.* (1994). Pressure may be expressed in terms of density and temperature

$$p = \frac{\rho R_u T}{(W - b\rho)} + \frac{a\alpha}{W} \frac{\rho^2}{(W + b\rho)} \quad (2.8)$$

where  $a$  and  $b$  accounts for attractive forces and repulsive forces between molecules, respectively. Mixing rules to compute  $a$  and  $b$  are based on corresponding state principle

$$a\alpha = \sum_i^N \sum_j^N X_i X_j (1 - k_{ij}) \sqrt{a_i a_j \alpha_i \alpha_j}, \quad b = \sum_i^N X_i b_i \quad (2.9)$$

where  $a_i$ ,  $b_i$  and  $\alpha_i(T)$  are related to the critical properties and acentric factor of constituent species as follows

$$a_i = \frac{0.42748 R_u^2 T_{ci}^2}{P_{ci}}, \quad b_i = \frac{0.08664 R_u T_{ci}}{P_{ci}}, \quad (2.10)$$

$$\alpha_i(T) = \left[ 1 + f\omega_i \left( 1 - \sqrt{T/T_{ci}} \right) \right]^2 \quad \text{with} \quad f\omega_i = 0.48 + 1.574\omega_i - 0.176\omega_i^2$$

All the thermodynamic properties required in the analysis come from derivation of Eq.(2.8) and (2.9). For instance, the internal energy is derived from the following relation

$$e(\rho, T, Y_i) = e^0(T, Y_i) + \int_0^\rho \left[ \frac{p}{\rho^2} - \frac{T}{\rho^2} \left( \frac{\partial p}{\partial T} \right)_\rho \right] d\rho \quad (2.11)$$

The previous integral may be computed to give the following analytic formula

$$e(\rho, T, Y_i) = e^0(T, Y_i) + T^2 \left[ \frac{\partial(a\alpha/T)}{\partial T} \right]_{Y_i} \frac{\rho}{bW} \text{Log}(1 + b\rho/W) \quad (2.12)$$

This expression of internal energy may be written as an explicit function of temperature and constituent partial density. Then, some thermodynamic considerations, described in Lafon (1994), enable us to compute easily specific enthalpy of each species using direct derivation the Eq.(2.12)

$$\bar{h}_i = \left( \frac{\partial m h}{\partial m_i} \right)_{p, T, m_{j \neq i}} = \left( \frac{\partial \rho e}{\partial \rho_i} \right)_{T, \rho_{j \neq i}} + \frac{T}{\rho} \left( \frac{\partial p}{\partial T} \right)_\rho / \left( \frac{\partial p}{\partial \rho} \right)_T \quad (2.13)$$

To compute expression of chemical potential, first expression of entropy is required.

By integration of the relation

$$s(\rho, T, Y_i) = s^0(\rho, T, Y_i) + \frac{R_u}{W} \text{Log} Z + \int_0^\rho \left[ \frac{R_u/W}{\rho} - \frac{1}{\rho^2} \left( \frac{\partial p}{\partial T} \right)_\rho \right] d\rho, \quad (2.14)$$

an analytical expression of entropy is obtained

$$\begin{aligned} s(\rho, T, Y_i) = & \int_{T^0}^T \frac{C_p^0}{T} dT - \frac{R}{W} \text{Log} \left( \frac{\rho R_u T}{P^0} \right) - \frac{R}{W} \sum_{i=1}^N X_i \text{Log} X_i \\ & + \frac{R}{W} \text{Log}(1 - b\rho/W) + \frac{1}{bW} \left[ \frac{\partial(a\alpha)}{\partial T} \right]_{Y_i} \text{Log}(1 + b\rho/W) \end{aligned} \quad (2.15)$$

Chemical potential is then easily evaluated by means of

$$\mu_i = \left( \frac{\partial mg}{\partial m_i} \right)_{p,T,m_{j \neq i}} = \left( \frac{\partial \rho e}{\partial \rho_i} \right)_{T,\rho_{j \neq i}} - T \left( \frac{\partial \rho s}{\partial \rho_i} \right)_{T,\rho_{j \neq i}} \quad (2.16)$$

### 2.3.2. Transport Properties

Transport properties determine the mass and energy transport which dictate the interface conditions and consequently the vaporization rate and the occurrence of critical conditions. The major properties of interest are thermal conductivity, mass diffusivity and thermal-diffusion coefficient. Classical gas kinetic theory fails to correctly predict transport properties at high pressures. However, it is always possible to estimate in the dilute-gas limit and then take into account the dense-fluid effects. Thermal conductivity is generally divided into two contributions,

$$\lambda_m(\rho, T, Y_i) = \lambda'_m(T, Y_i) + \lambda''_m(\rho, T, Y_i) \quad (2.17)$$

$\lambda'_m(T, Y_i)$  and  $\lambda''_m(\rho, T, Y_i)$  represent the internal contribution and the translational and collisional contribution to the thermal conductivity, respectively. For a mixture the first term may be evaluated by means of an empirical mixing rule

$$\lambda'_m = \frac{1}{2} \sum_i^N \sum_j^N X_i X_j \left( \frac{1}{\lambda'_i} + \frac{1}{\lambda'_j} \right)^{-1}, \quad (2.18)$$

in conjunction with the Eucken's correlation modified for polyatomic gases

$$\lambda'_i = 1.32 \mu_i^0 \left( c_{p,i}^0 - \frac{5}{2} \frac{R_u}{W_i} \right) \quad (2.19)$$

where the low pressure estimations of viscosity and specific heat are obtained from polynomial adjustments of existing experimental data, see for example Reid, Prausnitz & Poling (1987).

The collisional and translational contribution  $\lambda''_m(\rho, T, Y_i)$  may be evaluated using the corresponding-state method proposed by Ely & Hanley (1981) and (1983). The method is able to predict transport properties over a large domain of temperatures and pressures, from compressed liquid to dilute gas. The scheme assumes that the configurational properties of a single-phase mixture can be equated to those of a hypothetical pure fluid, which are then evaluated via corresponding states with respect to a given reference fluid. It requires the characteristic values of each species: critical coordinates and acentric factor.

Details of the procedure may be found in Ely & Hanley (1983) or Hsiao *et al.* (1995), but let us briefly present the guidelines of the method used to compute thermal conductivity.

$$\lambda_m''(\rho, T, Y_i) = \lambda_{rf}''(\rho_{rf}, T_{rf}) \mathcal{F}_\lambda \mathcal{X}_\lambda \quad (2.20)$$

$\mathcal{F}_\lambda$  and  $\mathcal{X}_\lambda$  are the scaling factor and a correction factor respectively. The latter compensates the non-correspondent behavior of the mixture. For the reference fluid, the collisional and translational contribution of thermal conductivity is divided into three parts

$$\lambda_{rf}''(\rho_{rf}, T_{rf}) = \lambda_{rf}^0(T_{rf}) + \Delta\lambda_{exc}(\rho_{rf}, T_{rf}) + \Delta\lambda_{crit}(\rho_{rf}, T_{rf}) \quad (2.21)$$

$\lambda_{rf}^0(T_{rf})$  is the value at the dilute gas limit which may be evaluated by

$$\lambda_{rf}^0(T_{rf}) = \frac{15R_u}{4W_{rf}} \mu_{rf}^0$$

$\Delta\lambda_{exc}(\rho_{rf}, T_{rf})$  and  $\Delta\lambda_{crit}(\rho_{rf}, T_{rf})$  correspond to the dense fluid correction and to the critical enhancement, respectively. They may be computed from analytical expressions fitted to experimental data. The critical enhancement part is not included in the present analysis for two reasons: first, properties which diverge strongly for pure components diverge only weakly for mixtures as discussed by Bruno & Ely (1991), second, the critical enhancement of the thermal conductivity has not been observed experimentally for mixtures.

Let us now present the estimations techniques used for the molecular diffusion coefficient. For gaseous phase, the approach proceeds in two steps. A low pressure binary mass diffusivity is obtained using the Chapman-Enskog theory in conjunction with the Lennard-Jones intermolecular potential-energy function, see for example Reid, Prausnitz & Poling (1987). The coefficient is corrected with the correlation of due to the work of Takahashi (1974) to take into account high pressure effects. However this method fails to predict liquid molecular diffusion coefficient which is best estimated with Wilke-and-Chang procedure. As supercritical regime is reached liquid estimation technique is still applied for temperatures below the mixture critical temperature. These methods are matched at the interface by using a correcting factor for the liquid estimation.

Concerning the thermal diffusion coefficients, much less material is available in the

literature, especially about the pressure effects on these coefficients. Pressure effects are expected to be of the same order of magnitude as on binary molecular diffusion coefficients. However, to estimate these coefficients, we use the theoretical developments of Dixon-Lewis (1968). This work is based on extension of the Chapman-Enskog kinetic to polyatomic gases. Since this method is valid only in the low pressure region, overestimations of the thermal diffusion coefficients are expected.

#### 2.4. Interfacial Boundary Conditions

Before the surface temperature reaches the mixture critical value, thermodynamic phase equilibrium, characterized by a minimum of the Gibbs function, is assumed to prevail at the interface. If surface tension is neglected, the equilibrium relations may be written as

$$\begin{cases} T^g &= T^l \\ p^g &= p^l \\ \mu_i^g &= \mu_i^l \end{cases} \quad (2.22)$$

The conservation of mass, species and energy across the interface are

$$\dot{m} = \rho(\mathbf{v} - \dot{\mathbf{R}})A|_{r=R_+} = \rho(\mathbf{v} - \dot{\mathbf{R}})A|_{r=R_-} \quad (2.23)$$

$$\dot{m}_i = [\dot{m}Y_i + \mathbf{q}_i A]_{r=R_+} = [\dot{m}Y_i + \mathbf{q}_i A]_{r=R_-} \quad (2.24)$$

$$-\lambda \nabla T|_{r=R_-} = -\lambda \nabla T|_{r=R_+} + \sum_i^N \dot{m}_i(\bar{h}_i^g - \bar{h}_i^l) \quad (2.25)$$

where  $R_-$  and  $R_+$  denotes the conditions at the interface on the liquid side and gaseous side, respectively.

### 3. Numerical Methods

The set of equations, Eqs. (2.1)-(2.4), is solved using a fully implicit scheme. Balance equations are discretized on a time varying grid with a finite volume formulation. Two different scenarios occur depending upon whether the vaporization regime is subcritical or supercritical. However, in both cases the grid follows the time regression of droplet interface. For supercritical regimes the droplet interface is either defined by critical isotherm or critical composition line. To perform a fully implicit treatment of the problem using time-varying grid cell, the volume of each grid cell is included in the quantities computed at each time step by inversion of the linear system introduced by

the implicit formulation. The variation of a grid cell is determined by the difference of its limiting surface velocities. If the location of each grid node is only a function of the instantaneous droplet radius, then the volume variation of each grid cell may be easily linked to the volume variations of the adjacent cells, same thing for the surface velocities. Droplet surface velocity is given by Eq. (2.23) for subcritical vaporization regimes, or by assuming that the interface corresponds to the mixture critical temperature line or critical composition line for supercritical vaporization regimes. Details of the numerical methods are presented in Lafon (1994). The following vector summarize the quantities computed at each time step for each grid cell

$$Q = (\rho V, \rho v A, \rho e V, \rho_i V, V)^T \quad (3.1)$$

All the quantities required in the resolution are expressed with those contained in the previous vector using a linearization technique. This technique gives for the expression of temperature

$$T^{n+1} = T^n + \nabla_Q T (Q^{n+1} - Q^n) \quad (3.2)$$

where the expression of the vector  $\nabla_Q T$  is derived from thermodynamic considerations involving Eq.(2.8) and its derivatives, see Lafon (1994) for details. Time step is reduced when temperature variations exceed a certain value, so that linearization techniques is still applicable.

The treatment of interfacial conditions requires a special procedure. Liquid and gaseous conditions at the interface are supposed to be those of the two cells adjacent to the surface. Interface thermal conductivity is artificially increased. This procedure does not alter the local energy flux value and thus reduced the local temperature gradient so that temperature difference between liquid and gaseous phase vanishes to zero. Then the transfer of each species involved in the thermodynamic equilibrium between the two phases is realized by using the following pseudo-phenomenological or kinetic-like relationship

$$\dot{m}_i = K_{vap,i} (\mu_i^l - \mu_i^g) \quad (3.3)$$

This expression is comparable to phenomenological laws such as Fourier's law for heat conduction or Fick's law for mass diffusion. The flux is proportional to the difference



of potential via the diffusion coefficient. To ensure the thermodynamic equilibrium, the value of the vaporization kinetic coefficient is set so that the difference between chemical potential is as small as wanted. This technique requires an implicit expression which is obtained by means of a relation similar to Eq.(3.2) for chemical potential. This method does not necessitate any sub-iterative process, but it requires an expression of chemical potential derivatives as accurate and as consistent as possible. If not, computations will diverge. That why all thermodynamic properties are only derived from derivations of Eqs.(2.8) and (2.9). Once the thermodynamic equilibrium is initiated, the interface evolves on a thermodynamic equilibrium trajectory. This evolution is controlled by heat and mass fluxes at the interface. As soon as the interface reaches the mixture critical conditions, this procedure is no longer applied, and the analysis switches to a single-phase approach.

#### 4. Vaporization in Hydrogen

The model is first applied to the vaporization of liquid oxygen droplet in hydrogen environments with a broad range of initial and ambient conditions.

##### 4.1. Binary Equilibrium and Criticality

Let us consider the binary equilibrium involved in this particular case at the droplet interface. The variance of the thermodynamic equilibrium is

$$v = N + 2 - \phi \quad (4.1)$$

Only two species (oxygen and hydrogen) and two phases (liquid and gas) are present, so that the variance is 2. Furthermore, the momentum balance over the domain, and especially at the interface, prescribes a constant pressure. As a consequence the reduced variance is unity. Evolutions of composition and temperature at the interface are linked by the thermodynamic equilibrium. Trajectories of the equilibrium are reported in Fig. 1.

For subcritical pressures hydrogen dissolution in the liquid phase is small and almost negligible. As the pressure increases above the critical pressure of pure oxygen (49.7 atm), the dissolution effect becomes more and more significant. For a fixed pressure, dissolution is maximum when the two phases reach their critical conditions, and increases generally

with pressure. Thus, for pressure equal to 300 atm, critical hydrogen molar composition is close to 0.5. However, since there is a big disparity in molecular weight between both species, hydrogen critical mass compositions are still close to zero. Nevertheless, hydrogen properties are different enough from the oxygen ones to affect substantially the mixture properties. As an example, enthalpy of vaporization is reported for various pressures in Fig. 2. Dissolution makes enthalpy of vaporization a function of both temperature and pressure.

Let us discuss now about an important feature, which concerns the properties of the mixture critical point. For a pure component the critical point is the locus of a loss of mechanical stability; the first and second derivatives of pressure with respect to density vanish to zero. This implies a strong divergence of the specific heat as the critical point is approached. For a mixture, the criticality criteria is somehow different. As its critical conditions are approached, the mixture lose its material stability, a phenomenon which may be characterized for a binary mixture by the relation as mentioned by Bruno & Ely (1991)

$$\left( \frac{\partial^2 G}{\partial X^2} \right)_{P,T} = 0 \quad (4.2)$$

All cubic equations of state use mixture rules based on the corresponding state principle. The mixture properties are reported to the properties of a hypothetical pure component by means of the mixture rules. Thus, for the mixture, a pseudo-critical point exists; it has all the characteristics of a pure component critical point, and is therefore a locus of a strong divergence of the specific heat. However, let us consider a binary mixture which pressure is above the critical pressure of the less volatile species (oxygen), but, which temperature is below the mixture critical value. When temperature progressively increases, it will reach its mixture critical point before the pseudo-critical point. Since this point is different from the pseudo-critical point but yet not too far from it, only a weak divergence on the specific heat is observed. This divergence vanishes when the pressure is far above the critical pressure.

When interface reaches its critical conditions, no distinction between the two phases remains. The critical interface is then classically defined as the critical isotherm, and it is still the locus of important density gradients. Another definition based on critical

composition may be considered. This choice can be justified by the fact that it may better represent the mixing process involved in supercritical vaporization. Application of one or the other definition will lead to different results mainly because the Lewis number is not unity (See next sections). The former definition seems the most adequate for comparison with experimental data, in which droplet regression is tracked by means of measurement techniques sensitive to temperature or density gradients -shadowgraphy is used by Hsiang & Feath (1993)-. For use in spray analysis, in which vaporization process is treated as a source term of mass and a sink term of energy in balance equations, the definition of the critical interface based on temperature seems also adequate. The mixing process experienced by the vaporized species is then handle by the gas-mixing model of the spray model. However, in the following study, both definition based on temperature and definition based on composition are considered.

#### 4.2. Discussion of Results

A series of calculations have been carried out to study the effects of ambient pressure and temperature on droplet behavior in both the subcritical and supercritical vaporization regimes. In this pure vaporization case, the problem is entirely controlled by diffusion, as was reported by Daou *et al.* (1995), dimensional analysis shows that the initial droplet diameter is the only length scale and that the droplet lifetime is proportional to the squared initial droplet diameter. Thus only droplets with an initial diameter  $D_0 = 100 \mu m$  are considered in the present analysis.

The case with an ambient hydrogen temperature of 1000 K is first considered to provide a baseline data set. Figure 3 shows the time variations of droplet surface temperature at various pressures. Three different scenarios must be reported. First, for low pressures ( $p = 10 atm$ ), the surface temperature rises suddenly and reaches a constant value, a condition referred by Hsieh *et al.* (1991) as the pseudo wet-bulb state. The constant value is slightly lower than the oxygen boiling temperature because of the presence of hydrogen on the gaseous side of the interface. For higher pressures ( $p = 50 atm$ ) surface temperature rises continuously. The pseudo wet-bulb state disappears, and the vaporization

process becomes transient in nature during the entire droplet lifetime. For  $p = 100 \text{ atm}$ , the droplet surface even reaches its critical state at  $t = 1 \text{ ms}$ .

In Figs. 4, 5, and 6, the instantaneous distributions of the mixture specific heat, the mixture thermal diffusivity, and the Lewis number, respectively, are reported at different times for  $p = 100 \text{ atm}$ ,  $T_\infty = 1000 \text{ K}$  and  $T_0 = 90 \text{ K}$ . These figures show the extreme space and time variations of the transport properties. In addition, figure 4 clearly shows the weak divergence of the specific heat around the critical conditions. The Lewis number, defined as  $Le = \lambda/\rho c_p D$  and reported in Fig. 6, characterizes the relative significance of thermal diffusion to mass diffusion.

Figure 7 presents the time evolution of the reduced droplet diameter squared at various pressures. For supercritical regimes, we follow the critical temperature regression. For low pressures, the behavior follows that predicted by the quasi-steady theory assumption. However, at high pressures, the variation becomes nonlinear with respect to time. The slope  $dD^2/dt$  is even almost infinite at the beginning of the process, because of the infinite temperature gradient at the droplet surface.

In Fig. 9, the droplet lifetime is reported for various ambient temperatures as a function of the reduced pressure  $p_r = p/p_{cO_2}$ . This figure uses logarithm scales on both axes. The plots exhibit two different slopes, depending on whether the vaporization regime is subcritical or supercritical. For subcritical regimes, the droplet lifetime decreases with ambient pressure, mainly because of the reduced enthalpy of vaporization. For supercritical regimes, the droplet behavior is then dominated by heat diffusion. The decrease of critical mixture temperature associated with the increase of thermal conductivity with pressure leads to a decreasing droplet lifetime with pressure. One interesting feature is that no abrupt change is noticeable at the transition despite the vanishing of enthalpy of vaporization. As critical conditions are approached, for pressures slightly above the critical pressure of pure oxygen, specific heat of the mixture exhibits a divergence, see Fig. 4. The closer the pressure is to the critical pressure of pure oxygen, the stronger is this divergence. Then, as critical conditions are approached, although the heat consumed by vaporization process becomes smaller, the heat needed to increase the droplet surface to its critical value becomes bigger. These two conflicting effects tend to balance.

Figure 8 presents the time evolution of the reduced droplet diameter squared at various pressures. Contrary to the previous figure, the critical interface is now defined as the critical composition line. This lead to results substantially different from the ones presented in Fig. 7. In Fig. 6, one can notice that the Lewis number is smaller than unity in the gaseous region close to droplet surface. Thus, heat transfer penetrates faster the droplet interior than molecular transfer, all the more so that pressure is high. Then, critical composition line is blown away from the liquid core. Eventually it reaches regions where molecular diffusion is more efficient, higher temperature regions leading to a Lewis number bigger than unity. For supercritical regimes, the final stage of the droplet lifetime is characterized by a high regression rate. For low ambient temperature, where favorable conditions for efficient molecular diffusion are more difficult to find, this mechanism may lead to an increase of the droplet lifetime for high pressure, with a minimum occurring for an intermediate pressure greater than oxygen critical pressure. This feature is reported in Fig. 10, which present the droplet lifetime as a function of the reduced pressure  $p_r = p/p_{cO_2}$  for various ambient temperatures. With the critical interface based on critical composition, no significant change is noticeable at the transition from subcritical to supercritical regimes.

Let us briefly comment on the influence of the cross-diffusion effects, namely the Soret and Dufour effects. Two series of computations, with and without taking into account these effects, have been conducted. These computations are reported in Figs. 11 and 12. It is important to note that both axis use linear scale. The influence of thermal diffusion is noticeable for subcritical pressures as well as for supercritical pressures when the critical interface is defined as the critical composition line. The most visible effect of thermal diffusion is the fact that heavier molecules are attracted by low temperature zones and vice versa for lighter molecules. In our case, hydrogen is attracted by hotter regions while oxygen tends to stay in cooler regions. For the subcritical case, since the hydrogen diffusion flux at the interface is smaller, the thermodynamic equilibrium is displaced to smaller temperatures (See Fig. 1). Figure 2 demonstrates that it leads to a slightly higher vaporization enthalpy. This phenomenon tends eventually to increase the droplet lifetime. For supercritical regimes, when the critical interface is based on

critical composition, the rate of vaporization is controlled by the species transport. The droplet lifetime is affected by cross-diffusion effects. Once again, the droplet lifetime is increased in comparison to the case without thermal diffusion. The Soret effect tends to keep oxygen in the cold region, the critical composition line corresponds then to a lower temperature where species transport is globally less efficient.

Our estimation of thermal diffusion coefficients should be restricted to low pressures. Such low-pressure estimations lead to thermal coefficients independent of pressure, which is more likely questionable. In fact, the dependency of thermal diffusion coefficients with respect to pressure must be roughly the same that for molecular diffusion coefficients. Thus, in our study, effect of cross-diffusion have been over-estimated for moderate and high pressures. Furthermore, since this effect tends to increase the droplet lifetime by less than a few percents, we do not consider it in the following presented results.

#### *4.3. Limits of Critical Regimes*

Since, for subcritical regimes, evolutions of temperature and compositions are linked by the thermodynamic equilibrium, the evolution of interface conditions is monitored both by heat transfer (evolution of temperature) and species transport (evolution of composition). The limit of occurrence of supercritical regimes, in terms of ambient conditions, is then a strong function of the estimation of transport properties. In Fig. 13, the limit ambient temperature, at which critical conditions are reached, is plotted for various pressures, and two initial droplet temperatures, 90 and 110 K, respectively. The dashed lines correspond to a supercritical regime reached after 1 % of droplet mass is vaporized, the solid line corresponds to a supercritical regime reached at the end of the droplet lifetime. For a pressure-temperature couple located in the region above the solid line, supercritical regime occurs during the droplet lifetime. For pressures above the double of the critical pressure of pure oxygen, supercritical regimes are reached almost instantaneously whatever the ambient temperature is. There are two major explanations of this phenomenon. First, as pressure increases, the mixture critical temperature decreases (See Fig. 1). Consequently, a droplet can reach its critical conditions more easily at a higher pressure. Second, the molecular diffusion coefficient is a decreasing function of pressure.

Then, since hydrogen will diffuse less at higher pressures to the droplet surface, critical conditions will be easier to reach. There is another interesting application of the last point: if the hydrogen ambient composition is decreased or if oxygen ambient composition is increased, by considering for instance a mixture of hydrogen and oxygen, the limit temperature for supercritical regime will decrease with respect to the ones presented in Fig. 13. To conclude with this point, the comparison of results obtained for two different initial droplet temperatures demonstrated that the limit temperature of occurrence of supercritical regime is also a function of the initial droplet temperature; the cooler the droplet is initially, the hotter ambient gas must be in order to reach supercritical regime. This effect is stronger for relatively low pressures.

Umemura (1986)

developed a theoretical model of droplet vaporization under supercritical conditions. The model was one-dimensional with a planar geometry, which enabled the author to find a self-similar solution to the transient problem. With a reasoning involving molecular and heat fluxes at the interface as well as the slope of the equilibrium curves of Fig. 1, Umemura stated that any thermodynamic model, in order to be consistent, requires that molecular diffusion coefficient vanishes at the mixture critical point. This phenomenon, which was observed experimentally by Sengers (1972) may be understood simply as follows. For subcritical regimes, as thermodynamic equilibrium exists, a difference in liquid and gaseous composition at the interface exists. Since interface thickness is assumed to be infinitely small, the gradient of composition is then infinite. As molecular flux remains finite one may consider that the molecular diffusion coefficient must vanish across the interface. This feature must remain true as temperature is increased to the critical value. However, since there is no accurate modelization of this phenomenon in the literature, we did not implement it in our numerical model. From the previous discussion, we can easily understand that this phenomenon influences the limit values of temperature of supercritical regime occurrence reported in Fig. 13. These latter values are then expected to be smaller than the ones presented.

## 4.4. Approximate Analysis

In this section, the attention is focused on the estimation of the droplet lifetime restricted to supercritical vaporization regimes, when this regime occurs soon after the liquid droplet have been exposed to the hot gaseous ambient atmosphere, that is when ambient pressure and temperature are located above the dashed lines of Fig. 13. The critical interface is based on the mixture critical temperature. In this case, as mentioned in the previously, the problem is entirely driven by heat conduction. In order to obtain an analytical solution, a simplified analysis of this problem may be conducted. Simplifying hypotheses are thus needed: thermal conductivity, specific heat and thermal diffusivity  $\alpha = \lambda/\rho c_p$  are constant in both space and time. In addition, the Stefan flow induced by vaporization is assumed to be negligible. Thus, the problem reduces to the resolution of the following partial derivative equation

$$\frac{\partial T}{\partial t} = \alpha \frac{1}{r^2} \frac{\partial}{\partial r} \left( r^2 \frac{\partial T}{\partial r} \right) \quad (4.3)$$

Using thermal diffusivity, initial droplet radius, initial droplet temperature, and ambient temperature, we can substitute in this equation the dimensionless quantities:  $r^* = r/R_0$ ,  $t^* = t\alpha/R_0^2$ , and  $T^* = (T_\infty - T)/(T_\infty - T_0)$ , to obtain

$$\frac{\partial T^*}{\partial t^*} = \frac{1}{r^{*2}} \frac{\partial}{\partial r^*} \left( r^{*2} \frac{\partial T^*}{\partial r^*} \right) \quad (4.4)$$

Considering the initial temperature distribution, for  $t^* = 0$

$$\begin{cases} T^*(r^*, 0) = 1 & , & \text{for } r^* \leq 1 \\ T^*(r^*, 0) = 0 & , & \text{for } r^* > 1 \end{cases}$$

The solution of Eq.(4.4) was given by Rosner (1967). At that time Rosner was interested in the burning time of droplets experiencing supercritical vaporization. The equation concerned the mass fraction, and by tracking the stoichiometric location, it gave prediction of the burning time. Nevertheless, the solution for reduced temperature may be given by

$$\begin{aligned} T^*(r^*, t^*) = & \frac{1}{2} \left[ \operatorname{erf} \left( \frac{1+r^*}{\sqrt{4t^*}} \right) + \operatorname{erf} \left( \frac{1-r^*}{\sqrt{4t^*}} \right) \right] \\ & - \frac{\sqrt{t^*}}{\sqrt{\pi} r^*} \left\{ \exp \left[ \left( \frac{1-r^*}{\sqrt{4t^*}} \right)^2 \right] - \exp \left[ \left( \frac{1+r^*}{\sqrt{4t^*}} \right)^2 \right] \right\} \end{aligned} \quad (4.5)$$



If the classical definition of the critical interface based on the mixture critical temperature is used, from the previous formulation, the reduced droplet lifetime  $\tau^*$  is demonstrated to be only a function of the reduced critical temperature,  $T_c^* = (T_\infty - T_c)/(T_\infty - T_0)$ , and thus solution of the equation

$$T_c^* = \operatorname{erf}\left(\frac{1}{\sqrt{4\tau^*}}\right) - \frac{1}{\sqrt{\pi\tau^*}} \exp\left(-\frac{1}{4\tau^*}\right) \quad (4.6)$$

#### 4.5. Final Droplet Lifetime Results

A large series of numerical simulations have been conducted for various ambient temperatures and pressures and for two initial droplet temperatures:  $T_0 = 90$  and  $110$  K, respectively. The former corresponds to the lower limit of LOX injection temperature in many operational rocket engines, the latter is used to determine the effect of initial droplet temperature and is slightly under critical temperature for pressure of  $300$  atm. Ambient temperatures were chosen in the range  $500 \leq T_\infty \leq 2500$  K, and ambient pressures  $p_c \leq p \leq 300$  atm. Of course some of the computations may not meet the requirement of quick criticality and will present significant differences from the other ones. This particular case is however representative of most of the cases: liquid and gaseous thermal diffusivity differ by several orders of magnitude. It is due to the difference between oxygen and hydrogen behavior, as well as to the temperature difference between both phases. It appears clearly that the characteristic heat-up process in the liquid phase is the limiting process of droplet vaporization. Using this observation, Figure 14 shows, for all the performed computations, the dimensionless droplet lifetime  $\tau^* = \tau \alpha_0^l / R_0^2$  as a function of the reduced critical temperature  $T_c^*$ , where  $\alpha_0^l$  denotes the initial liquid thermal diffusivity. The solid line corresponds to theoretical predictions from resolution of Eq.(4.6). The filled dots correspond to computations that do not meet the fast criticality requirement, ambient pressure and temperature located under the dashed lines of Fig. 13.

Unfortunately no line meets all the data points, clearly because it involves many features which are not included in the simplified analysis. First, the convection induced by the vaporization process was not considered in the analysis. This effect reduced the overall heat flux arriving at the droplet surface and, if it was included in the previous

theory, it would shift up the solid line of Fig. 14. However, this effect is more likely to be small. Since the process is entirely driven by heat diffusion, the space distribution of thermal diffusivity must be determinant, all the more that liquid and ambient thermal diffusivity differ by several orders of magnitude. Figure 5 demonstrates that the thermal diffusivity at the droplet surface is very close to the liquid thermal diffusivity; the same remark may be done for thermal conductivity. The heat flux arriving at the droplet surface is the product of the interface thermal conductivity multiplied by the local temperature gradient. The interface thermal conductivity is almost unchanged during the entire droplet lifetime, but the interface temperature gradient varies. It may roughly be estimated as follows

$$|\nabla T|_s \approx \frac{T_\infty - T_c}{\sqrt{\alpha_\infty t}} \quad (4.7)$$

As the ambient thermal diffusivity increases, the interface temperature gradient is reduced so that the droplet lifetime is expected to be longer with respect to the case where thermal diffusivity is space constant. It is then logical to correct the results presented in Fig. 14 by a factor dependent of the ratio  $\alpha_\infty/\alpha_0^l$ . By analyzing in details the results, it seems that, when  $\alpha_\infty/\alpha_0^l$  increases, the correction factor reaches an asymptotic value. Thus, the following correcting factor has been chosen

$$f(\alpha_\infty/\alpha_0^l) = 1 + 3.9 [1 - \exp(-0.035 (\alpha_\infty/\alpha_0^l - 1))] \quad (4.8)$$

Figure 15 presents the corrected reduced droplet lifetime for the various computational cases,  $\tau_{corrected}^* = \tau \alpha_0^l / (R_0^2 f(\alpha_\infty/\alpha_0^l))$ . This lifetime may now be easily correlated to the reduced critical temperature by means of a linear function (represented with the dashed line in the figure), the expression of the droplet lifetime is given by

$$\tau = [0.0115 + 0.542 (1 - T_c^*)] \frac{R_0^2}{\alpha_0^l} f(\alpha_\infty/\alpha_0^l) \quad (4.9)$$

The average error from this relation is 5.2 %, while the maximum error for the presented results is around 10 %. Application of Eq.(4.9) constitutes then an excellent estimation technique of the droplet lifetime for supercritical regimes. In addition, it may be extended to moderate supercritical pressures (filled dots of Fig. 15) with satisfying agreement. The expression of  $T_c^*$  may be related to a Spalding number, which has more physical

---

	Oxygen	Hydrogen	Water
$p_c$ (atm)	49.8	12.8	218.3
$T_c$ (K)	154.6	33.1	647.3

---

TABLE 1. Critical properties

significance, as follows

$$B_T = \frac{T_\infty - T_c}{T_c - T_0} = \frac{T_c^*}{1 - T_c^*} \quad (4.10)$$

This correlation shows clearly that pressure affects the droplet lifetime through its effect on the mixture critical temperature and on the ambient thermal diffusivity.

## 5. Vaporization in Hydrogen/Water Mixtures

In a real rocket engine combustion chamber, the ambient environment seen by a liquid oxygen droplet is not exclusively composed of hydrogen. One must consider at least the main combustion product issued from the reactive mechanism, that is water. However the resolution of the problem is not straightforward and needs further considerations.

### 5.1. Condensation of Water

Water critical properties are much higher than the ones of both hydrogen and oxygen (See table 5.1). Water is much less volatile than oxygen and hydrogen. Consequently its liquid state exists for higher temperatures and pressures. Applied to our problem, it may have the following consequence: when gaseous water diffuses towards the oxygen droplet surface, a non-negligible amount of gaseous water may reach low temperature regions so that water partial pressure becomes bigger than its saturation pressure. Gaseous water may then experience a phase change leading to formation of ice/water particles. There is no way to elude the problem by assuming that condensation process is negligible because the incompatibility between gaseous water concentrations and local temperatures will lead to somehow unsolvable problems of density computations. In the following analysis, we consider that gaseous water may experience only one phase change, that is condensation; transition from liquid to solid state or direct transition from gaseous to solid state are not considered.

The condensation mechanism is complex and involves different processes such as nucleation and particles growth by germination. In addition, particles may interact with the gaseous flow and with other particles: particles coalescence. The purpose here is not to treat the entire problem induced by condensation because it will require the development of a sophisticated spray model which may overlap our initial study set. However, by analyzing the features of all the processes involved, a simplified modelization of the condensation can be obtained.

Particle formation is attributed to nucleation of molecular clusters called embryos. As the saturation ratio, defined as the ratio of the partial water vapor pressure to the water saturation pressure ( $S = p_{H_2O}/p_{sat}$ ) increases above unity, embryos larger than a critical size become stable droplets, see Reist (1984). Droplets of critical size,  $R_{pc}$  are called nuclei, and can be estimated from the Kelvin equation given by Mc Donald (1962)

$$R_{pc} = \frac{2\sigma}{R_u \rho_p T \ln S} \quad (5.1)$$

$\sigma$  is the surface tension of water and  $\rho_p$  its density, respectively approximately equal to  $7.5 \cdot 10^{-2} \text{ N/m}$  and  $1000 \text{ kg/m}^3$ . The expression is defined only for saturation ratios greater than one. For saturation ratios less than one, embryos disintegrate as rapidly as they form. Figure 16 present results of Eq.(5.1) for different representative temperatures. We consider that nucleation process is not influence by foreign molecules (oxygen and hydrogen) and is thus homogeneous; the nucleation rate per unit volume is determined by statistical thermodynamics, see Rogers & Yau (1989)

$$J = 4\pi R_{pc}^2 Z \frac{p_{H_2O}}{\sqrt{2\pi W R_u T}} \frac{\rho_{H_2O} N^2}{W} \exp \left( -\frac{4\pi R_{pc}^2 \sigma N}{3 R_u T} \right) \quad (5.2)$$

where the factor  $Z$  denotes the Zeldovich factor, which has a numerical value in order  $10^4$  when all quantities are measured in SI units.  $N$  is the Avogadro number. By combining Eqs.(5.1) and (5.2), the nucleation rate is expressed as a function of the saturation ratio and temperature. We may express, for a given gaseous water density  $\rho_{H_2O}$ , the characteristic time of nucleation  $\tau_{nucleation}$  defined by the relation

$$\rho_{H_2O} = \frac{4}{3} \pi R_{pc}^3 \rho_p J \tau_{nucleation} \quad (5.3)$$

From the three previous relations, this characteristic nucleation time may be expressed

as a function of temperature and saturation ratio. Figure 17 presents for different temperatures the nucleation time function of saturation ratio. This characteristic time is extremely sensitive to the saturation ratio. Thus for saturation ratios above 10 it becomes smaller than  $10^{-10}$  s and nucleation process may be considered as instantaneous with respect to our vaporization process which characteristic time is close to  $10^{-3}$  s. For such saturation ratios, the critical nuclei radius is between  $10^{-10}$  m and  $10^{-9}$  m, each nuclei is then composed of a few water molecules.

When expressing nucleation time function of temperature and saturation ratio, we have expressed the saturation pressure as a function of temperature. Such expressions derived from experimental data are available in the literature, see for example Reid, Prausnitz & Poling (1987). In these expressions, saturation pressure exhibits an exponential dependency with respect to temperature: it vanishes rapidly as temperature decreases. When liquid oxygen droplet vaporizes, the region which is likely to shelter the water condensation process corresponds most of the time to a large temperature gradient region. Then, considering that nucleation process occurs for saturation ratios around 10 or occurs at local thermodynamic equilibrium ( $S = 1$ ) will generate only small discrepancies. In addition, by only taking into account homogeneous condensation, we may have overestimated the characteristic nucleation times for saturation ratios close to one. As a matter of fact gaseous oxygen and hydrogen molecules are expected to influence the nucleation process. Based on these considerations, we have modeled very simply nucleation process as occurring for saturation ratios equal to one, and almost instantaneously. This hypothesis is equivalent to consider local thermodynamic equilibrium. Some computations were carried out with nucleation process occurring for saturation ratios above 1 and demonstrated only negligible differences.

After their formation, condensed particles interact with the gaseous flow. Water particles are submitted to thermophoretic and viscous forces. The former effect tends to attract heavier molecules or small particles to low temperature regions, as was discussed by Talbot *et al.* (1980). Condensed particles will thus be attracted by oxygen droplet surface. Expressions for thermophoretic forces are based on the derivations of Epstein (1929) corrected by Brock (1962) to take into account non-quiescent environment, the expression

of the one-dimensional radial thermophoretic force is obtained

$$F_T = - \frac{12\pi\mu^2 R_p C_s (\Lambda + C_t Kn)}{\rho(1 + 3C_m Kn)(1 + 2\Lambda + 2C_t Kn)} \frac{1}{T} \frac{\partial T}{\partial r} \quad (5.4)$$

where non subscribed quantities refer to the gaseous environment and  $\Lambda$  represents the ratio of gas thermal conductivity to particle thermal conductivity. The Knudsen number  $Kn$  is defined as the ratio of molecular mean free path to particle radius

$$Kn = \frac{\lambda}{R_p} = \frac{1}{R_p} \frac{2\mu}{\rho\sqrt{8R_u T/\pi}} \quad (5.5)$$

In Eq.(5.4) the constants  $C_s$ ,  $C_t$  and  $C_m$  are derived from kinetic theory and have been assigned the values of 1.17, 2.18, and 1.14, respectively. Brock's equation yields good predictions whatever the ratio  $\Lambda$  is. Moreover, Talbot *et al.* (1980) has shown that it exhibits only 3 % error in the collisionless limit,  $Kn \rightarrow \infty$ , although it was originally designed for small values of the Knudsen number. Since nuclei are typically of order of the molecular mean free path, viscous forces were modeled using the Stokes-Cunningham equation

$$F_v = \frac{6\pi\mu R_p}{C_c} (v - v_p) \quad (5.6)$$

where  $v$  and  $v_p$  are the flow and particles velocities, respectively. The Cunningham correction coefficient  $C_c$ , defined as

$$C_c = 1 + Kn \left[ 1.257 + 0.4 \exp \left( -\frac{1.1}{Kn} \right) \right], \quad (5.7)$$

has been introduced by Carlson & Haglund (1964) into the Stokes-flow expression to account for non-continuum effects coincident with water particles sizes of the molecular mean free path in the suspending fluid. Assuming that thermophoretic and viscous forces are the only forces acting on the particle, the equation of motion describing particle dynamics can be written as

$$\frac{4}{3}\pi R_p^3 \rho_p \frac{dv_p}{dt} = F_v + F_T \quad (5.8)$$

Actually a terminal velocity is reached when the net force acting on particles is equal to zero. The expression is obtained by equating Eqs.(5.4) and (5.6). Let us now consider the time needed to reach this mechanical equilibrium which expression may be easily

obtained from previous equations

$$\tau_{\text{mechanical equilibrium}} = \frac{R_p^2 \rho_p C_c}{18\mu} \quad (5.9)$$

Figure 18 presents this mechanical equilibrium characteristic time as a function of particle radius. Since, once again, this characteristic time is by several order of magnitude smaller than the characteristic time of liquid oxygen vaporization, we may consider that particle velocity is almost instantaneously equal to its terminal velocity given by

$$v_{p,\text{terminal}} = v - \frac{2C_c C_s \mu (\Lambda + C_t Kn)}{\rho (1 + 3C_m Kn) (1 + 2\Lambda + 2C_t Kn)} \frac{1}{T} \frac{\partial T}{\partial r} \quad (5.10)$$

Numerical experiments show that the second term on the right hand side of Eq.(5.10) is much smaller than the first one. Thus particle velocity is very close to gaseous flow velocity. Furthermore, since the particle radius effect is entirely included in this term, the overall effect of condensed particle size is then expected to be small or even negligible. A full treatment of water condensation process would require a different treatment of each condensed particle depending on its size. Since each particle would grow or decrease depending on the local saturation conditions, and since each particle may collide with other particles, tracking each particle size and position would necessitate a sophisticated modelization. From previous considerations such modelization seems unnecessary and we may consider that, as a first approximation, each condensed particle has the same radius, taken to be equal to  $10^{-2} \mu m$ .

The condensation process may now be modeled simply. It can be reduced to the addition of mass sink term,  $-\dot{m}_{\text{cond},H_2O}$  in the balance equation of mass, Eq.(2.1), and a source term,  $\Delta H_{\text{vap},H_2O} \dot{m}_{\text{cond},H_2O}$  in the balance equation of energy, Eq.(2.3). The clear parallelism existing between water condensation process and oxygen vaporization process leads us to express these terms with a method similar to the one described previously in Eq.(3.3)

$$\dot{m}_{\text{cond},H_2O} = K_{\text{cond},H_2O} (p_{H_2O} - p_{\text{sat}}) \quad (5.11)$$

However, a significant difference exists between both processes. Water condensation process does not occur at a fixed location. Thus Eq.(5.11) must be applied for the gaseous region adjacent to the droplet surface and limited by the line above which saturation ratio becomes lower to one. This condensation limit is determined by means of an iterative

procedure. Once created, condensed particles are convected by use of Eq.(5.10) and reach zones where saturation ratio is lower than unity. In this case, condensed particles are assumed to disappear almost instantaneously.

Neglecting the contribution of Brownian motion of condensed particles to the pressure, we still can use Eq.(2.8) where  $\rho$  is the gas density. Besides, we assume that the total volume is the sum of each phase volume. The condensed mass volume is related to its mass by the particle density which is considered as independent of pressure and temperature. The numerical implementation of condensation model requires then the insertion of three other quantities: for each grid cell, we compute the condensed particle mass, volume and velocity.

### 5.2. Results and Discussion

We consider now the vaporization of liquid oxygen droplet in gaseous mixture of hydrogen and water for both subcritical and supercritical regimes of vaporization. In this latter case, since for ternary mixtures critical composition line lose most of its signification, only the critical interface based on critical temperature is used. The condensation process does not influence significantly the vaporization process so that results are qualitatively similar to previous ones. This phase change experienced by gaseous water prevents the water to reach oxygen droplet surface. Gaseous water is consumed by the condensation process away from the droplet surface, and condensed particles are blown away by the gaseous flow. Thus, only oxygen and hydrogen are present at the droplet surface and the behavior of the thermodynamic equilibrium is very close to the one described in the previous section. In the Fig. 19, instantaneous distributions of compositions are reported at different times for  $p = 100 \text{ atm}$  and  $T_\infty = 1000 \text{ K}$ . The gaseous compositions are reported to total gaseous mass whereas the condensed phase mass fraction is reported to the total mass of the system. However, condensed mass fraction remains very small during the entire droplet lifetime, eventually dropping to zero as droplet disappears. The accumulation of condensed water in the neighborhood of droplet surface is also rather small. Gaseous water does not diffuse towards the oxygen droplet surface. For the same conditions as Fig. 19, Figure 20 presents the instantaneous distributions of temperature.



Despite the fact that condensation process liberates energy in the gaseous phase, no influence is noted on the temperature profiles, showing once again that condensation process is very weak.

Figure 21 presents, for different ambient pressures and temperatures, the instantaneous location of the condensation limit. The radius is reduced by the instantaneous droplet radius. Condensation first occurs very close to the oxygen droplet surface, for relatively low temperatures. Then, the limit moves away from the droplet reaching higher temperature zones. Effect of ambient pressure on the location of the condensation limit may be simply explained as follows. The condensation region is characterized by the equality of partial pressure of water and its saturation pressure. As the ambient pressure increases, partial pressure of water increases also implying that the temperature of the condensation limit increases. The condensation limit is then moved further from the oxygen droplet surface. Same reasoning may be done to explain ambient temperature effect.

To conclude with qualitative aspects of condensation process we can discuss some of the hypotheses of modelization. First computations were carried out with different particle radii, no significant changes were observed. In the model we only considered one phase change. The treatment of condensed particle dynamics does not consider whether particles are liquid or solid. Considering a different phase change would affect the local thermodynamic equilibrium and the liberation of heat in the gaseous phase. Since the overall aspect of condensation process has been demonstrated to be small, the additive effect of ice particle formation is not expected to change significantly the presented results.

Figure 23 presents the droplet lifetime as a function of reduced pressure for three different ambient compositions, and three different ambient temperatures. Hydrogen composition is chosen from  $Y_{H_2,\infty} = 0.25, 0.50, \text{ and } 0.75$ , respectively. Ambient temperature is chosen from  $T_\infty = 1000, 1500, \text{ and } 2000 \text{ K}$ , respectively. Pressure varies between 10 and 300 atm. First, the curves present obviously the same trend as the oxygen/hydrogen case. Second, the effect of ambient composition is weak. In the Fig. 24 we have reported the reduced droplet lifetime using the same procedure as for the pure hydrogen case. The lifetime is reduced by means of initial liquid thermal diffusivity and initial droplet radius

with the correction factor of Eq.(4.8). Since the straight line appearing in this figure in the same that in Fig. 15, droplet lifetime may be estimated by use of Eq.(4.9). Average and maximum deviations are respectively 4.8 % and 12 % for the presented results.

Since condensation mechanism introduces an other length scale, the droplet lifetime is not simply proportional to the initial squared diameter. However condensation process has been proven sufficiently small to neglect this phenomenon.

## 6. Concluding Remarks

A comprehensive analysis of LOX droplet vaporization in hydrogen and water environments at both sub- and supercritical conditions has been conducted. A special attention has been devoted to transport and thermodynamic properties evaluation. In the case where ambient gas is partly composed of water, a condensation model has been implemented. Results of this model show that condensation occurs in the neighborhood of oxygen droplet surface. The main implication of this phenomenon is that gaseous water does not reach oxygen droplet surface, gaseous water forms small condensed particles which are blown away by the gaseous flow. The overall effect of condensation is however very small and no agglomeration of condensed particles near the droplet surface occurs. Effects of ambient and initial conditions have been investigated in detail. Results indicate that pressure influence is different depending upon whether the vaporization regime is sub- or supercritical. In the case where supercritical regime happens almost instantaneously, the droplet lifetime may be estimated simply by means of a correlation involving ambient and initial conditions. This correlation, derived from physical considerations, presents an average deviation of about 5 %.

## REFERENCES

- BIRD, R.B., STEWART, W.E. & LIGHTFOOD, E.N. 1960 Transport phenomena. John Wiley & Sons, Inc., New York-London.
- BROCK, J.R. 1962 On the theory of thermal forces acting on aerosol particles. *Journal of Colloid Science*, 17, 768-780.
- BRUNO, T.J. & ELY, J.F. 1991 Supercritical fluid technology: reviews in modern theory and applications CRC Press, Inc., Boca Raton.
- CARLSON, D.J. & HAGLUND, R.F. 1964 Particle drag and heat transfer in rocket nozzles. *AIAA Journal*, 2, 35-58.
- CURTIS, E.W. & FARREL, P.V. 1992 A numerical study of high pressure vaporization. *Combustion and Flame*, 90, 85-102.

- DAOU, J., HALDENWANG, P. & NICOLI, C. 1995 Supercritical burning of liquid (LOX) droplet with detailed chemistry. *Combustion and Flame*, 153–169.
- DELPLANQUE, J.P. & SIRIGNANO, W.A. 1991 Transient vaporization and burning for an oxygen droplet at sub- and near-critical conditions. *AIAA Twenty-ninth Aerospace Sciences Meeting & Exhibit, Reno, NV*, 91-0075.
- DIXON-LEWIS, G. 1968 Flame structure and flame reaction kinetics. II. Transport phenomena in multicomponent systems. *Proc. Roy. Soc., A* (307), 111–135.
- ELY, J.F. & HANLEY, H.J.M. 1981 Predictions of transport properties. 1. Viscosity of pure liquids and mixtures. *Industrial and Engineering Chemistry Fundamentals*, 20 (4), 323.
- ELY, J.F. & HANLEY, H.J.M. 1983 Predictions of transport properties. 2. Thermal conductivity of pure liquids and mixtures. *Industrial and Engineering Chemistry Fundamentals*, 20 (4), 90.
- EPSTEIN, P.S. 1929 *Z. Phys.*, 54, 537.
- FAETH, G.M., DOMINICIS, D.P., TULPINSKY, J.F. & OLSON, D.R. 1968 Supercritical bipropellant droplet combustion. *Twelfth Symposium (International) on Combustion, The Combustion Institute*, 9–18.
- GRABOSKI, M.S. & DAUBERT, T.E. 1979 A modified soave equation of state for phase equilibrium calculations. 3. Systems containing hydrogen. *Industrial and Engineering Chemistry Process Design and Development*, 18 (2), 300.
- HSIANG, L.-P. & FAETH, G.M. 1993 Deformation and secondary breakup of drops. *AIAA Thirty-First Aerospace Sciences Meeting & Exhibit, Reno, NV*, 93-0814.
- HSIAO, C.C., YANG, V. & SHUEN, J.S. 1995 Vaporization of liquid oxygen (LOX) droplets in supercritical hydrogen convective environments. Submitted to *Journal of Fluid Mechanics*, 1995.
- HSIEH, K.C., SHUEN, J.S., & YANG, V. 1991 Droplet vaporization in high-pressure environments 1: near critical conditions. *Combust. Sci. and Tech.*, 76, 111–132.
- JIA, H. & GOGOS, G. 1993 High pressure droplet vaporization; Effects of liquid-phase gas solubility. *International Journal of Heat and Mass Transfer*, 36 (18), 4419–4431.
- LAFON, P. & PRUD'HOMME, R. 1994 Droplet combustion models with condensation of the burnt products. *La Recherche Aérospatiale (ONERA)*.
- LAFON, P. 1994 Modélisation et simulation numérique de l'évaporation et de la combustion de gouttes à haute pression. Thèse de doctorat, Université d'Orléans.
- LIN, N.N., OEFELIN, J.C., YANG, V. & SHUEN, J.S. 1994 Aspects of ice/water formation in the vicinity of a liquid oxygen droplet surface. *Unpublished*.
- LITCHFORD, R.J. & JENG, S.-M. 1990 LOX Vaporization in high-pressure, hydrogen-rich gas. *AIAA Twenty-Sixth Joint Propulsion Conference, Orlando, FL*, 90-2191.
- MCDONALD, J.E. 1962 Homogeneous nucleation of vapor condensation. I. Thermodynamic aspects. *American Journal of Physics*, 30, 870–877.
- POWELL, E.E. Simulation of water vapor condensation on LOX droplet surface using liquid nitrogen. *NASA/ASEE Summer Faculty Fellowship Program*, NGT 01-002-099, N89-21749.
- REID, R.C., PRAUSNITZ, J.M. & POLING, E.P. 1987 The properties of gases and liquids. 4th ed, Mac Graw Hill, New York.
- REIST, P.C. 1984 Introduction to aerosol science. MacMillan Publishing Company.
- ROGERS, R.R. & YAU, M.K. 1989 A short course in cloud physics. 3rd ed, Pergamon Press.
- ROSNER, D.E. 1967 On liquid droplet combustion at high pressures. *AIAA Journal*, 5 (1), 163–166.
- SENGERS, J.V. 1972 Transport properties of gases and binary liquids near the critical point. CR 2112, NASA, University of Maryland.
- SHUEN, J.S., YANG, V., & HSIAO, C.C. 1992 Combustion of liquid-fuel droplets in supercritical conditions. *Combustion and Flame*, 89, 299–319.
- TAKAHASHI, S. 1974 Preparation of a generalized chart for the diffusion coefficients of gases at high pressures. *Journal of Chemical Engineering (Japan)*, 74, 417–420.
- TALBOT, L., CHENG, R.K., SCHEFER, R.W. & WILLIS, D.R. 1980 Thermophoresis of particles in a heated boundary layer. *Journal of Fluid Mechanics*, 101, 737–758.
- UMEMURA, A. 1986 Supercritical liquid fuel combustion. *Twenty-First Symposium (International) on Combustion, The Combustion Institute*, 463–471.
- YANG, V., LIN, N.N. & SHUEN, J.S. 1994 Vaporization of liquid oxygen (LOX) droplets in

supercritical hydrogen environments. *Combustion Science and Technology*, **97**, 247-270.

YOSET, D.J. & TURNS, S.R. 1992 Modeling of product condensation in liquid droplet combustion. *Proceedings of 4th Annual Symposium of Propulsion Engineering Research Center, The Pennsylvania State University*, 63-67.

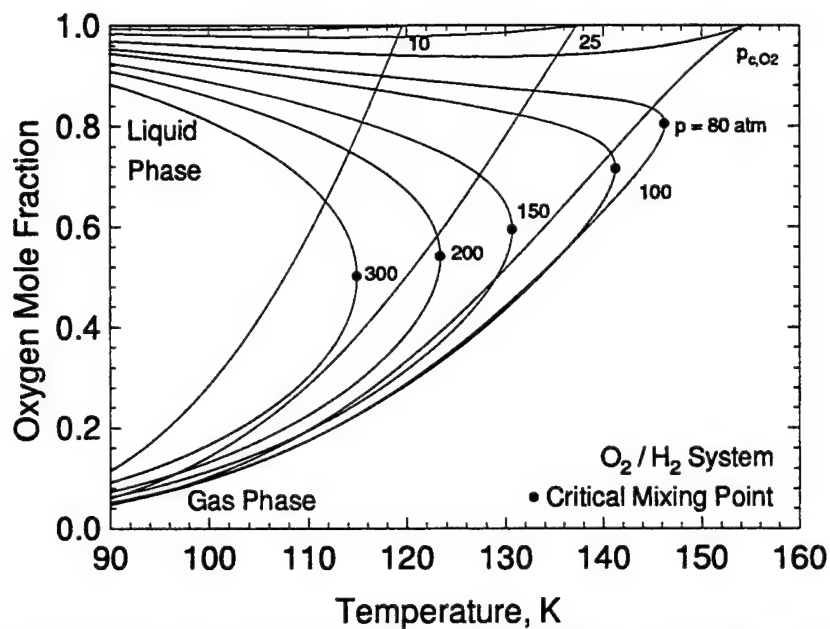


FIGURE 1. Vapor-liquid phase equilibrium compositions for  $O_2/H_2$  at various pressures.

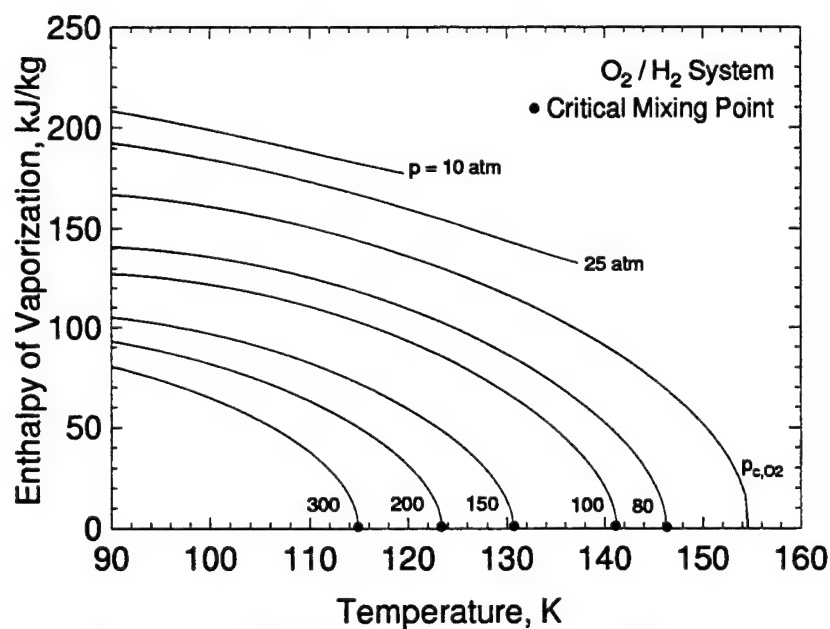


FIGURE 2. Enthalpy of vaporization of  $O_2$  in an equilibrium mixture of  $O_2$  and  $H_2$  at various pressures.

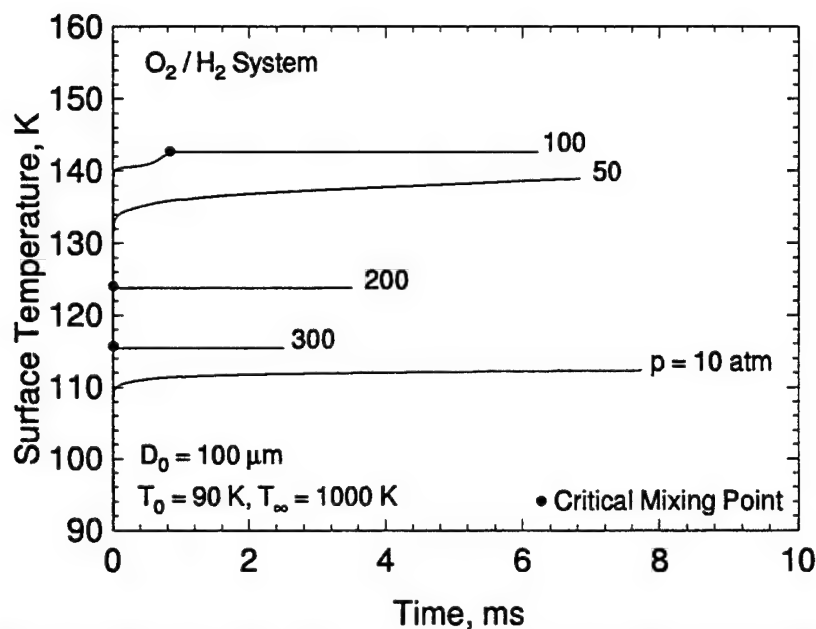


FIGURE 3. Time variations of droplet surface temperature at various pressures;  $T_{\infty} = 1000\text{ K}$ ;  $T_0 = 90\text{ K}$ ;  $D_0 = 100\text{ }\mu\text{m}$ .

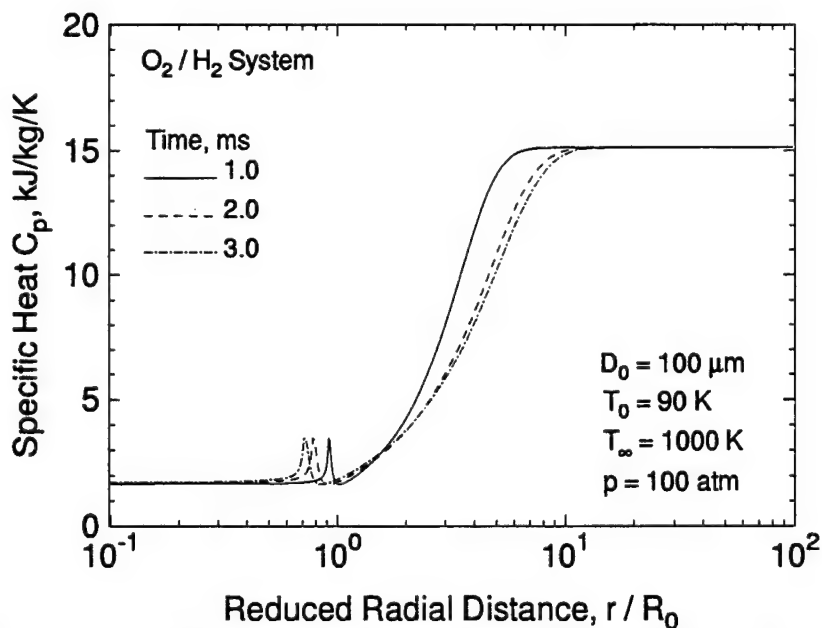


FIGURE 4. Instantaneous distributions of mixture specific heat in the entire field at various times;  $T_0 = 90\text{ K}$ ,  $T_{\infty} = 1000\text{ K}$ ,  $p = 100\text{ atm}$ ,  $D_0 = 100\text{ }\mu\text{m}$ .

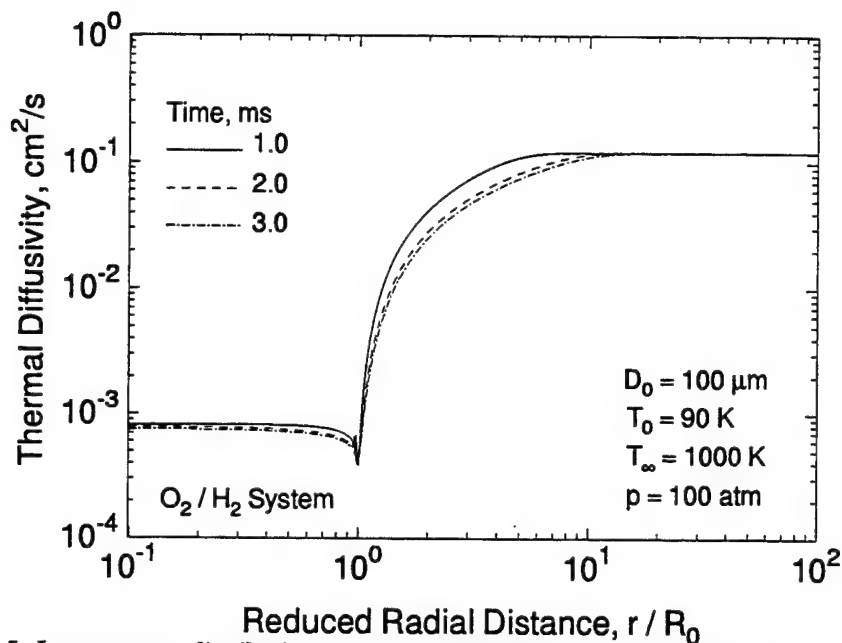


FIGURE 5. Instantaneous distributions of thermal diffusivity in the entire field at various times;  $T_0 = 90 \text{ K}$ ,  $T_\infty = 1000 \text{ K}$ ,  $p = 100 \text{ atm}$ ,  $D_0 = 100 \mu\text{m}$ .

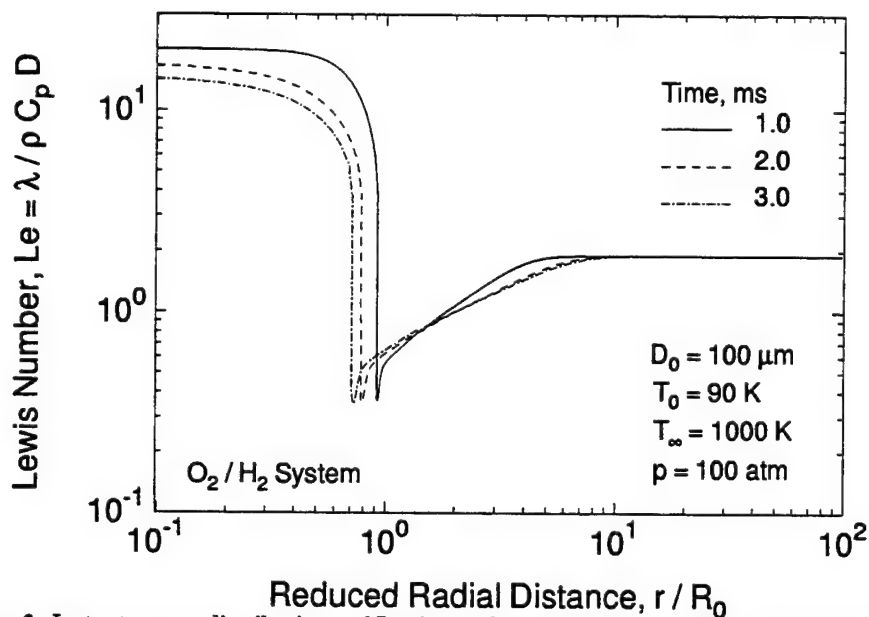


FIGURE 6. Instantaneous distributions of Lewis number in the entire field at various times;  $T_0 = 90 \text{ K}$ ,  $T_\infty = 1000 \text{ K}$ ,  $p = 100 \text{ atm}$ ,  $D_0 = 100 \mu\text{m}$ .

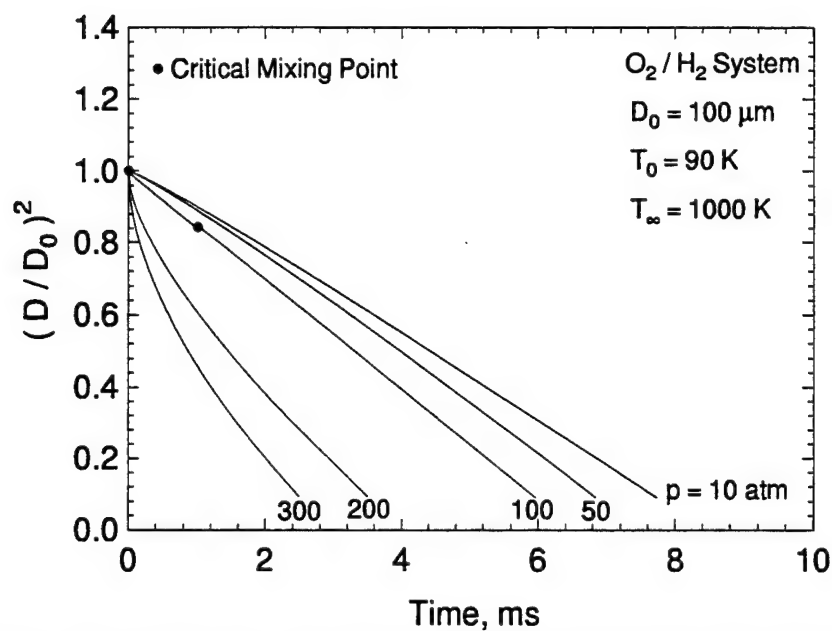


FIGURE 7. Time variations of the square of the reduced diameter at various pressures; critical interface based on temperature;  $T_\infty = 1000 K$ ;  $T_0 = 90 K$ ;  $D_0 = 100 \mu m$ .

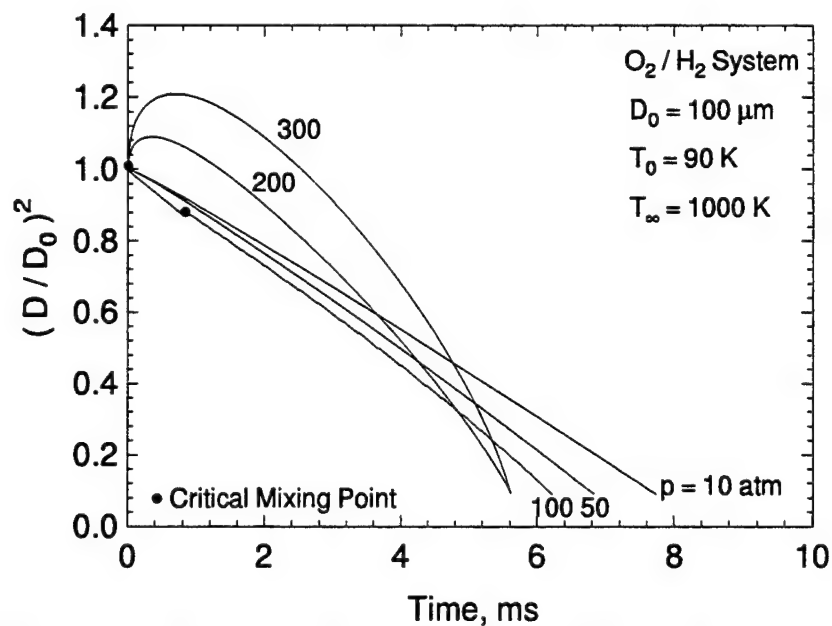


FIGURE 8. Time variations of the square of the reduced diameter at various pressures; critical interface based on composition;  $T_\infty = 1000 K$ ;  $T_0 = 90 K$ ;  $D_0 = 100 \mu m$ .



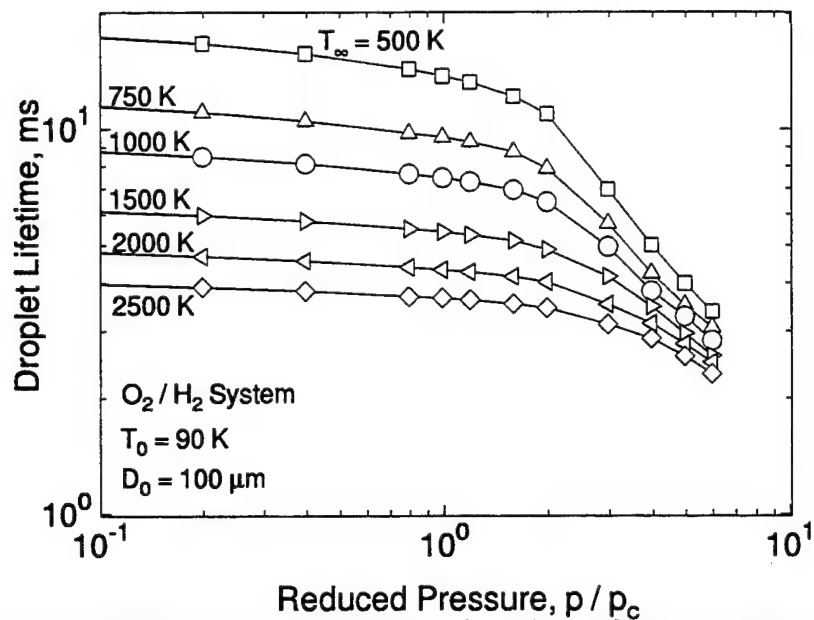


FIGURE 9. Droplet lifetime versus reduced pressure for various ambient temperatures;  $T_0 = 90\text{ K}$ ,  $D_0^2 = 100\text{ }\mu\text{m}$ .

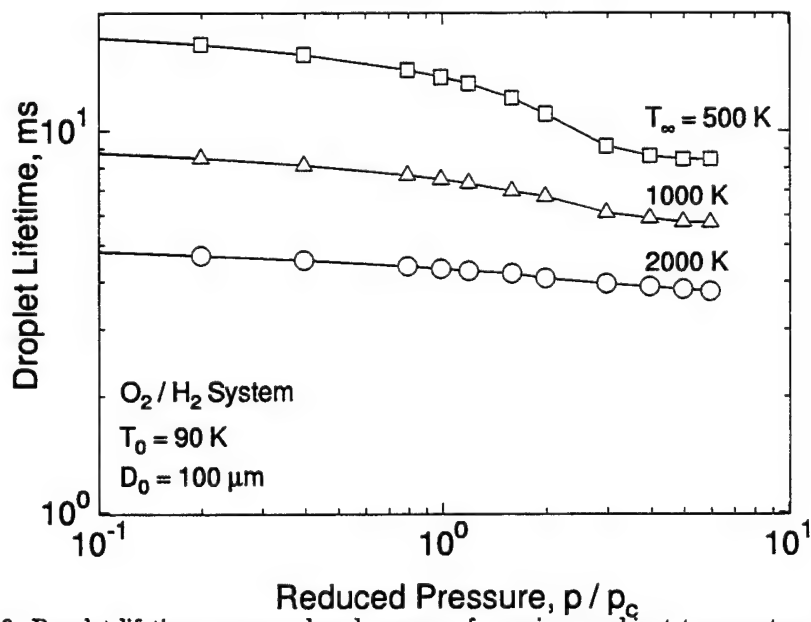


FIGURE 10. Droplet lifetime versus reduced pressure for various ambient temperatures;  $T_0 = 90\text{ K}$ ; critical interface based on composition.

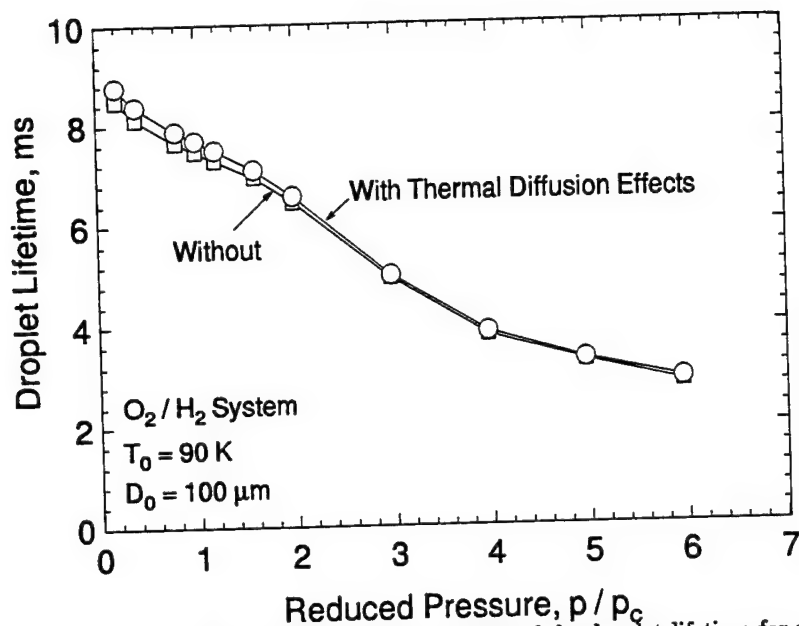


FIGURE 11. Influence of cross-diffusion effects on predictions of the droplet lifetime for various pressures; critical interface based on temperature;  $T_\infty = 1000\text{ K}$ ;  $T_0 = 90\text{ K}$ ;  $D_0^2 = 100\text{ }\mu\text{m}$ .

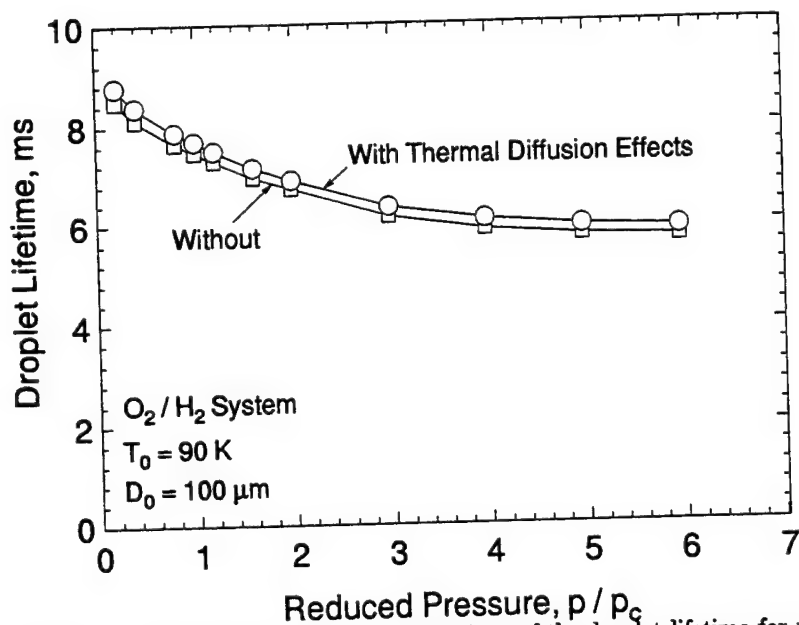


FIGURE 12. Influence of cross-diffusion effects on predictions of the droplet lifetime for various pressures; critical interface based on composition;  $T_\infty = 1000\text{ K}$ ;  $T_0 = 90\text{ K}$ ;  $D_0^2 = 100\text{ }\mu\text{m}$ .

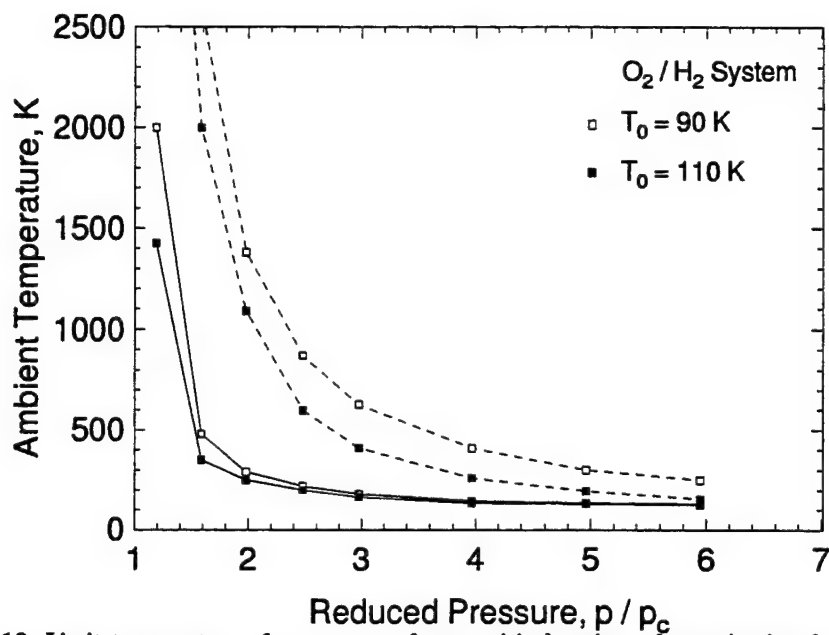


FIGURE 13. Limit temperature of occurrence of supercritical regime of vaporization for two initial droplet temperatures;  $T_0 = 90$ , and  $110$  K.

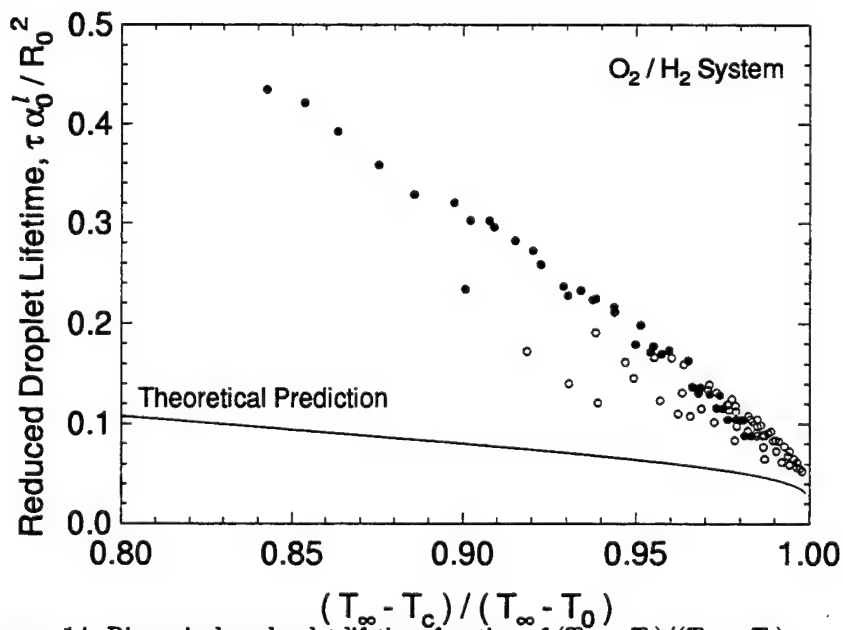


FIGURE 14. Dimensionless droplet lifetime function of  $(T_\infty - T_c) / (T_\infty - T_0)$ .

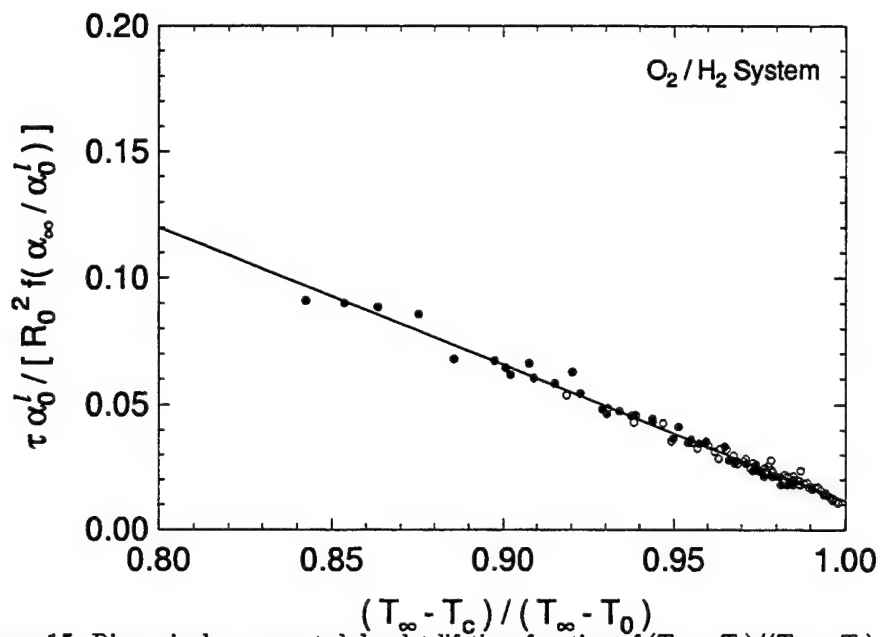


FIGURE 15. Dimensionless corrected droplet lifetime function of  $(T_\infty - T_c)/(T_\infty - T_0)$ .

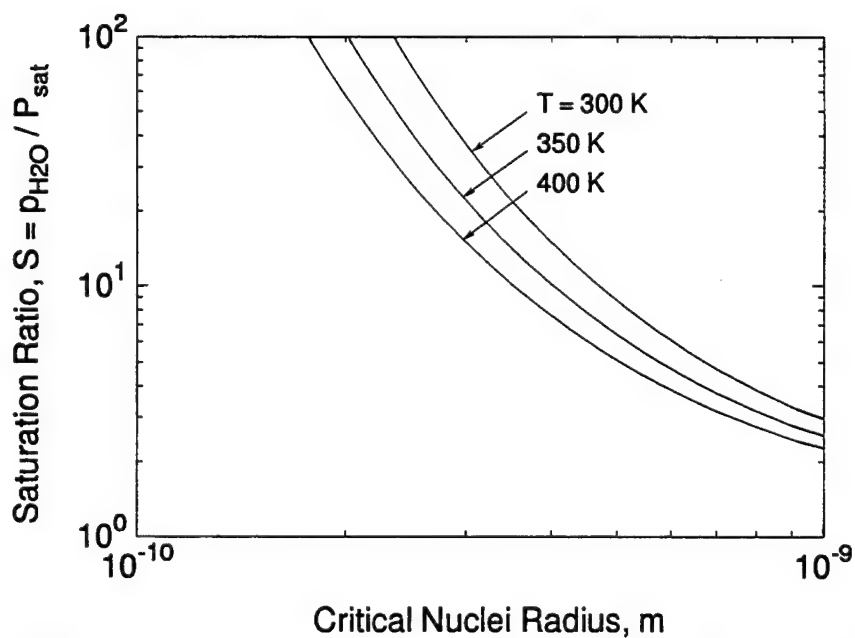


FIGURE 16. Critical nuclei radius function of saturation ratio for different temperatures.

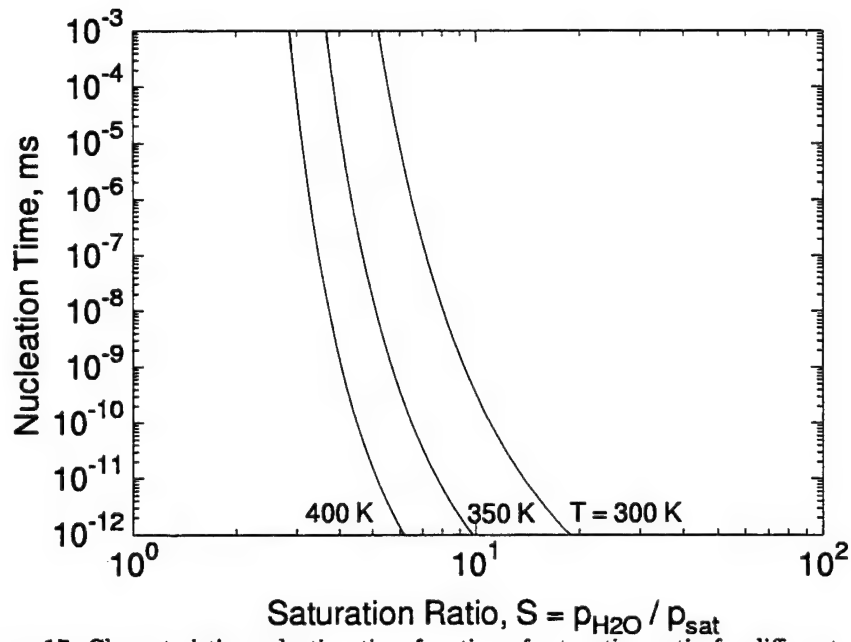


FIGURE 17. Characteristic nucleation time function of saturation ratio for different temperatures.

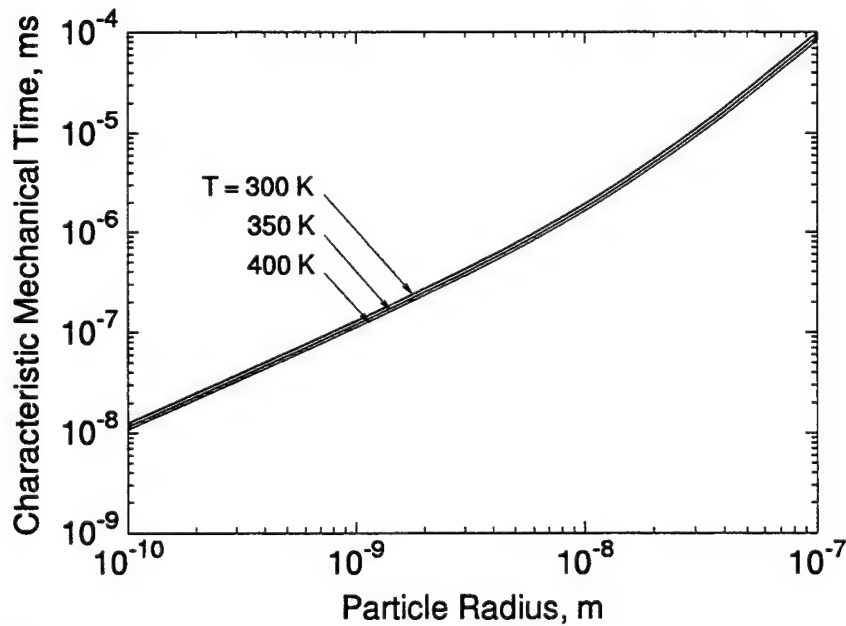


FIGURE 18. Characteristic mechanical equilibrium time function of particle radius for different temperatures.

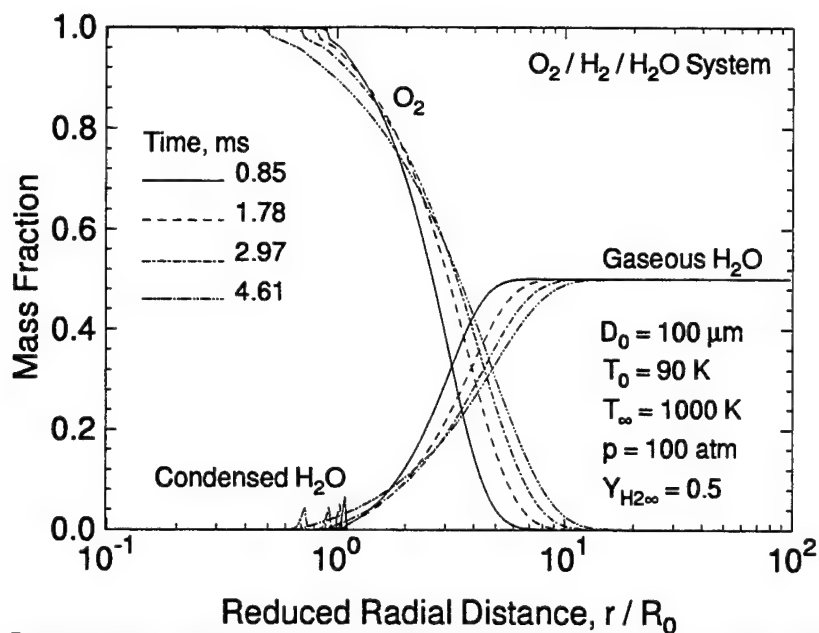


FIGURE 19. Instantaneous distributions of compositions in the entire field for various times,  $LOX/H_2/H_2O$  system.

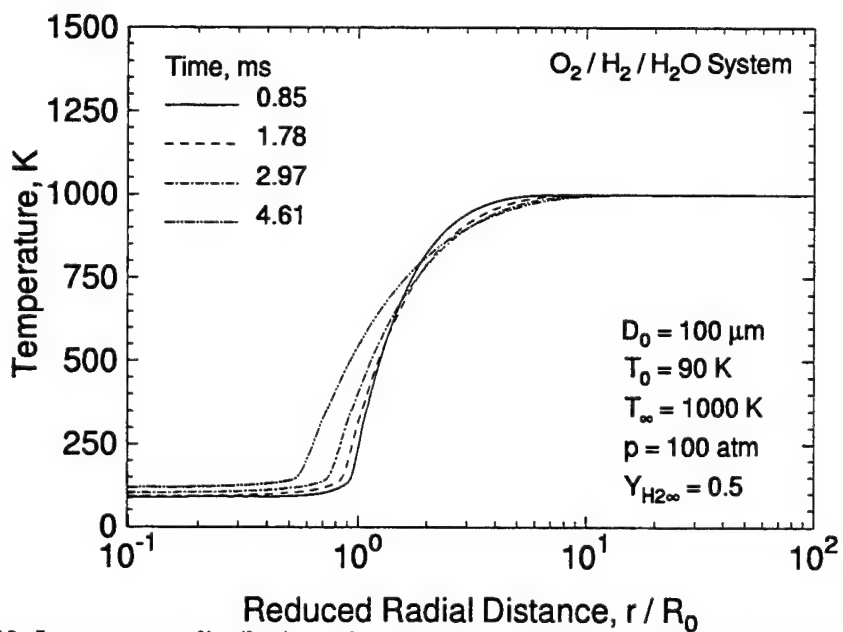


FIGURE 20. Instantaneous distributions of temperature in the entire field for various times,  $LOX/H_2/H_2O$  system.

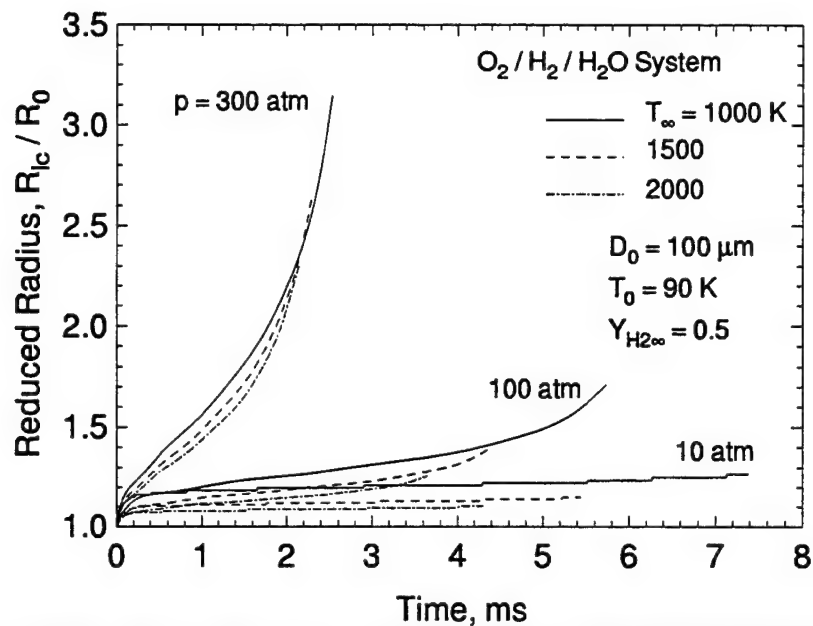


FIGURE 21. Reduced radius of the limit condensation position for different temperatures and pressures.

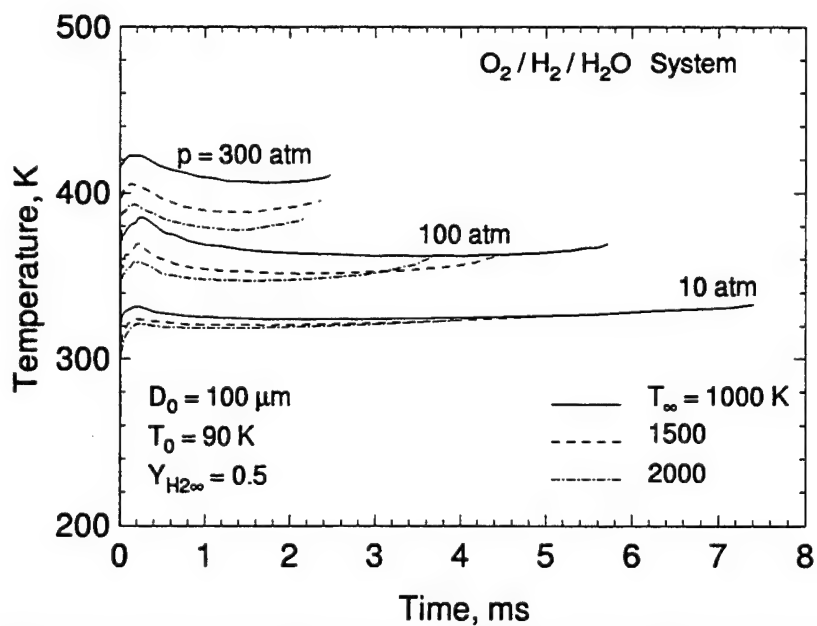


FIGURE 22. Temperature of the limit condensation position for different temperatures and pressures.

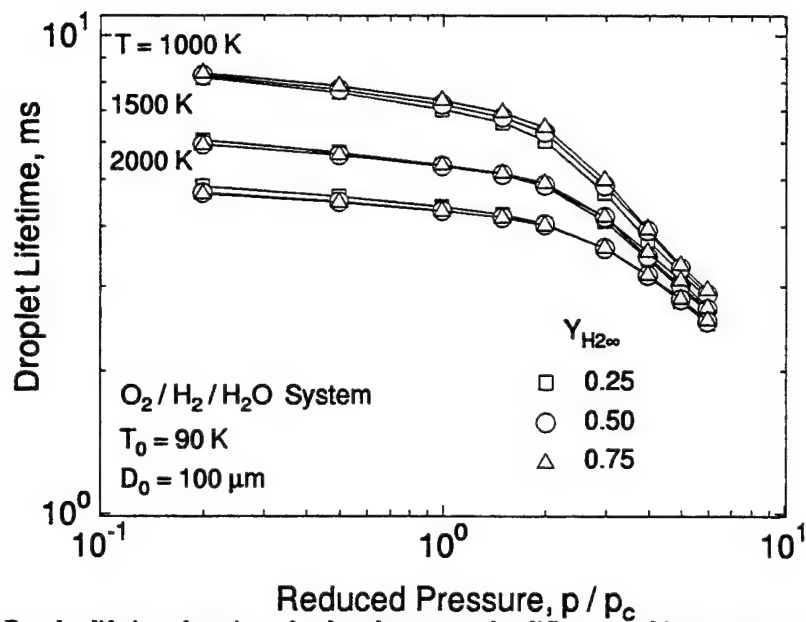


FIGURE 23. Droplet lifetime function of reduced pressure for different ambient temperatures and compositions.

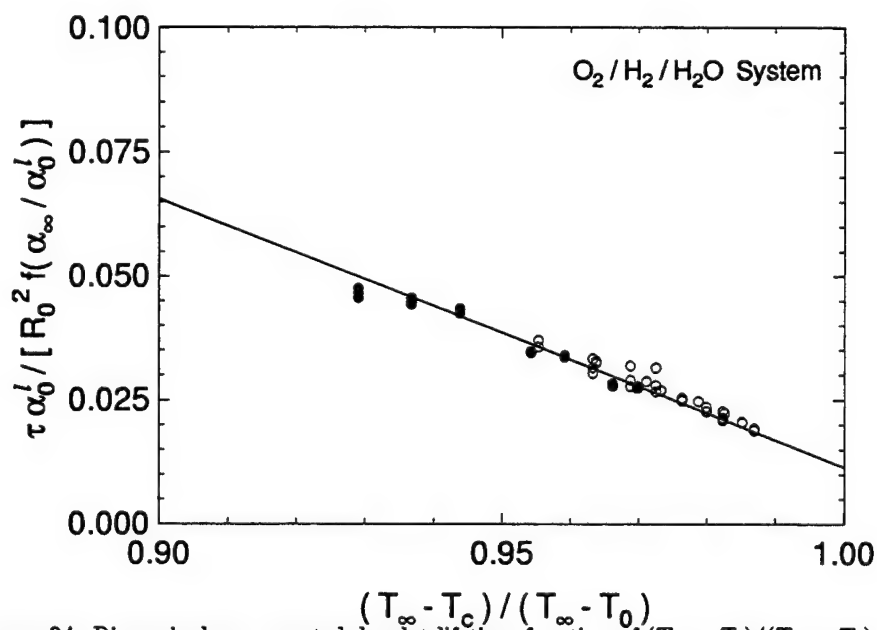


FIGURE 24. Dimensionless corrected droplet lifetime function of  $(T_\infty - T_c)/(T_\infty - T_0)$ .



# Effects of Pressure on Hydrocarbon Fuel Droplet Vaporization in Air

Patrick Lafon

Vigor Yang

## 1 Introduction

In previous publications <sup>5, 6</sup>, we have presented a numerical model for treating droplet vaporization and combustion in quiescent environments over a broad range of thermodynamic conditions. Both subcritical and supercritical regimes of vaporization are studied in detail. The numerical scheme appears quite efficient and allows for a systematic investigation into various underlying mechanisms involved in droplet vaporization. Such studies were carried out for the oxygen/hydrogen system. The goal of the present study is to carry out the same kind of systematic studies for single-component hydrocarbon droplets vaporizing in air.

Three hydrocarbon fuel droplets are considered, *n*-pentane, *n*-heptane and *n*-decane droplets, respectively. These three hydrocarbon species represent a good simple in terms of molecular weight. Let us summarize the characteristics of interest of all the species involved:

## 2 Results and Discussion

A series of computations have been carried out for the three hydrocarbons. Different initial droplet temperatures, different ambient temperatures and pressures have been

---

	<i>n</i> -pentane	<i>n</i> -heptane	<i>n</i> -decane	Nitrogen	Oxygen
<i>W</i>	72.15	100.2	142.3	28.01	32.00
<i>T<sub>c</sub></i> (K)	469.8	540.3	617.5	126.2	154.6
<i>p<sub>c</sub></i> (atm)	33.31	26.94	20.70	33.46	49.77

---

Table 1: Species characteristics

considered. In the present study of pure vaporization, there is only one length scale involved (i.e., droplet diameter).<sup>1</sup> Thus, a dimensional analysis shows that the droplet lifetime is proportional to the square of the initial droplet diameter. Therefore, computations were carried out only for droplets with an initial diameter of 100  $\mu m$ . This does not mean, however, that the  $d^2$ -law is valid regardless of the ambient conditions. This simply means that the transient diffusion processes and time evolution of the surface conditions may be scaled by the square of the initial droplet diameter.

Figures 1, 2, and 3 present droplet lifetimes as a function of reduced pressure for various ambient temperatures, for *n*-pentane, *n*-heptane, and *n*-decane droplets, respectively. Droplet lifetime presents a similar sensitivity to ambient pressure regardless of the hydrocarbon species. The major point to be noted is the difference between low ambient temperature cases and higher ambient temperature cases. For low ambient temperatures, for example  $T_\infty = 400\text{ K}$ , the droplet lifetime first increases with pressure, then levels off and eventually decreases a little bit for high pressures. This behavior remains noticeable although with less amplitude for ambient temperatures up to 750 K. For higher ambient temperatures, the droplet lifetime decreases persistently with increasing pressure. Eventually, when both ambient temperature and pressure are high enough, the droplet surface may reach its critical value. In Figs. 1, 2, and 3, the filled symbols correspond to cases where supercritical vaporization is reached during the droplet lifetime. The dashed line represents the limit of occurrence of both vaporization regimes.

Let us first focus our attention onto the thermodynamic equilibrium process involved at the interface under subcritical vaporization conditions. The numerical scheme uses a kinetic-like relation for the expressions of the species mass flow rate.<sup>5, 6</sup> This technique allows a simultaneous treatment of the thermodynamic equilibrium existing at the interface under subcritical conditions, and of the flux conservation at the interface. In addition, it enables to treat more complex systems than binary systems. In a previous published work<sup>8</sup> concerning *n*-pentane droplet combustion in air, only a binary system was considered, this was justified since due to the combustion mechanism oxygen does not reach the surface. Here, we have to handle a ternary system, which thermodynamic variance is three, and which is thus fully determined for a given temperature, pressure and one species composition in one of the two phases. Computations carried out with the ternary system involved (Hydrocarbon/Nitrogen/Oxygen) show that although oxygen mole fraction in both liquid and gaseous phase is small, it produces some important departures from the binary system (Hydrocarbon/Nitrogen). For example, instantaneous conditions of the thermodynamic equilibrium are monitored by surface composition history, and, contrary to the binary-system case are no longer one-to-one function of the surface temperature.

In Figs. 4 and 5, we have reported for the *n*-heptane/air system the surface composition history as a function of surface temperature for two ambient pressures, respectively  $p = 5, 200\text{ atm}$ . As mentioned previously, compositions are not one-to-one functions of temperature as they were for binary systems. Besides, for a given pressure, critical

coordinates should not be unique. However, as temperature increases, both liquid and gaseous oxygen compositions at the interface becomes smaller and general equilibrium behavior becomes similar to the one of a binary system. In this case, a raise of surface temperature is linked with an increase of *n*-heptane gaseous composition, that is a decrease of nitrogen gaseous composition.

Let us consider figures 6 and 7 in which we have reported respectively final surface temperature and the corresponding enthalpy of vaporization as a function of the ambient pressure. This mixture enthalpy of vaporization is computed from the relation:

$$\Delta H_m = \frac{\sum_i \dot{m}_i (\bar{h}_i^g - \bar{h}_i^l)}{\sum_i \dot{m}_i} \quad (1)$$

Two different ambient temperatures were considered, respectively  $T_\infty = 400 \text{ K}$  and  $T_\infty = 1000 \text{ K}$ . For low ambient temperatures, as pressure increases, the droplet surface temperature first increases then levels off, which may be explained as follows. As pressure increases, molecular diffusion becomes less efficient and nitrogen gaseous composition at the interface is reduced. From observation of equilibrium curves, in Figs 4 and 5, a reduce in nitrogen gaseous composition goes with an increase of surface temperature. Of course, surface temperature cannot become greater than ambient temperature. So, as pressure increases, the temperature gradient at droplet surface becomes small. In the mean time, droplet surface temperature augmentation only weakly affects the value of vaporization enthalpy. In conclusion, when ambient pressure increases, heat flux conducted decreases so that droplet lifetime increases. For high ambient pressures, the enthalpy of vaporization may be sufficiently reduced so that droplet lifetime slightly decreases.

For higher ambient temperatures, as pressure increases, droplet surface temperature increases. However, since difference between surface temperature and ambient temperature is important, heat flux to droplet surface is always efficient. Furthermore, as pressure increases, vaporization enthalpy reported in Fig. 7 shows a net decrease eventually dropping to zero when supercritical vaporization regime is reached. Then, it becomes obvious that, for high ambient temperatures, an increase in ambient pressure is followed by a decrease in droplet lifetime.

### 3 Correlations of Results

From observations of Figs. 1, 2, and 3 and previous discussion, it seems difficult to correlate droplet lifetime with pressure regardless of the ambient temperature. In the present section, we only consider ambient temperatures above  $750 \text{ K}$ . The basic idea is first to reduce the droplet lifetime based on the low pressure value ( $p = 1 \text{ atm}$ ), and then to correlate the reduced droplet lifetime by means of a function of ambient pressure. Computations have been carried out for different droplet initial temperatures, which are however different for the three hydrocarbon droplets due to the different normal

boiling temperatures of the three hydrocarbon species. Thus, for *n*-pentane droplets,  $T_0 = 275, 300\text{ K}$  have been considered. For *n*-heptane and *n*-decane droplets,  $T_0 = 300, 325,$  and  $350\text{ K}$  have been considered.

Let us first compare our numerical results obtained for low pressures with the predictions of the quasi-steady theory. This theory gives two expressions for droplet lifetime, respectively:

$$\tau = d_0^2 \frac{\rho_l}{8\pi} \frac{c_{ps}}{\lambda_s} [\ln(1 + B_T)]^{-1} \quad (2)$$

and

$$\tau = d_0^2 \frac{\rho_l}{8\pi} \frac{1}{\rho D_s} [\ln(1 + B_Y)]^{-1} \quad (3)$$

The two Spalding numbers involved are expressed by:

$$B_T = \frac{c_p(T_\infty - T_s)}{\Delta H} \quad \text{and} \quad B_Y = \frac{Y_{Fs}}{1 - Y_{Fs}} \quad (4)$$

By equating Eqs. (2) and (3), and using Raoult's law for linking interface equilibrium composition and temperature, an estimation of droplet lifetime may be obtained. The quasi-steady theory requires that the thermal diffusivity, molecular diffusion coefficient and specific heat are time and space-constant. These properties are estimated by means of an average between surface and ambient conditions. In Fig. 8, we have reported the ratio of numerical prediction to the corresponding theoretical value. The agreement is only weak, it only gives the order of magnitude. This disagreement may be explained by the simplifying hypotheses used in the quasi-steady theory: constant liquid temperature, space constant transport and thermodynamic properties, idealized thermodynamic equilibrium. As can be seen from Fig. 8, the departure from the quasi-steady theory is maximum for low ambient temperature, where the droplet heat-up process is expected to occupy a longer portion of the droplet lifetime. This heat-up process is not taken into account in the quasi-steady theory.

In Tables 2, 3, and 4, droplet lifetimes at low pressure conditions ( $p = 1\text{ atm}$ ) issued from our numerical simulations are reported. These tables may be used to extrapolate low pressure droplet lifetimes to other ambient or initial conditions.

Only a few relevant experimental data are available in the literature, although many experimental works have been carried out on droplet vaporization. In quiescent environment, we can mention the work performed by, for example, Faeth *et al.*<sup>2</sup>, Kadota and Hiroyasu<sup>4</sup>, and more recently, Hartfield<sup>3</sup> and Sato<sup>7</sup>. The work of Faeth *et al.* was only concerned by the combustion of binary-fuel droplets, whereas the work of Kadota and Hiroyasu, although applying to pure vaporization processes, was conducted under normal gravity conditions. Considering pure vaporization conditions leads to droplet lifetime of the order of 10 to 30 seconds for the droplet size handled experimentally. On the other hand, micro-gravity test facilities provide micro-gravity conditions for a much shorter amount of time. Nevertheless, Hartfield<sup>3</sup> and Sato<sup>7</sup> have conducted droplet vaporization experiments under micro-gravity conditions. Both used *n*-heptane

$T_{\infty}, K$	750	1000	1500	2000	2500
$T_0 = 275K$	41.1	30.8	21.8	17.6	15.1
$T_0 = 300K$	38.4	29.0	20.8	16.9	14.6

Table 2: Low pressure vaporization lifetime (ms); *n*-pentane/air system;  $p = 1 \text{ atm}$ .

$T_{\infty}, K$	750	1000	1500	2000	2500
$T_0 = 300K$	44.8	32.6	23.2	18.7	16.1
$T_0 = 325K$	42.2	31.3	22.2	18.0	15.5
$T_0 = 350K$	39.3	29.5	21.1	17.2	14.8

Table 3: Low pressure vaporization lifetime (ms); *n*-heptane/air system;  $p = 1 \text{ atm}$ .

droplets vaporizing in a nitrogen atmosphere. They used a suspended droplet technique which enable them to stabilize spatially the droplet. Comparisons of our numerical simulations to both experimental works only provide poor agreements. Numerical and experimental results only agree on the order of magnitude of the droplet lifetime. This does not question our numerical results however. First, both experimental works lead to different droplet lifetimes or vaporization constants, i.e. the slope in the later stage of the droplet lifetime of the square of the droplet diameter as a function of the time. Two sets of experimental results presented by Sato show some disagreements between each others of the order of a few tens of percents. First the experimental technique used by Hartfield leads to an over-shoot of the pressure and a non-zero convective velocity in the neighborhood of the droplet for a time comparable to the droplet lifetime. Second, for both experimental studies, some uncertainties remain in the value of the initial droplet temperature, which is strongly affected by the ambient temperature because of the droplet formation technique used. Moreover, since the droplet is hold by a fiber, this fiber tends to heat-up the interior of the droplet especially if the ambient temperature is high. This leads to significant difference between numerical predictions and experimental results. Thus, the best agreements between numerical predictions and experimental data are obtained for the low-temperature results presented by Sato<sup>7</sup>. In this case, the discrepancy between numerical predictions and experimental results is of the order of 30 %. It is however very important to mention that our numerical results

$T_{\infty}, K$	750	1000	1500	2000	2500
$T_0 = 300K$	51.1	36.3	25.1	20.1	17.2
$T_0 = 325K$	48.9	34.9	24.2	19.5	16.7
$T_0 = 350K$	46.5	33.5	23.4	18.9	16.2

Table 4: Low pressure vaporization lifetime (ms); *n*-decane/air system;  $p = 1 \text{ atm}$ .

present the same trend that the experimental results presented by Sato, in terms of the influence of both ambient pressure and temperature on the droplet lifetime.

Figure 9 presents reduced droplet lifetime,  $\tau_r = \tau/\tau_p = 1 \text{ atm}$ , as a function of the ambient pressure for each hydrocarbon. All the different ambient temperatures and initial droplet temperatures reported in the previous tables have been considered. Results collapse extraordinary well, so that reduced droplet lifetime may be expressed as a function of pressure:

$$\tau_r = \exp[-a(p - p_{ref})/p_{ref}] \quad (5)$$

with  $p_{ref} = 1 \text{ atm}$ . Values of  $a$ , average and maximum deviation are summarized in Table 5.

	$a$	average deviation	maximum deviation
<i>n</i> -pentane	0.140	0.9 %	11.3 %
<i>n</i> -heptane	0.084	0.6 %	5.7 %
<i>n</i> -decane	0.050	0.7 %	11.6 %

Table 5: Correlations of results.

## 4 Concluding Remarks

A comprehensive study concerning hydrocarbon droplets vaporizing in air has been carried out. Only pure *n*-heptane and pure *n*-decane droplets have been considered. The effect of pressure has been estimated and explained. Two different behaviors appear depending on ambient temperature. In the case where ambient temperature is

above 750 K, droplet lifetime may be correlated for various initial droplet temperature and ambient temperature. This correlation uses estimation of droplet lifetime at low pressure and a simple function of ambient pressure. For the presented computations, the average deviation between numerical results and the correlation is less than 2 %.

## References

- <sup>1</sup> Daou, J., Haldenwang, P., Nicoli, C. Supercritical Burning of Liquid (LOX) Droplet with Detailed Chemistry. *Combustion and Flame*, pages 153–169, 1995.
- <sup>2</sup> Faeth, G.M., Dominicus, D.P., Tulpinsky, J.F., Olson, D.R. Supercritical Bipropellant Droplet Combustion. *Twelfth Symposium (International) on Combustion*, The Combustion Institute, pages 9–18, 1968.
- <sup>3</sup> Hartfield, J.P., Farrel, P.V. Droplet Vaporization in a High Pressure Gas. *Journal of Heat Transfer*, 115:699–706, 1993.
- <sup>4</sup> Kadota, T., Hiroyasu, H. Evaporation of a Single Droplet at Elevated Pressures and Temperatures. *Bulletin of the JSME*, 19(138):1515–1521, 1976.
- <sup>5</sup> Lafon, P. Modélisation et Simulation Numérique de l'Evaporation et de la Combustion de Gouttes à Haute Pression. *Thèse de doctorat, Université d'Orléans*, 1994.
- <sup>6</sup> Lafon, P., Yang, V., Habiballah, M. Supercritical Vaporization of Liquid Oxygen in Hydrogen and Water Environments. *Submitted to Journal of Fluid Mechanics*, 1995.
- <sup>7</sup> Sato, J. Studies on Droplet Evaporation and Combustion in High Pressures. *AIAA Thirty-First Aerospace Sciences Meeting & Exhibit, Reno, NV*, 93-0813, 1993.
- <sup>8</sup> Shuen, J.S., Yang, V., Hsiao, C.C. Combustion of Liquid-Fuel Droplets in Supercritical Conditions. *Combustion and Flame*, 89:299–319, 1992.

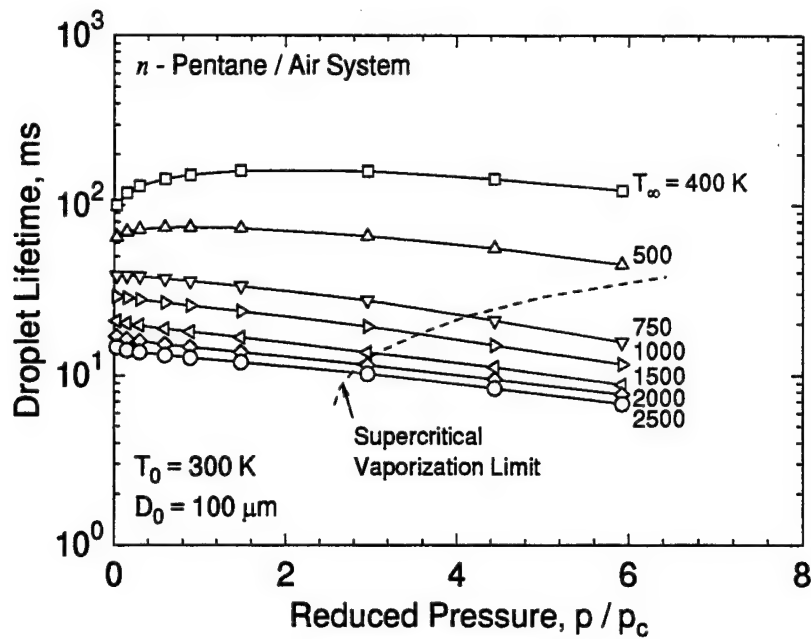


Figure 1: Droplet lifetime as a function of the reduced pressure for different ambient temperatures; *n*-pentane/air system,  $T_0 = 300 \text{ K}$ ;  $d_0 = 100 \mu\text{m}$ .

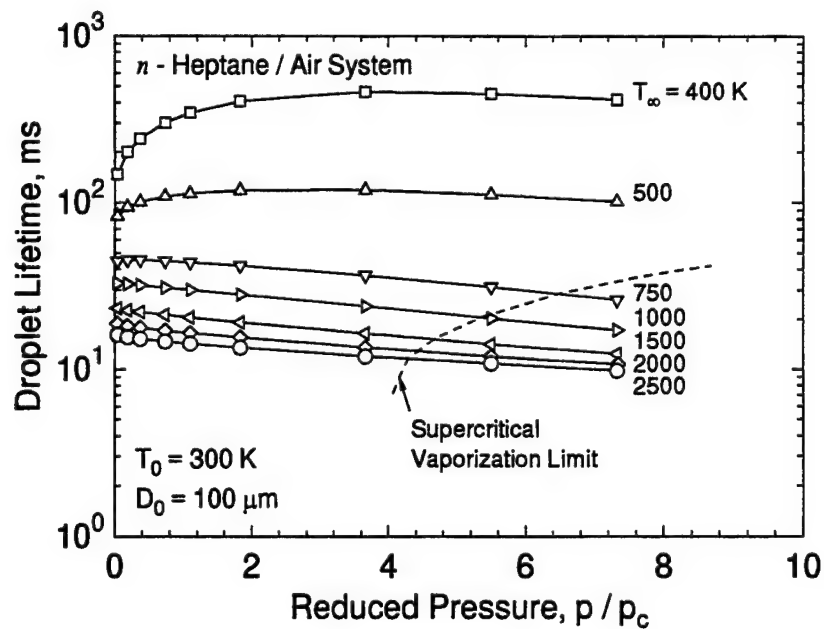


Figure 2: Droplet lifetime as a function of the reduced pressure for different ambient temperatures; *n*-heptane/air system,  $T_0 = 300 \text{ K}$ ;  $d_0 = 100 \mu\text{m}$ .



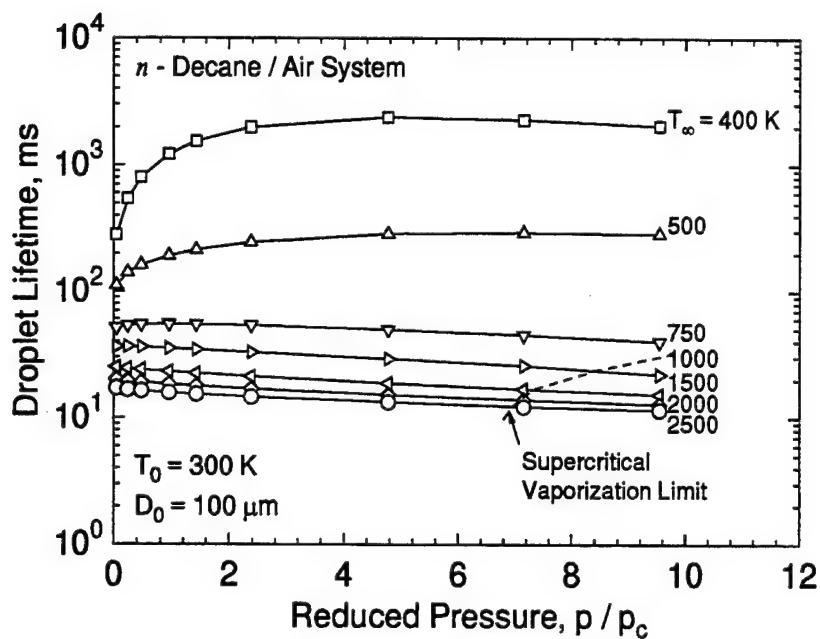


Figure 3: Droplet lifetime as a function of the reduced pressure for different ambient temperatures; *n*-decane/air system,  $T_0 = 300 \text{ K}$ ;  $d_0 = 100 \mu\text{m}$ .

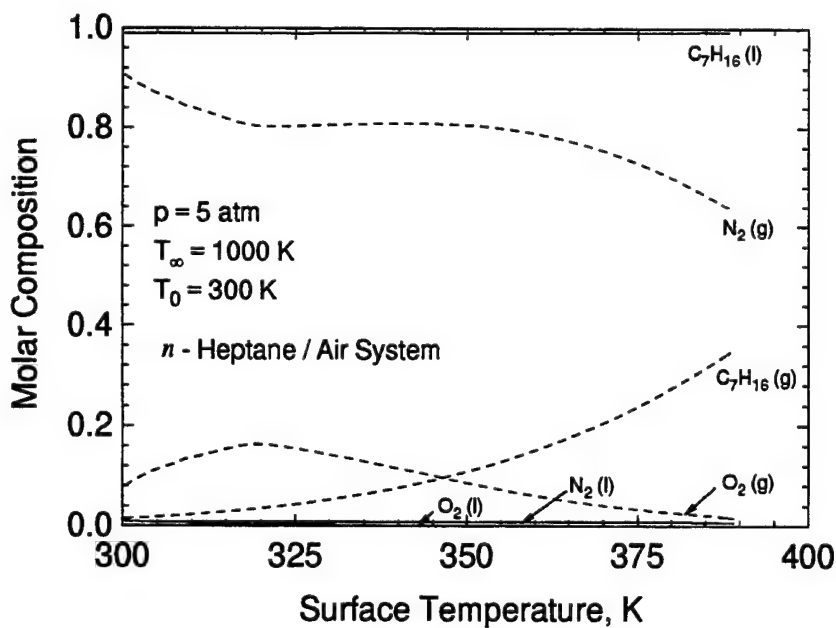


Figure 4: Equilibrium compositions as a function of temperature; *n*-heptane/air system;  $T_\infty = 1000 \text{ K}$ ,  $T_0 = 300 \text{ K}$ ,  $p = 5 \text{ atm}$ .

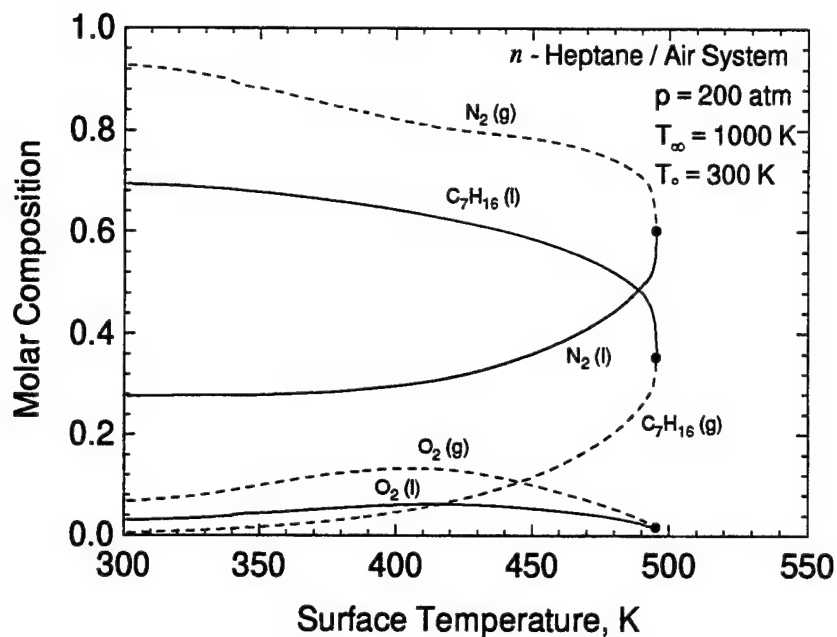


Figure 5: Equilibrium compositions as a function of temperature; *n*-heptane/air system;  $T_{\infty} = 1000 \text{ K}$ ,  $T_0 = 300 \text{ K}$ ,  $p = 200 \text{ atm}$ .

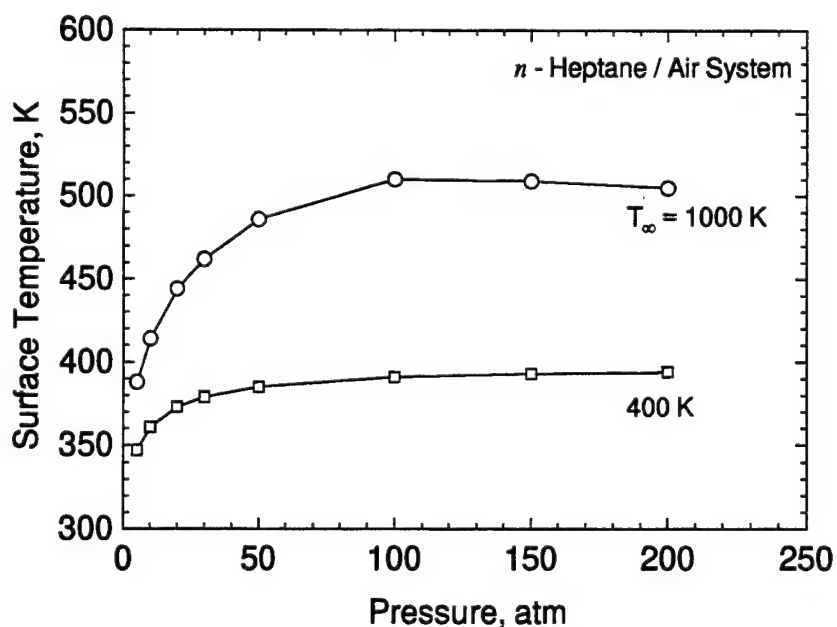


Figure 6: Final surface temperature function of ambient pressure; *n*-heptane/air system;  $T_0 = 300$ .

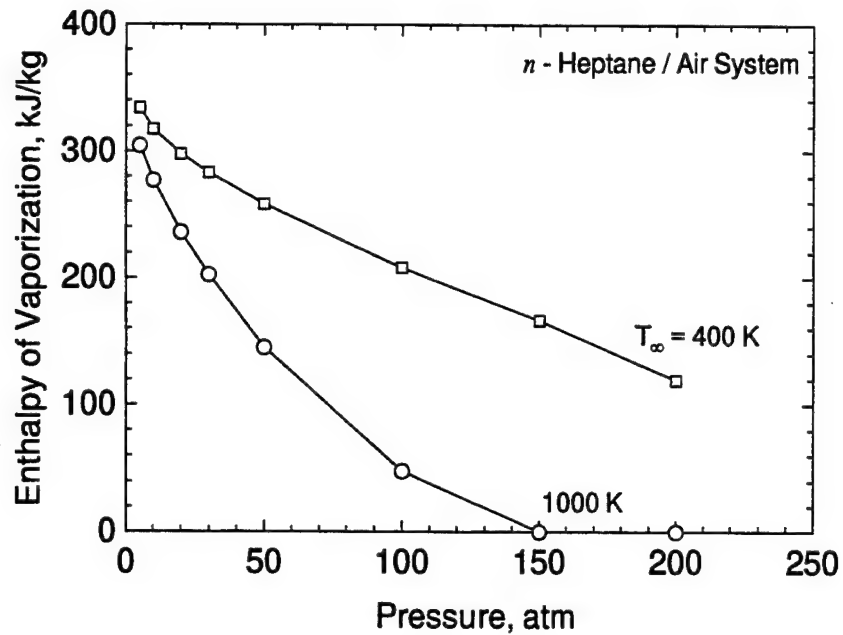


Figure 7: Final mixture vaporization enthalpy function of ambient pressure; *n*-heptane/air system;  $T_0 = 300$  .

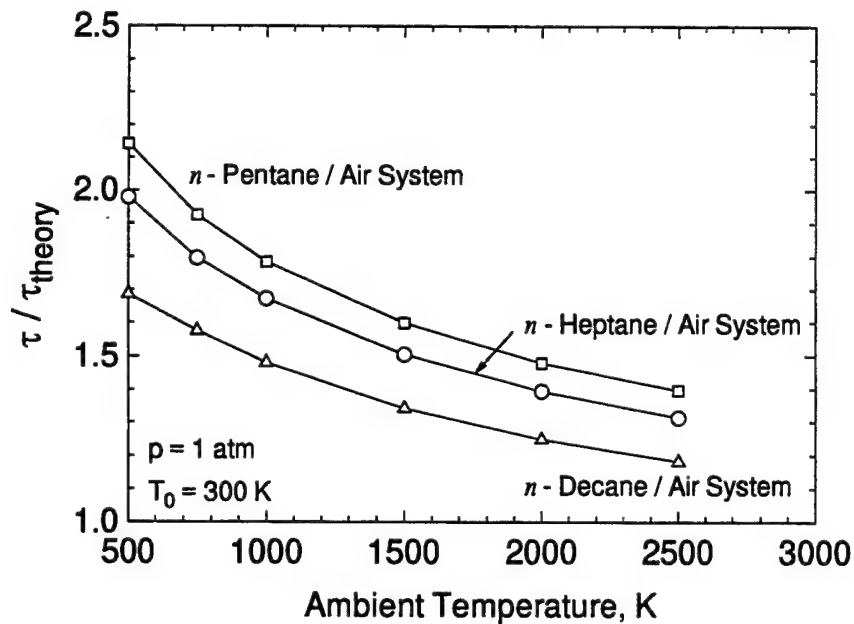


Figure 8: Comparison of numerical results with theoretical predictions for low ambient pressure;  $T_0 = 300$  .

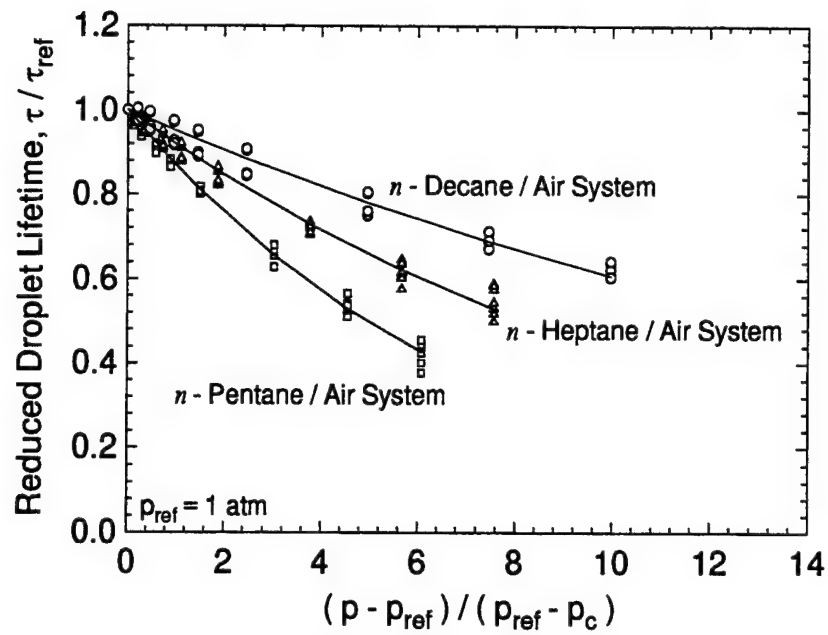


Figure 9: Reduced droplet lifetime function of ambient pressure.

# **Droplet Vaporization at Thermodynamic Non-Equilibrium Conditions**

Patrick Lafon and Vigor Yang  
The Pennsylvania State University  
Department of Mechanical Engineering

## **Abstract**

The purpose of this study is to estimate the influences of thermodynamic non-equilibrium conditions on droplet vaporization processes. The study focuses on the oxygen/hydrogen system, and is conducted in two steps. First, a droplet vaporization model based on the thermodynamic equilibrium assumption is used; its predictions of the vaporized mass flow rate are compared with the molecular fluxes issued from molecular dynamics theory. Except for small droplet diameters, molecular dynamics does not appear to be a limiting factor to the achievement of thermodynamic equilibrium. However, since some uncertainties remains in the expression of the molecular fluxes, it may be interested to compute the features of the superheated liquid phase resulting from non-equilibrium conditions. This is the purpose of the second part of this study. Thus, the limit of existence of the metastable liquid phase are estimated, i.e. the thermodynamic stability limit (spinodal limit) and the kinetic limit. The latter limit involves the determination of the homogeneous nucleation rate. For both limit conditions of superheated liquid, the change in terms of enthalpy of vaporization with respect to the thermodynamic-equilibrium model are estimated giving some insights on the influence of the non-equilibrium conditions on the droplet vaporization pro-

cesses.

## 1 Introduction

During the last decades, many work were devoted to the understanding of the droplet vaporization process under high pressure conditions. Highly sophisticated numerical models were developed in order to simulate the process. The need of numerical models was due to the unsteady features of the overall process, to the importance of the space and time variations of the transport properties, as long as to the importance of the dissolution phenomenon as pressure increases. Taking into account this dissolution phenomenon necessitates the use of a real-gas thermodynamic modelization. However, in all the former studies, the hypothesis of thermodynamic equilibrium at the droplet interface is assumed. Thus, it is postulated that the molecular transfers are fast enough to ensure that thermodynamic equilibrium is reached. In other words, molecular dynamic is not a limiting factor in the achievement of thermodynamic equilibrium. The justification lies implicitly in the fact that the characteristic time of completion of the equilibrium is short, at least by several orders of magnitude, compared with the characteristic diffusion times ruling droplet vaporization.

The aim of this work is to possibly provide a justification to this assumption, or to estimate the consequences of any departure from the equilibrium conditions. The work is focused on the system oxygen hydrogen, but the same developments may be carried out for hydrocarbon air systems and, at least, some of the conclusions may be used. Therefore, we proceed in two steps. First, we determine whether or not the thermodynamical equilibrium can be reached on a molecular viewpoint, by looking closely at the molecular transfers at the interface. Since some of the parameters used

in the estimation of the molecular fluxes are only roughly known, as we will discuss later on, this first analysis does not enable us to conclude definitely on this problem. It appears thus necessary to conduct a further study.

The aim of this second study is to estimate what the limits of non-equilibrium conditions are both on a thermodynamic stability and kinetic outlooks. Here, our only concern is the limit of superheat for the liquid phase. The thermodynamic stability limit or spinodal limit involves the stability of the liquid metastable phase, and is fully determined by means of the thermodynamic modelization. The kinetic limit of superheat involves both molecular dynamics theory and thermodynamic modelization through computation of the nucleation rate. Although the molecular fluxes are subject to the same limitations as previously, their influence on the estimation of the nucleation rate is small compared to the one of the thermodynamic modelization, so that a good confidence can be obtained for the issued predictions.

The changes in the conditions seen by the interface are then estimated for these two limit conditions, spinodal and kinetic limit, respectively. The influence of non-equilibrium conditions of the vaporized mass flow rate and thus on the droplet lifetime is determined.

## 2 Molecular Fluxes at the Interface

If the interface between two phases is studied at the molecular level, it appears no longer as an abrupt discontinuity, but it is rather the locus of a smooth transition between the two phases. This feature is presented in Fig. 1. Since this transition occurs within a few molecular mean free paths, or intermolecular distance, on a macroscopic viewpoint the interface is still best modeled by a discontinuity between the two bulk phases. Our

concern here is to estimate the flux of molecules crossing the interface going from one bulk phase to an other, in one or the other way, i.e. condensation or vaporization flux. The net flux of vaporization is then the difference between the two fluxes. If Boltzmann's statistics applies, it can be shown that the molecular rate of species  $i$  per unit area for a fixed-location interface may be expressed by<sup>1</sup>

$$j_{N_i} = \frac{1}{4} \left( \frac{N_i}{V} \right) \left( \frac{8k_B T}{\pi m_i} \right)^{1/2} \quad (1)$$

where  $T$ ,  $k_B$ ,  $N_i$ ,  $m_i$  are the temperature, the Boltzmann's constant, the number density of species  $i$ , and the mass of molecule  $i$ , respectively. After rearrangements, this leads to an equivalent expression for  $j_{N_i}$

$$j_{N_i} = \frac{\rho X_i}{W} \left( \frac{R_u T}{2\pi W_i} \right)^{1/2} \mathcal{N}_A^{-1} \quad (2)$$

where  $\mathcal{N}_A$ ,  $\rho$ ,  $R_u$ ,  $X_i$  are the Avogadro number, the density of the mixture, the universal gas constant, and the molar fraction of species  $i$  in the mixture, respectively. This expression does not involve in its current formulation any assumption concerning the behavior of the gas, i.e. the ideal-gas assumption is not used. Nevertheless, when considering a droplet vaporization model, one must consider the interface regression velocity. Schrage<sup>10</sup> has shown that the previous expressions have to be corrected by a factor  $\Gamma$  function of the ratio  $v_s/\sqrt{2R_u T/W}$ . This correction factor is significant only when  $v_s/\sqrt{2R_u T/W} > 0.01$ . For the oxygen/hydrogen system, the correction factor will only be significant for surface regression velocities over 10 m/s. Thus, it can be neglected in a first approximation.

Concerning the validity of expression 1, two major restrictions have to be made. First, the expression of  $j_{N_i}$  is obtained from integration of the velocity distribution function under the assumption that the molecules do not experience any collision. For



a dense fluid, this assumption is certainly not valid, but one could argue that the number of molecules initially travelling on one way and which will be reflected in the other direction is roughly balanced by the number of molecules initially travelling on the opposite way and which experience also a collision. Second, for similar reasons, if the expression of  $j_{N_i}$  is to be used to estimate the phase-change rate, it has to be corrected by a so-called accommodation coefficient which takes into account the fact that only a portion of the molecules striking the interface is actually due to condensation or vaporization. The remaining fraction is due to reflection of molecules. The value of the accommodation coefficient depends on the local interface conditions and therefore depends on the system involved. Values of the accommodation coefficient between 0.5 and 1 have been reported in the literature.<sup>1</sup> When experiments show that the accommodation coefficient exhibits values very different from unity, it is most likely that the molecular dynamics theory used does not apply for the system considered.

A way to assess the validity of the thermodynamic-equilibrium assumption is to compare the respective orders of magnitude of the net vaporization mass flow rate under equilibrium conditions, and the mass flow rates, vaporization and condensation, issued from molecular dynamics theory. To overcome the difficulty related to the uncertainty associated with the accommodation coefficient, we only consider the following ratios

$$\frac{(m_i j_{N_i} A_s)^l}{\dot{m}_{i,eq}} \quad \frac{(m_i j_{N_i} A_s)^g}{\dot{m}_{i,eq}} \quad (3)$$

where  $A_s$ ,  $m_i$ ,  $\dot{m}_{i,eq}$  represent the area of the interface, the mass of molecule  $i$ , and the equilibrium net vaporization mass flow rate, respectively.  $(m_i j_{N_i} A_s)^l$  and  $(m_i j_{N_i} A_s)^g$  represent the mass flow rate across the interface coming from the bulk liquid phase, i.e. vaporization mass flow rate, and the mass flow rate across the interface coming from the bulk gaseous phase, respectively. The estimations of the vaporization mass flow rate

under thermodynamic-equilibrium conditions are obtained from numerical simulations issued from a one-dimensional model. The model and the theoretical formulation used have been presented by the authors in a previous paper.<sup>6</sup> The model has been applied successfully to the simulation of oxygen droplet vaporization in hydrogen atmospheres under a broad range of ambient pressure conditions.

From Eq. (2), we see that molecular fluxes are fully determined by the bulk phase temperature, density and composition. In Fig. 2, the decimal logarithm of the ratios of Eq. (3) are reported throughout the droplet lifetime for the two species involved in this particular system. The ambient pressure, the ambient temperature, and the initial droplet diameter are equal to 30 atm, 1000 K, and 100  $\mu m$ , respectively. The divergence exhibited by the two curves concerning hydrogen rates comes from the sign change of hydrogen mass flow rate. The hydrogen starts to condensate and aggregates within the liquid droplet, after a while, the trends is reversed and the hydrogen vaporizes. However, for hydrogen, the predictions of mass flow rate from molecular dynamics theory are by several orders of magnitude bigger than the hydrogen equilibrium mass flow rate. Despite the uncertainty in the accommodation coefficient, this demonstrates that hydrogen transfer at the interface is by no means a limiting factor in the achievement of the thermodynamic equilibrium.

For the case reported in Fig. 2, the molecular dynamics gives estimations of the oxygen mass flow rate, condensation or vaporization, by slightly more than 3 orders of magnitude bigger than the net vaporization mass flow rate obtained under thermodynamic-equilibrium conditions. The smaller of the two ratios is the one concerning oxygen flux from the gaseous phase towards the liquid phase, i.e. the condensation mass flow rate. This features is essentially due to the change in density between liquid and gaseous

phase.

For subcritical regimes of vaporization, i.e. when thermodynamic equilibrium exists throughout the droplet lifetime, the droplet vaporization process is almost quasi-steady except at the beginning of the process. In this case, the famous  $d^2$ -law holds, the droplet surface regression is linear with time and it can be shown that the mass flow rate is proportional to the droplet diameter. If this quasi-steady regime, the surface temperature reaches a constant value after the heat-up period, so does the interface composition. Thus, the molecular dynamics mass flow rate is proportional to the instantaneous droplet diameter. Furthermore, in this pure vaporization case, there is only one length scale involved in the overall process.<sup>2</sup> A dimensional analysis shows that all characteristic times are related to the squared initial droplet diameter. Thus, the droplet behavior throughout its lifetime may be related to its initial diameter. From the previous remarks, we see that the order of magnitude of the ratios defined in Eq. (3) will be reduced by 1 as the initial droplet diameter is divided by 10. Thus, for the same temperature and pressure conditions as the ones reported in Fig. 2, the difference in order of magnitude will drop to 2 for an initial droplet diameter of  $10\ \mu\text{m}$ . Thus, for small droplet, the thermodynamic equilibrium assumption becomes questionable.

In Figs. 3 and 4, the influence of ambient pressure and ambient temperature is analyzed. In those plots, only the minimum of the two ratios defined in Eq. (3) for oxygen are reported. The ambient pressure ranges from  $10\ \text{atm}$  to  $50\ \text{atm}$ , and the ambient temperature from  $1000\ \text{K}$  to  $2500\ \text{K}$ . The order of magnitude of the ratio between the two mass flow rates is only slightly affected by the change in ambient conditions. The estimations of the mass flow rate issued from the molecular dynamics theory are sensitive to the ambient pressure by the change induced in the density, in ad-

dition, when the pressure varies, the equilibrium compositions and temperature of the interface are affected. On the other hand, a change in pressure does not affect considerably the value of the equilibrium net vaporization rate. Since, as pressure increases, the partial density of oxygen on the gaseous phase of the interface increases also, the thermodynamic equilibrium becomes more and more valid as pressure increases. The ambient temperature has only a small influence upon the interface conditions. However, its influence is more significant on the droplet lifetime and therefore on the equilibrium net vaporization mass flow rate, which increases significantly as ambient temperature increases. This explains why the order of magnitude of the ratio of the two mass flow rates drops slightly with increasing ambient temperatures.

As a conclusion to this first part, after estimating the efficiency of the molecular transfer at the interface, the thermodynamic equilibrium assumption is valid for oxygen droplets vaporizing in hydrogen atmospheres as long as the droplet initial diameter is above a threshold value close to  $10\text{ }\mu\text{m}$ . Usually the oxygen droplet diameter atomized in rocket engines combustion chamber are close to  $100\text{ }\mu\text{m}$ . Small droplets, such as the ones mentioned previously, are obtained when 99.9 % of the droplet mass have vaporized, and such small droplets are usually neglected. The achievement of thermodynamic equilibrium depends on the ambient conditions of temperature and pressure, also this sensitivity is less significant than the sensitivity to the droplet diameter. In this first part, we have considered that thermodynamic equilibrium assumption for droplet vaporization modelization holds as long as the molecular transfer is by 2 or 3 orders of magnitude bigger than the actual transfer required under equilibrium conditions. Despite our efforts, some uncertainties still remain for the estimation of the molecular dynamics fluxes. First, there is the uncertainty in the validity in the chosen statistics,

i.e. Boltzmann's statistics versus Fermi or Dirac's statistics. Second, there is the uncertainty in the order of magnitude of the accommodation coefficient. It is believed although not proven that this will not affect the previous conclusions. Nevertheless, it might be interesting to estimate what will be the effects on the surface conditions, in terms of compositions and enthalpy of vaporization, under non-equilibrium conditions. This will be the aim of the next section.

### 3 Limits of Superheat

Let us discuss an interesting and necessary matter about thermodynamic phase transitions and phase stability. In most of physical cases, phase changes do not occur under thermodynamic equilibrium conditions, <sup>i.e.</sup> Whether the liquid is superheated or the vapor is supercooled. For <sup>a</sup> single-component mixture, the liquid phase is superheated when, <sup>at</sup> for a given pressure, its temperature is above <sup>the</sup> ~~its~~ saturation value, and vice versa for supercooled vapor. Such phases are called metastable phases. The state of a system, with given values of the total entropy  $S$ , of the number of molecules  $N$ , and of the volume  $V$ , satisfies the relation

$$\delta U = 0 \quad (4)$$

where  $U$  represents the total internal energy of the system. This state is stable if and only if it is located on a local minimum of the phase space. From basic thermodynamic relations, it can be shown that a stable thermodynamic state satisfies several stability criteria.<sup>1</sup> For a single-component mixture, the first criterion is called the criterion of thermal stability and requires that

$$C_v > 0 \quad (5)$$

This criterion is virtually never violated, and the second stability criterion for a single-component mixture, called the criterion of mechanical stability becomes a necessary and sufficient condition, it requires that

$$\left(\frac{\partial p}{\partial \rho}\right)_T > 0 \quad (6)$$

For a binary mixture, like the one we are interested in, an extra criterion of stability must be satisfied, it is called the criterion of material stability or criterion of diffusional stability. The former terminology is preferable since no diffusion processes are involved. It is expressed as follows

$$\left(\frac{\partial \mu_1}{\partial X_1}\right)_{T,P} > 0 \quad (7)$$

This relation may be transformed by using derivatives of the chemical potential with respect to the number of moles of both species

$$\left(\frac{\partial \mu_1}{\partial X_1}\right)_{T,P} = n \left[ \left(\frac{\partial \mu_1}{\partial n_1}\right)_{n_2,P,T} - \left(\frac{\partial \mu_1}{\partial n_2}\right)_{n_1,P,T} \right] \quad (8)$$

where  $n$  represents the total number of moles of the system. These latter derivatives possess interesting properties of symmetry with respect to species 1 and 2, due to the second Gibbs-Duhem equation applied to the Gibbs free energy. It is interesting to tell that the criterion of Eq. (7) is satisfied or violated simultaneously for both species. As for a single-component mixture the criterion of mechanical stability was violated before the criterion of thermal stability, for a binary mixture, the criterion of material stability is the first to be violated.

When the system crosses this limit of thermodynamic stability, it experiences a sudden phase transition, i.e. the superheated liquid becomes suddenly vapor. This thermodynamic limit of superheat is called the spinodal limit. On a molecular level, the sudden phase change is due to internal fluctuations within the liquid which are no

longer compatible with the existence of a liquid phase. Such fluctuations are called heterophase fluctuations.

There is a second limit to the existence of metastable phases which is called the kinetic limit, since it involves molecular dynamics. The heterophase fluctuations, which have been reported before, occurs not only at the spinodal limit but also all over the stable phase and metastable phase domain. Those heterophase fluctuations are characterized by some local molecular density fluctuations. Let us concentrate our attention on the case of a superheated liquid, which is <sup>of</sup> special interest for us. For this case, heterophase fluctuations will tend to create bubbles within the metastable liquid phase. By computing the Gibbs free energy of the nucleus bubble, it can be shown that these nuclei are either stable or unstable depending on their size and thus on their number of molecules. There exists a critical nucleus which is located on a local extremum of the Gibbs energy function. When a critical nucleus gains one <sup>extra</sup> molecule, it will tend to grow indefinitely, whereas when it loses one molecule, it will tend to decay. The homogeneous nucleation rate is the rate of creation of nucleus of the critical size. At the saturation conditions, the homogeneous nucleation rate is zero, essentially ~~becomes~~ the radius of the critical nucleus is infinite. But, as the level of superheat is increased, this homogeneous nucleation rate will switch progressively from extremely low values to extremely high value. Eventually, its value will be high enough to physically observe an instantaneous phase transition. Usually, a threshold value of  $10^{12} \text{ cm}^{-3} \text{ s}^{-1}$  is arbitrarily chosen to constitute the kinetic limit of superheat. Let us now introduce the theoretical basis associated with the computation of the homogeneous nucleation rate for binary systems.

The index 1 and 2 denotes quantities with respect to oxygen, and hydrogen, respec-

tively. The homogeneous nucleation rate is expressed in the following form

$$J = K \cdot e^{-\Delta G^*/k_B T} \quad (9)$$

where  $K$  is a kinetic factor, and  $\Delta G^*$  is the Gibbs free energy of the critical nucleus. The Gibbs free energy of a nucleus  $\Delta G(N_1^b, N_2^b)$  is a function of the number of molecules of both species within the nucleus bubble. The  $\Delta G(N_1^b, N_2^b)$  plane exhibits a saddle point, which position corresponds to the position of the critical nucleus. It corresponds to the lowest passage over an energy barrier for the nucleus to reach a size above which it will grow to a macroscopic <sup>or bubble?</sup> droplet. The central assumption of the classical nucleation theory is the Gibbs' capillarity assumption which states that the bubble can be described by using classical thermodynamic. The expression of the Gibbs free energy is given by a sum of a bulk plus a surface contribution

$$\Delta G(N_1^b, N_2^b) = \sum_{i=1,2} n_i^{bb} \mu_i^{bb} + \sum_{i=1,2} n_i^{sb} \mu_i^{sb} - \sum_{i=1,2} n_i^b \mu_i^l + 4\pi R^2 \sigma \quad (10)$$

where  $n_i^b$ ,  $n_i^{bb}$ , and  $n_i^{sb}$ , represent the number of moles of species  $i$  in the total bubble, in the bulk volume of the bubble, and in the surface of the bubble, respectively. These mole numbers may be related to the molecule numbers by means of the Avogadro number.  $\sigma$  represents the surface tension of the bubble. In this expression, a distinction has been made between the molecules of the bubble on the surface and in the bulk volume of the bubble. However, the surface of the bubble is assumed to be in equilibrium with the bulk volume

$$\mu_i^{sb} = \mu_i^{bb} \quad (11)$$

so that the Eq. (10) may be simplified to

$$\Delta G(N_1^b, N_2^b) = \sum_{i=1,2} N_i^b (\mu_i^b - \mu_i^l) + 4\pi R^2 \sigma \quad (12)$$



Furthermore, by using the Gibbs-Duhem equation for the bulk bubble molecules

$$\sum_{i=1,2} n_i^{bb} d\mu_i^{bb} = 0 \quad (13)$$

and the for the surface bubble molecules

$$\sum_{i=1,2} n_i^{sb} d\mu_i^{sb} + 4\pi R^{b^2} d\sigma = 0 \quad (14)$$

it can be shown that the system characterizing the location of the saddle point of the nucleus Gibbs free energy

$$\left( \frac{\partial \Delta G}{\partial N_1^b} \right)_{N_2^b, T, P} = 0 \quad (15)$$

$$\left( \frac{\partial \Delta G}{\partial N_2^b} \right)_{N_1^b, T, P} = 0 \quad (16)$$

may be simplified to give the so-called Kelvin equations

$$(\mu_1^b - \mu_1^l) + \frac{2\sigma \bar{v}_1^b}{R^b} = 0 \quad (17)$$

$$(\mu_2^b - \mu_2^l) + \frac{2\sigma \bar{v}_2^b}{R^b} = 0 \quad (18)$$

where  $\bar{v}_i$  represents the partial volume of species  $i$ , defined as

$$\bar{v}_i = \left( \frac{\partial v}{\partial n_i} \right)_{n_{j \neq i}, P, T} \quad (19)$$

which satisfies the following relation

$$v = \sum_i n_i \bar{v}_i = \frac{4}{3} \pi R^{b^3} \quad (20)$$

One important remark must be done concerning the expressions of Eqs. (17) and (18). The bubble chemical potentials  $\mu_1^b$  and  $\mu_2^b$  involved concern whether the surface of the bubble or the bulk volume of the bubble. In the latter case, they can be computed from the characteristics of the bulk volume of the bubble, i.e. temperature, pressure,

and composition. On the other hand, the partial molar volumes  $\bar{v}_1^b$  and  $\bar{v}_2^b$  are related to the composition of the whole bubble, surface plus bulk volume. They represent the increase of the volume due to an increase of one in the bubble of the number of moles 1 and 2, respectively. From the bulk volume composition and classical thermodynamic modelization, an estimation of the partial molar volume for the bulk volume of the bubble  $\bar{v}_i^{bb}$  may be obtained. Although only the molecules of the bulk volume of the bubble contribute to the volume of the bubble,  $\bar{v}_i^{bb}$  and  $\bar{v}_i^b$  are not equal but follow

$$\bar{v}_i^b = \bar{v}_i^{bb} \left( \frac{\partial N_i^b}{\partial N_i^{bb}} \right) \quad (21)$$

Since, we do not have more details about the molecule repartition between the surface and the bulk volume,  $\bar{v}_i^b$  cannot be obtained. However, as the size of the nucleus increases, it can be shown easily that the part of the molecules forming the surface becomes negligible with respect to the total number of molecules within the bubble, so that from relation 21,  $\bar{v}_i^b$  and  $\bar{v}_i^{bb}$  become equal. This assumption, although only valid for large nuclei, will be done in the remaining of this study. From this assumption, and use of Eqs. (12), (17), and (18), the Gibbs free energy of the critical nucleus may be simply expressed as follows

$$\Delta G^* = \frac{4}{3} \pi R^{b2} \sigma \quad (22)$$

In addition, the critical nucleus is in mechanical equilibrium with the surrounding liquid, so that the Laplace's equation holds

$$p^b - p^l = \frac{2\sigma}{R^b} \quad (23)$$

and in thermal equilibrium with the surrounding liquid

$$T^b = T^l \quad (24)$$

① oxygen  
② hydrogen

For a binary mixture, the saturation ratio is classically defined as the ratio of the molar fraction of species 2 in the liquid phase with respect to the one under saturation conditions

$$S = \frac{X_2^l}{X_{2,sat}^l} \quad (25)$$

For a given liquid pressure, liquid temperature, and saturation ratio, the features of the critical nucleus, i.e. numbers of molecules, radius, pressure, and temperature, are fully determined by solving simultaneously Eqs. (17), (18), (23), and (24).

To compute the Gibbs free energy of the critical nucleus, given that the Gibbs' capillarity applies, one needs a thermodynamic modelization in order to calculate the thermodynamic quantities needed. In the previous studies concerning droplet vaporization at high pressure, which we have carried out,<sup>5,6</sup> the Soave-Redlich-Kwong equation of state has been used. Predictions of the liquid density are close to 10 % of the experimental. However, the use of such a simple equation of state was necessary due to the need to calculate analytically first and second derivatives of primary thermodynamic variables such as Gibbs free energy. In the present study, we face the same constraints. In addition, it is better to be consistent with previous studies. Thus, the thermodynamic modelization is based on the Soave-Redlich-Kwong equation of state. We make the assumption that such an equation of state is able to predict the thermodynamic behavior of a metastable phase. Looijmans *et al.*<sup>7</sup> have conducted the same kind of analysis using Soave-Redlich-Kwong equation of state, although it was for alkanes. When expressing the pressure in terms of temperature and density, it takes the form<sup>3</sup>

$$p = \frac{\rho R_u T}{(W - b\rho)} + \frac{a\alpha}{W} \frac{\rho^2}{(W + b\rho)} \quad (26)$$

where  $a$  and  $b$  accounts for attractive forces and repulsive forces between molecules,

respectively. Mixing rules to compute  $a$  and  $b$  are based on corresponding state principle

$$a\alpha = \sum_i^N \sum_j^N X_i X_j (1 - k_{ij}) \sqrt{a_i a_j \alpha_i \alpha_j}, \quad b = \sum_i^N X_i b_i \quad (27)$$

where  $a_i$ ,  $b_i$  and  $\alpha_i(T)$  are related to the critical properties and acentric factor of constituent species as follows

$$a_i = \frac{0.42748 R_u^2 T_{ci}^2}{P_{ci}}, \quad b_i = \frac{0.08664 R_u T_{ci}}{P_{ci}}, \quad (28)$$

$$\alpha_i(T) = \left[ 1 + f\omega_i \left( 1 - \sqrt{T/T_{ci}} \right) \right]^2 \quad \text{with} \quad f\omega_i = 0.48 + 1.574\omega_i - 0.176\omega_i^2$$

All the thermodynamic properties required in the analysis come from derivation of Eq.(26) and (27). Some details can be found in previous publications.<sup>5,6</sup>

Finally, in order to be able to compute the Gibbs free energy of the critical nucleus, we need an estimation of the surface tension of the critical bubble. On one hand its estimation is crucial is the final accuracy of the Gibbs free energy, the pressure difference between the bubble and its surrounding, and thus on the nucleation rate, on the other hand not many data exist in the literature. This is particularly true for the oxygen/hydrogen system. The surface tension of a mixture may be estimated by means of the Macleod-Sugden correlation,<sup>8</sup> it is expressed by

$$\sigma^{1/4} = \sum_i (P_i) \left[ (\rho X_i / W)^l - (\rho X_i / W)^g \right] \quad (29)$$

with  $\rho$ ,  $W$  and  $\sigma$  in  $g/cm^3$ ,  $g/mol$  and  $dyn/cm$ . The parameter  $P_i$  are the so-called parachors of the components. Even though it was originally suggested to compute them from molecular structure, best agreement is obtained by fitting experimental results. For instance, for oxygen, an experimental expression of the surface tension gives<sup>4</sup>

$$\sigma = \sigma_0 \left( 1 - \frac{T}{T_c} \right)^p \quad (30)$$

with  $\sigma^0$ , and  $p$  equal to 3.95 *dyn/cm*, and 1.255 respectively, which gives an evaluation of the parachor around 30.0. For hydrogen, such experimental correlation just does not exist. In order to obtain an estimation of the parachor for hydrogen, we proceed with the following procedure. We estimate the surface tension of pure hydrogen by means of a theoretical expression based on the corresponding state principle et supposedly valid for polar liquids.<sup>8</sup> The expression introduces the Stiel polar factor  $X$  and presents the following shape

$$\sigma = P_c^{2/3} T_c^{1/3} Q_p \left( \frac{1 - T_r}{0.4} \right)^m \quad (31)$$

with  $\sigma$ ,  $P_c$ ,  $T_c$ , and  $\omega$  being the surface tension in *dyn/cm*, the critical pressure in *bar*, the critical temperature in *K*, and the acentric factor, respectively.  $Q_p$ ,  $m$ , and  $X$  have respectively the following expressions

$$Q_p = 0.1560 + 0.365 \omega - 1.754 X - 13.57 X^2 - 0.506 \omega^2 + 1.287 \omega X \quad (32)$$

$$m = 1.210 + 0.5385 \omega - 14.61 X - 32.07 X^2 - 1.656 \omega^2 + 22.03 \omega X \quad (33)$$

$$X = \log [P_{vp}(0.6 T_c) / P_c] + 1.70 \omega + 1.552 \quad (34)$$

This enables us to obtain a value of the parachor for hydrogen close to 68.0. Eventually, we are now able to get an estimation of the Gibbs free energy of the critical nucleus bubble.

Figure 6 presents the contour levels of the nucleus bubble Gibbs free energy  $\Delta G$ , reduced by  $k_B T$ , as a function of  $N_1^b$  and  $N_2^b$ , i.e., the number of molecules in the nucleus bubble of oxygen and hydrogen, respectively. The liquid temperature, liquid pressure, and saturation ratio are equal to 110 *K*, 30 *atm*, and 5, respectively. The saddle point position has been determined by solving the system presented previously. However, for the plot of Fig. 6, an approximate method has been used to compute the Gibbs free energy of the nucleus. For a given bubble, the repartition of the molecules

between the surface and the bulk volume is unknown, partly because we do not know how to model the thermodynamic behavior of the surface molecules. Thus, the bulk volume composition of the bubble, and the expression of Eq. (10), even for a given number of molecules within the nucleus, cannot be obtained. Nevertheless, the shape of the Gibbs free energy can be obtained in the vicinity of the critical nucleus.<sup>7,12</sup> The bulk volume composition is assumed to be equal to the total bubble composition, the surface tension and the pressure inside the bubble are kept constant at the value of the critical nucleus. Thus, though the nuclei do not satisfy the Laplace's equation, the Gibbs free energy derivatives with respect to the molecule number of each of the two species are equal to the left-hand side of the Kelvin's equation reported in Eqs. (17) and (18).

In Fig. 6, the saddle point is located very close to the  $N_2^b$  axis, which indicates that the critical nucleus bubble is composed mainly of hydrogen. For the saturated conditions considered, the critical bubble is composed of 17 molecules of oxygen and 110 molecules of hydrogen, corresponding to a nucleus radius of  $9.5 \cdot 10^{-10} m$ .

To compute the nucleation rate, one must determine the expression of the kinetic factor  $K$  in Eq. (9). Developments were first carried out by Reiss<sup>9</sup> and refined by Stauffer,<sup>11</sup> and reported by Zeng.<sup>13</sup> An expression of  $K$  is obtained

$$K = \mathcal{N}_A \frac{\rho}{W} A B Z \quad (35)$$

$A$  is the surface area of the critical nucleus bubble,  $B$  is the average growth rate, which is given by

$$B = \frac{j_{N_1} j_{N_2}}{j_{N_1} \sin^2 \phi + j_{N_2} \cos^2 \phi} \quad (36)$$

and  $j_{N_i}$  given by Eq. (1).  $Z$  is the generalized Zel'dovich factor given by the following

equations

$$Z = -\frac{D_{11} \cos^2 \phi + 2 D_{12} \cos \phi \sin \phi + D_{22} \sin^2 \phi}{(D_{12}^2 - D_{11} D_{22})^{1/2}} \quad (37)$$

with

$$D_{ij} = \frac{1}{2} \left( \frac{\partial^2 \Delta G}{\partial N_i^b \partial N_j^b} \right)_{T,P} \quad (38)$$

$\phi$  is the angle between the  $N_1^b$  axis and the direction of growth of the critical nucleus bubble, its expression is

$$\tan \phi = s + \left( s^2 + \frac{j_{N_1}}{j_{N_2}} \right)^{1/2} \quad (39)$$

where

$$s = \frac{D_{22} (j_{N_2}/j_{N_1}) - D_{11}}{2 D_{12}} \quad (40)$$

In Fig. 6, the location of the critical nucleus as well as the predicted angle  $\phi$  is reported, indicating the direction of growth of the critical nucleus.

The nucleation rate appears to be very sensitive to the saturation ratio. For example, its value will be changed by several order of magnitude as the saturation ratio is changed by a few percents. Classically, a threshold value of the nucleation rate is arbitrarily chosen to represent the limit between finite rate nucleation and instantaneous nucleation. In this study, the limit is  $J = 10^{12} \text{ m}^{-3}\text{s}^{-1}$ ; this value is recommended for bubble nucleation<sup>1</sup>, whereas a value of  $J = 10^6 \text{ m}^{-3}\text{s}^{-1}$  is recommended for droplet nucleation. Despite its arbitrary nature, the limit value of the nucleation rate does not influence significantly the final results. In Fig. 5, the nucleation rate is reported as a function of the saturation ratio for different pressures, 20, 30, 40, 50 atm, respectively. In every case, the plot looks like a vertical line, so that the nucleation rate goes from  $10^0$  to  $10^{12} \text{ m}^{-3}\text{s}^{-1}$  for a change of a few percents of the saturation ratio. The threshold value of the nucleation rate cannot be related easily to a nucleation characteristic time,

through an expression like the following

$$\tau_{nucleation} = \frac{\rho_l}{m_{nucleus} J} \quad (41)$$

where  $\rho_l$  and  $m_{nucleus}$  represent the density of the superheat liquid and the mass of the critical nucleus, respectively. The definition of the nucleation rate is the rate of creation of critical nuclei per unit time and volume, those nuclei are unstable and tend to grow indefinitely. Thus, the characteristic time of nucleation is expected to be much shorter than the predictions issued from Eq (41) and, at the chosen kinetic limit of superheat, it is expected to be much shorter than any of the characteristic time involved in the droplet vaporization process.

In the Figs. 7-10, the ratio, for both oxygen and hydrogen, between the enthalpy of vaporization as a function of temperature under superheat conditions -for both the spinodal and the kinetic limit of superheat- and the enthalpy of vaporization at the saturation conditions

$$\Delta \bar{h}_i / \Delta \bar{h}_{i, sat} \quad (42)$$

is reported for different pressures, 20, 30, 40 and 50 atm, respectively. First, as it may have been expected *a priori*, the ratio of the enthalpies of vaporization becomes bigger at the spinodal limit. This limit, as was mentioned previously, constitutes a limit of thermodynamic stability and is never reached in principle. Let us focus our attention on the kinetic limit of vaporization. The behavior of the ratio of the enthalpies of vaporization depends strongly of the species considered. For oxygen, the ratio remains very close to 1, so that the relative difference is smaller than 10 %. On the other hand, for hydrogen, the ratio becomes very different from unity and tends eventually to diverge when the saturation temperature of pure oxygen is reached. Although this latter feature seems to show that non-equilibrium conditions have significant influence



on the droplet vaporization process, this feature must be balanced by the fact that, for the oxygen/hydrogen system, the ratio  $\dot{m}_{H_2}/\dot{m}$  is always negligible, as might have been deduced from Fig. 2. In fact, only the ratio of enthalpies of vaporization concerning oxygen should be considered. In this case, non-equilibrium conditions do not affect by more than 10 % the enthalpy of vaporization at the droplet surface. Therefore, the change in the predictions of droplet lifetime, under the occurrence of thermodynamic non-equilibrium conditions, would be smaller than 10 % with respect to the thermodynamic-equilibrium predictions.

The saturation ratio corresponding to the kinetic limit of superheat is reported for the considered pressures in Fig. 11. As the pressure is increased, the saturation ratio decreases, decreasing thus the difference between saturation conditions and superheat conditions. This leads to a ratio of enthalpies of vaporization closer to unity. Thus, the influence of thermodynamic non-equilibrium conditions drops to zero as pressure increases.

The analysis presented above may be criticized because of the somehow inaccurate hypotheses of modelization used. First, the Boltzmann's statistics has been used to estimate the dynamics of the molecules. However, the Boltzmann's statistics should be accurate enough so that the order of magnitude is not affected, and so should be the conclusions of the first part of this study. The molecular fluxes are also used to compute the nucleation rate. The expression of the nucleation rate is a product of the kinetic factor time an exponential factor. This latter factor has the greatest influence on the nucleation rate value, because as the liquid phase becomes more metastable, it increases from a very small value to an almost infinite value,<sup>9</sup> and finally any inaccuracy in the estimation of the kinetic factor may be not considered as dramatic.<sup>7,12</sup> Second, our

analysis is based on a thermodynamic modelization of both the bulk liquid and bubble gaseous phase issued from the Soave-Redlich-Kwong equation of state. This cubic equation of state has been demonstrated to lead to important error in the prediction of the liquid density near the saturation line.<sup>8</sup> However, since first and second derivatives of the primary thermodynamic variables are needed in the analysis, a relatively simple expression for the equation of state is needed. On one hand, one can argue that this may affect significantly the results, but one must keep in mind, on the other hand, that the best predictions of the droplet vaporization times are based on the same kind of thermodynamic modelizations.

## 4 Conclusion

A comprehensive analysis has been conducted concerning the influence of thermodynamic non-equilibrium conditions on the droplet vaporization process. The study has been restricted to the oxygen/hydrogen system, although the same kind of analysis may be conducted for other systems. First, the vaporization mass flow rates issued from droplet vaporization models based on the classical thermodynamic equilibrium assumption have been compared to the molecular fluxes. It has been shown that the molecular dynamics does not constitute a limiting factor for the reaching of the thermodynamic equilibrium at the interface, whatever the ambient temperature and pressure are, and as long as the droplet diameter is above 10  $\mu\text{m}$ . However, some uncertainties remain in the expression of the molecular fluxes, uncertainties essentially contained in the so-called accommodation coefficient. The second part of the analysis has been devoted to the case where molecular dynamics is not fast enough to sustain thermodynamic equilibrium, i.e. small droplet diameters or low accommodation coefficients.

The limit of occurrence of the resulting metastable liquid phase have been computed, both on a thermodynamic stability and on a kinetic limit viewpoints. It has been shown that, at the kinetic limit, the superheat liquid exhibits properties such that the enthalpy of vaporization of oxygen is only less than 10 % different from the saturation case. So that, under thermodynamic non-equilibrium conditions, the change in the droplet vaporization lifetime is expected to be negligible. In conclusion, it has been demonstrated that, as the pressure increases, first the thermodynamic equilibrium is most likely to be achieved, and, second, the influences of non-equilibrium conditions become smaller.

## References

- <sup>1</sup> Carey V.P. *Liquid-Vapor Phase-Change Phenomena*. Hemisphere Publishing Corporation, 1992.
- <sup>2</sup> Daou, J., Haldenwang, P., Nicoli, C. Supercritical Burning of Liquid (LOX) Droplet with Detailed Chemistry. *Combustion and Flame*, pages 153–169, 1995.
- <sup>3</sup> Graboski, M.S., Daubert, T.E. A Modified Soave Equation of State for Phase Equilibrium Calculations. 3. Systems Containing Hydrogen. *Industrial and Engineering Chemistry Process Design and Development*, 18(2):300, 1979.
- <sup>4</sup> Kai, T. Surface Tension of Ternary Mixtures of Nitrogen, Oxygen, and Argon. *Journal of Chemical and Engineering Data*, 39(3):499–501, July 1994.
- <sup>5</sup> Lafon, P. Modélisation et Simulation Numérique de l'Evaporation et de la Combustion de Gouttes à Haute Pression. *Thèse de doctorat, Université d'Orléans*, 1994.

- <sup>6</sup> Lafon, P., Yang, V., Habiballah, M. Supercritical Vaporization of Liquid Oxygen in Hydrogen and Water Environments. *Submitted to Journal of Fluid Mechanics*, 1995.
- <sup>7</sup> Looijmans, K.N.H. Classical Binary Nucleation Theory Applied to the Real Mixture *n*-Nonane/Methane at High Pressures. *Journal of Chemical Physics*, 102(11):4531, March 1995.
- <sup>8</sup> Reid, R.C., Prausnitz, J.M., Poling, E.P. *The Properties of Gases and Liquids*. Mac Graw Hill, New York, 4th edition, 1987.
- <sup>9</sup> Reiss, H. The Kinetics of Phase Transitions in Binary Systems. *Journal of Chemical Physics*, 18:840-848, 1950.
- <sup>10</sup> Schrage, R.W. *A Theoretical Study of Interface Mass Transfer*. Colombia University Press, New-York, 1953.
- <sup>11</sup> Stauffer, D. *Journal of Aerosol Science*, 7:319, 1976.
- <sup>12</sup> Wilemski, G. Revised Classical Binary Nucleation Theory for Aqueous Alcohol and Acetone Vapors. *Journal of Physical Chemistry*, 91:2492-2503, 1987.
- <sup>13</sup> Zeng, X.C. Binary Homogeneous Nucleation Theory for the Gas-Liquid Transition. A Nonclassical Approach. *Journal of Chemical Physics*, 95(8):5940, October 1991.

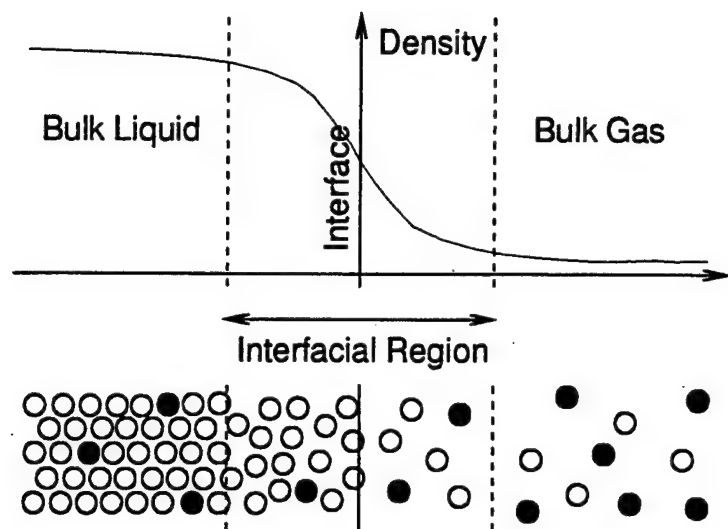


Figure 1: Schematic diagram of the interface between two bulk phases.

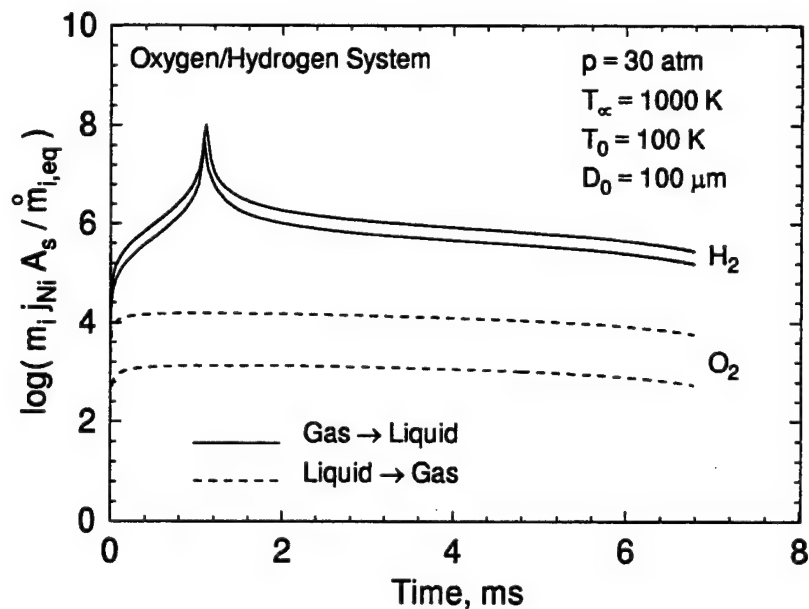


Figure 2: Comparisons between equilibrium net vaporization rates and molecular dynamics estimations; oxygen/hydrogen system;  $p = 30 \text{ atm}$ ,  $T_\infty = 1000 \text{ K}$ ,  $D_0 = 100 \mu\text{m}$ .

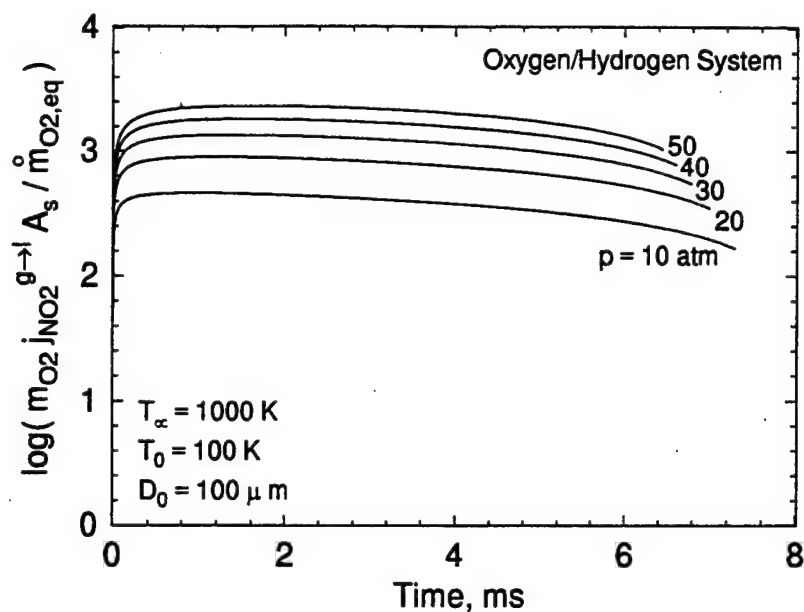


Figure 3: Comparisons between equilibrium net vaporization rates and molecular dynamics estimations at various pressures; oxygen/hydrogen system;  $T_{\infty} = 1000 \text{ K}$ ,  $D_0 = 100 \mu\text{m}$ .

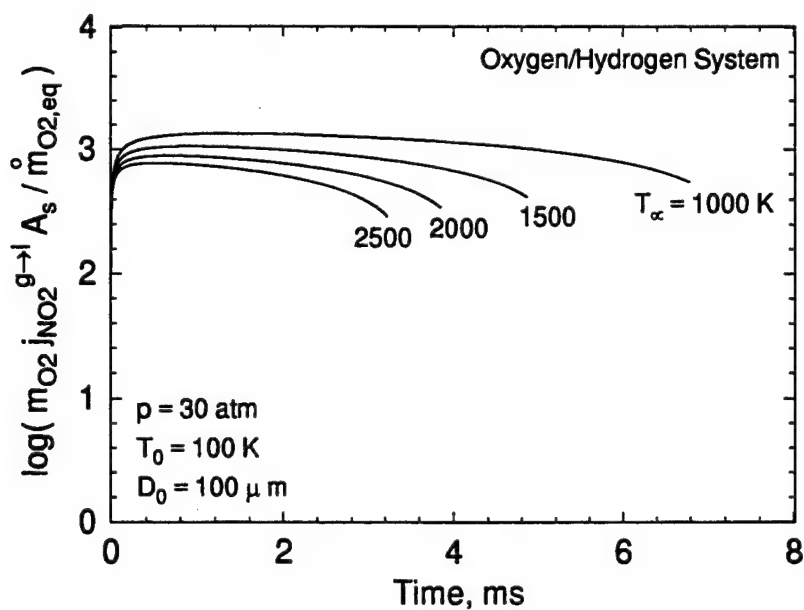


Figure 4: Comparisons between equilibrium net vaporization rates and molecular dynamics estimations at various ambient temperatures; oxygen/hydrogen system;  $p = 30 \text{ atm}$ ,  $D_0 = 100 \mu\text{m}$ .

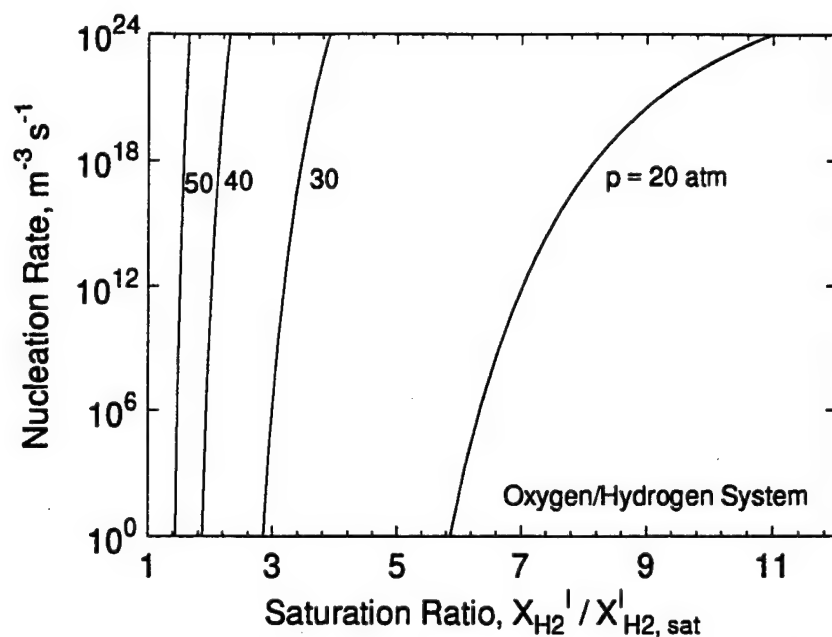


Figure 5: Nucleation rate as a function of the saturation ratio for various pressures; oxygen/hydrogen system; oxygen/hydrogen system;  $T = 100 \text{ K}$ .

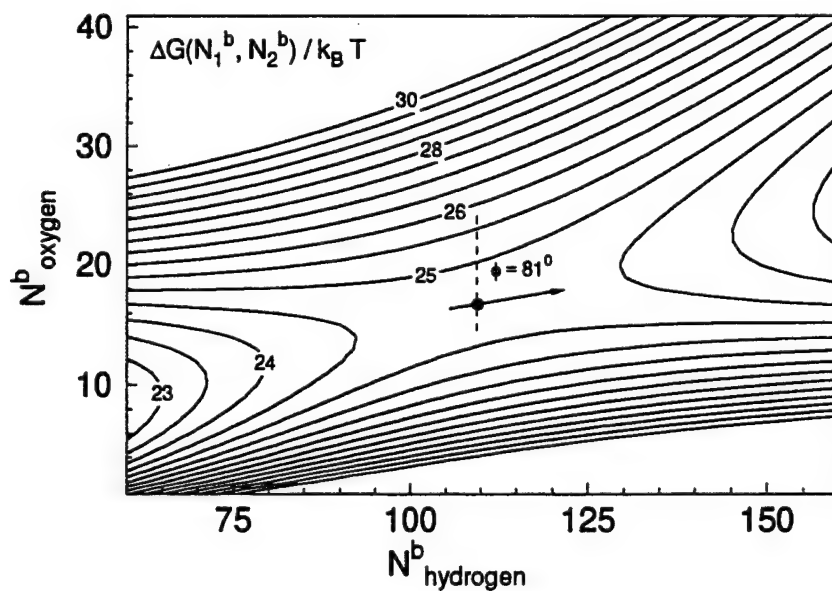


Figure 6: Contourplot of the Gibbs free energy in the vicinity of the saddle point;  $T_l = 110 \text{ K}$ ,  $p_l = 30 \text{ atm}$ ,  $S = 5$ .

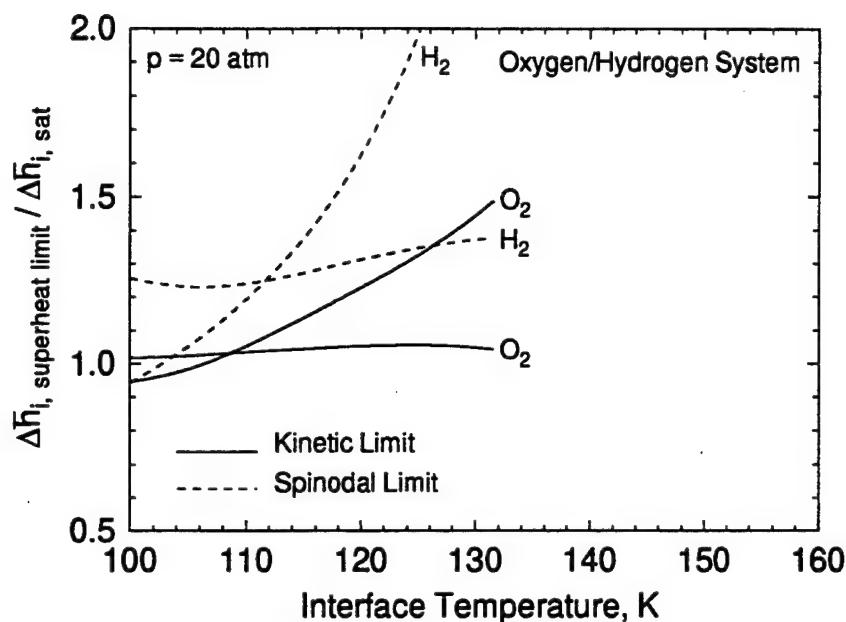


Figure 7: Enthalpy of vaporization at the spinodal and kinetic limit of superheat related to the enthalpy of vaporization at the saturation conditions; oxygen/hydrogen system;  $p = 20 \text{ atm}$ .

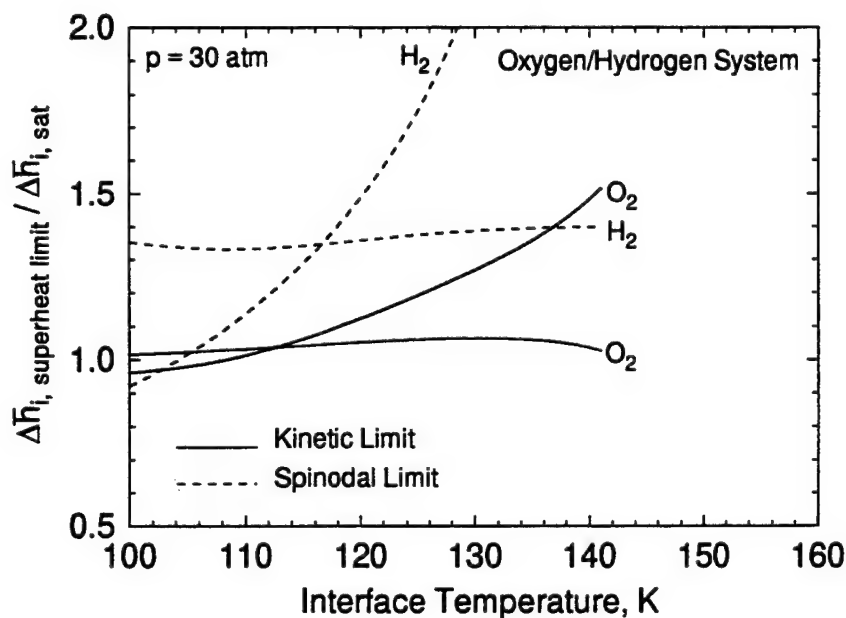


Figure 8: Enthalpy of vaporization at the spinodal and kinetic limit of superheat related to the enthalpy of vaporization at the saturation conditions; oxygen/hydrogen system;  $p = 30 \text{ atm}$ .



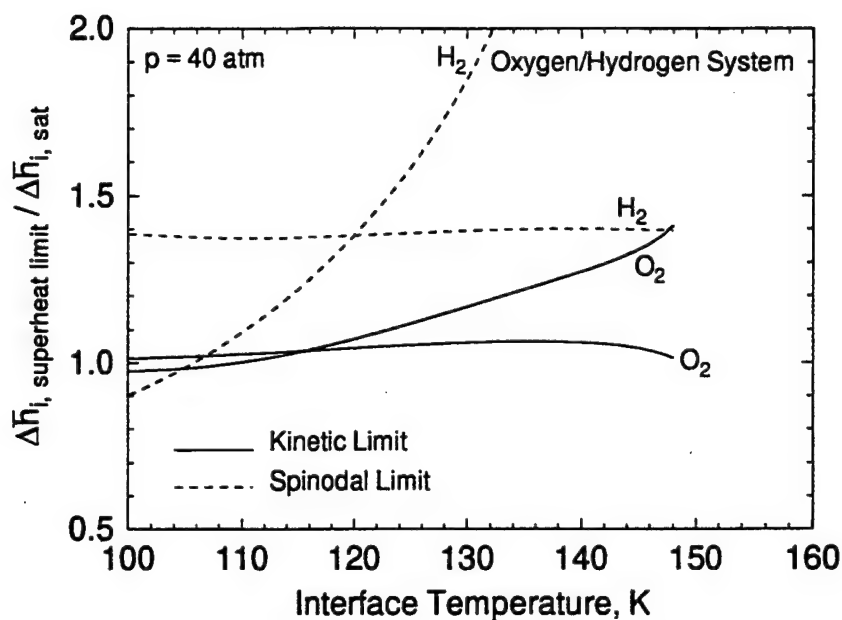


Figure 9: Enthalpy of vaporization at the spinodal and kinetic limit of superheat related to the enthalpy of vaporization at the saturation conditions as a function of temperature; oxygen/hydrogen system;  $p = 40 \text{ atm}$ .

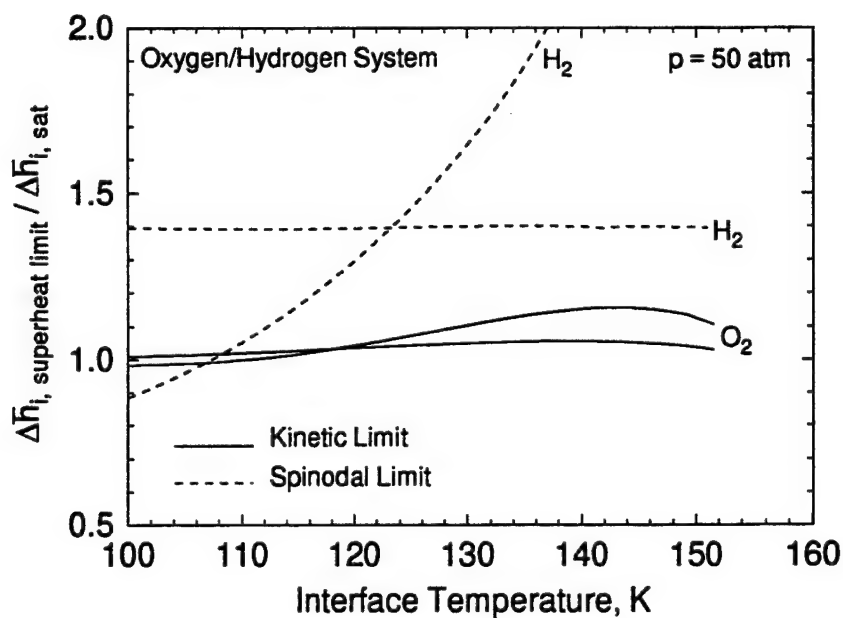


Figure 10: Enthalpy of vaporization at the spinodal and kinetic limit of superheat related to the enthalpy of vaporization at the saturation conditions as a function of temperature; oxygen/hydrogen system;  $p = 50 \text{ atm}$ .

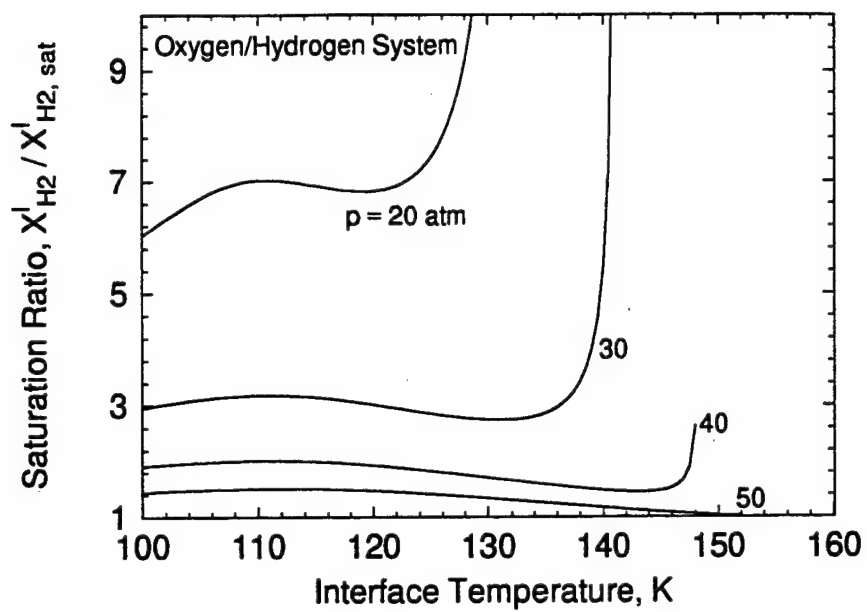


Figure 11: Saturation ratio as a function of temperature at the spinodal and kinetic limit of saturation; oxygen/hydrogen system;  $p = 20, 30, 40, 50 \text{ atm}$ .

# Pressure-Coupled Vaporization and Combustion Responses of Liquid Oxygen (LOX) Droplets in Supercritical Hydrogen Environments

Patrick Lafon\* and Vigor Yang†  
The Pennsylvania State University, University Park, PA 16802

Mohammed Habiballah‡  
Office National d'Etudes et de Recherche Aéronautique, 92322 Châtillon, FRANCE

## Abstract

This paper presents a numerical simulation of liquid-oxygen droplet vaporization and combustion under high pressure conditions in hydrogen quiescent atmospheres over a wide range of ambient conditions, including both subcritical and supercritical regimes. Theoretical modelization has been refined for thermodynamic behavior and transport properties estimations. In the case where gaseous water diffuses to oxygen droplet surface, a simplified condensation model has been implemented. In this paper, we focused our attention to droplet response to ambient pressure oscillations in terms of vaporization or combustion rate. Computations were carried out over a wide range of different ambient conditions for both pure-vaporization and combustion cases. Results can be applied to combustion instability studies of liquid rocket engines.

## Nomenclature

$a$  Equation of state constant in Eq.(11)

---

\*European Space Agency Post-Doctoral Fellow.

†Professor, Department of Mechanical Engineering, Associate Fellow AIAA.

‡Head, Division of Liquid Rocket Propulsion.

# Liquid Oxygen (LOX) Droplet Vaporization and Combustion in High-Pressure Hydrogen Environments with Pressure Oscillations

Patrick Lafon\* and Vigor Yang<sup>†</sup>  
The Pennsylvania State University, University Park, PA 16802

Mohammed Habiballah<sup>‡</sup>  
Office National d'Etudes et de Recherche Aéronautique, 92322 Châtillon, FRANCE

## Abstract

This paper presents a numerical simulation of liquid-oxygen droplet vaporization and combustion under high pressure conditions in hydrogen quiescent atmospheres over a wide range of ambient conditions, including both subcritical and supercritical regimes. Theoretical modelization has been refined for thermodynamic behavior and transport properties estimations. Both pure-vaporization and reactive cases have been investigated. In the case where gaseous water diffuses to oxygen droplet surface, a simplified condensation model has been implemented. In this paper, we focused our attention to droplet response to ambient pressure oscillations in terms of vaporization or combustion rate. The priority has been given to the understanding of the mechanisms involved in the droplet response, as well as to the special issues raised by high-pressure environments.

## Nomenclature

$a$	Equation of state constant in Eq.(11)
$A$	Surface area
$b$	Equation of state constant in Eq.(11)
$c$	Speed of sound
$C_p$	Constant-pressure specific heat
$D$	Droplet diameter
$D_{ij}$	Binary mass diffusion coefficient
$D_{im}$	Effective mass diffusion coefficient
$e$	Specific total internal energy
$F_T$	Thermophoretic force

---

\*European Space Agency Post-Doctoral Fellow.

<sup>†</sup>Professor, Department of Mechanical Engineering, Associate Fellow AIAA.

<sup>‡</sup>Head, Division of Liquid Rocket Propulsion.

$F_v$	Viscous force
$f$	Frequency
$\bar{h}_i$	Specific enthalpy of species $i$
$K_{vap}$	Vaporization kinetic coefficient in Eq.(21)
$\dot{m}$	Droplet mass evaporation rate
$N$	Number of species
$p$	Pressure
$q_e$	Energy diffusion flux
$q_i$	Mass diffusion flux of species $i$
$r$	Radial coordinate
$R$	Droplet radius
$R_p$	Response function
$R_u$	Universal gas constant
$S$	Saturation ratio
$v$	Velocity
$v_s$	Control surface moving velocity
$V$	Total volume
$V_i$	Diffusion velocity of species $i$
$X_i$	Mole fraction of species $i$
$Y_i$	Mass fraction of species $i$
$W$	Molecular weight
$Z$	Compressibility factor

### *Greek Symbols*

$\alpha$	Thermal diffusivity
$\alpha(T)$	Soave temperature function in Eq.(11)
$\lambda$	Thermal conductivity
$\mu_i$	Chemical potential of species $i$
$\nu_i$	Stoichiometric coefficient
$\rho$	Density
$\tau$	Droplet lifetime
$\omega$	Acentric factor
$\dot{\omega}_i$	Rate of production of species $i$

### *Subscripts*

$c$	Critical condition
$i$	Species $i$
$p$	Condensed particle
$r$	Reduced thermodynamic property
$rf$	Reference fluid
$sat$	Saturation value
$\infty$	Ambient condition

## Superscripts

$g$	Gaseous phase
$l$	Liquid phase
$0$	Dilute gas limit
$\cdot$	Time derivative
$'$	Fluctuation quantity
$-$	Averaged quantity
$*$	Dimensionless quantity

## 1 Introduction

This paper is concerned with liquid oxygen (LOX) droplet vaporization and combustion responses to ambient pressure oscillations. The ambient gas is composed of both hydrogen and water. In liquid rocket engines, propellants are injected into the combustion chamber as a spray of droplets which then undergo a sequence of vaporization, mixing and combustion processes. Each of these processes has been shown to play an important role in determining the instability characteristics. In this study, special attention has been given to the droplet behavior at high-pressure conditions.

In the past decade, several theoretical works have been developed to study droplet vaporization and combustion under high-pressure conditions. Most of them were numerical simulations concerning vaporization of either hydrocarbon droplets in air,<sup>1-3</sup> or liquid oxygen droplets in hydrogen environments.<sup>4-6</sup> By isolating the most important processes, these works have contributed to the comprehension of high-pressure droplet vaporization behavior, although some disagreements still exist among predictions, mainly due to the transport and thermodynamic modelization used. However, only a few numerical simulations were devoted to oscillating pressure conditions.<sup>7</sup>

Droplet vaporization and combustion have long been identified as a rate-controlling process for driving combustion instabilities in propulsion system. However, a quasi-steady response of the vaporization process to pressure oscillations cannot sustain the combustion instability. Many analyses<sup>8-11</sup> have been conducted and have shown that droplet vaporization response was small. Some of the hypotheses used in these models were criticized and might have altered the solution. A constant liquid temperature assumption could have kept the amplitude of vaporization response at low values. This assumption is questionable when the droplet heating time is longer than the droplet lifetime, which is the case for oxygen droplets vaporizing in hot hydrogen atmospheres. Recently, Sirignano *et al.*<sup>12-14</sup> have developed models which showed that droplet response amplitude is sufficiently large to sustain the instability. In addition, the effect of velocity fluctuation was shown to be more important than the one of pressure oscillations. These latter models were only applied to low-pressure situations.

The present work is concerned with the vaporization and combustion responses of liquid oxygen droplets in high-pressure hydrogen/water atmospheres. Since the model is one-dimensional, only the effect of pressure oscillations is investigated. The model cannot give a definitive answer on the role of vaporization in determining combustion instability, since the effect of velocity fluctuation is expected to be significant. However it gives insights into many important issues concerning the behavior of the oxygen/hydrogen system, for both low-pressure and high-pressure conditions. In the latter case, when the vaporization regime is supercritical, the droplet regression, and thus the vaporization

mass flow rate, is classically computed through the regression of a critical characteristic line, critical temperature, density, or composition. When interested in the droplet response to ambient pressure oscillations, this issue needs to be addressed carefully.

The numerical model is established on a solid foundation. An important effort has been devoted to transport and thermodynamic properties estimations. A unified treatment of thermal conductivity and molecular diffusion coefficient is presented. Thermodynamic properties are derived from the Soave-Redlich-Kwong equation of state in a self-consistent manner. In addition, a model for treating water condensation and its ensuing influence on droplet vaporization behavior is developed.<sup>15</sup>

In this paper, we first describe the theoretical formulation with emphasis on estimation on transport and thermodynamic properties. A condensation model is briefly discussed, followed by a summary of the numerical methods used in the present work. The model is first applied to vaporization of oxygen droplets in pure hydrogen environments in both subcritical and supercritical environments. The reactive case is then considered.

## 2 Theoretical Formulation

Figure 1 shows the situation examined here, an isolated LOX droplet vaporizing in a stagnant hydrogen/water environment with superimposed periodic pressure oscillations. Since buoyancy effects and forced convection are ignored, the problem is governed by a set of conservation equations in spherically symmetric coordinate. The following balance equations are written in their most general form. The initial droplet temperature is uniform and subcritical so that a well-defined interface in thermodynamical equilibrium exists at time zero.

### 2.1 Conservation Equations

Let us consider an arbitrary control volume  $V_a(t)$  delimited by a surface  $A_a(t)$  moving in an absolute referential at speed  $v_s$ . The mass balance equation may be written as follows:

$$\frac{d}{dt} \int_{V_a(t)} \rho dV + \int_{A_a(t)} \rho(v - v_s) \cdot d\mathbf{A} = 0 \quad (1)$$

The momentum and energy conservation equations are simplified with the following hypothesis: the velocities involved are very low so that the kinetic energy and viscous dissipation can be neglected. The momentum equation then reduces to the following:

$$\nabla p = 0 \quad (2)$$

Thus, when the ambient pressure oscillates, the droplet sees an environment with a uniform pressure distribution, but with a time-varying value. The uniform-pressure hypothesis is valid as long as the wave length of the pressure oscillation is far greater than the droplet diameter. Since the wave length is equal to the ratio of the speed of sound to the oscillation frequency  $c/f$ , the hypothesis loses its validity as frequency becomes very high.

The conservation of energy is derived by applying the first law of thermodynamics to the control volume

$$\frac{d}{dt} \int_{V_a(t)} \rho e dV + \int_{A_a(t)} \rho e(v - v_s) \cdot d\mathbf{A}$$

$$= - \int_{A_a(t)} p v \cdot dA - \int_{A_a(t)} q_e \cdot dA \quad (3)$$

The conservation of species is written as

$$\begin{aligned} & \frac{d}{dt} \int_{V_a(t)} \rho Y_i dV + \int_{A_a(t)} \rho Y_i (v - v_s) \cdot dA \\ &= - \int_{A_a(t)} q_i \cdot dA + \dot{\omega}_i \end{aligned} \quad (4)$$

## 2.2 Diffusion Fluxes

The diffusion fluxes of energy and mass,  $q_e$  and  $q_i$ , in Eqs.(3) and (4) need to be modeled. The Soret and Dufour effects, which account respectively for molecular diffusion due to temperature gradient and energy diffusion due to species-concentration gradient are not considered in the present analysis. Despite the disparity of molecular weight between hydrogen and oxygen and the high temperature gradients involved, these effects have been proven to be negligible at high pressure for oxygen droplet vaporization.<sup>15</sup> For diffusion fluxes, we derive the following formulas.<sup>16</sup>

$$q_e = -\lambda \nabla T - \sum_i^N q_i \bar{h}_i \quad (5)$$

$$q_i = \rho Y_i V_i = -\rho D_{im} \nabla Y_i \quad (6)$$

Fourier's and Fick's laws are used to approximate the thermal and molecular diffusion, respectively. The effective mass diffusion is obtained from the following equation in terms of binary mass diffusivity.<sup>17</sup>

$$D_{im} = (1 - X_i) / \sum_{i \neq j}^N (X_j / D_{ij}) \quad (7)$$

## 2.3 Gas-Phase Combustion Model

A finite-rate single-step irreversible chemical scheme,  $O_2 + 2 H_2 \rightarrow 2 H_2O$  is considered:

$$\dot{\omega}_i = \nu_i W_i Y_{O_2} Y_{H_2} A e^{(-E_a/R_u T)} \quad (8)$$

Combustion process is assumed to be faster than all the other mechanisms involved. Nominal values of  $A$  and  $E_a$  are thus chosen, so that they do not affect the solution.

## 2.4 Condensation of Water

When oxygen reacts with hydrogen, the main combustion product is water vapor. The water vapor diffuses from the flame towards the droplet surface. Water is much less volatile than oxygen and hydrogen. Consequently its liquid state exists for higher temperatures and pressures. Thus a non-negligible amount of gaseous water may reach a low temperature region where the water partial pressure becomes locally greater than its saturation pressure. Gaseous water may then experience phase change, leading to formation of ice/water particles. In the following analysis we consider that



gaseous water may experience only one phase change, that is condensation; transition from liquid to solid or direct transition from the gaseous to solid state is not considered.

The condensation mechanism involves an array of complex processes such as nucleation and particle growth by germination. In addition, particles may interact with the gaseous flow and other particles. The purpose here is not to treat the entire problem induced by condensation because it requires the development of a sophisticated spray model which may overlap our initial study set. All the processes involved in the condensation were analyzed, which enables to simplify the model.<sup>15</sup>

Since the nucleation process is faster than any other processes involved for realistic critical nuclei sizes, condensation is assumed to occur instantaneously when the saturation ratio ( $S = p_{H_2O}/p_{sat}$ ) is greater than unity. After their formation, the condensed particles interact with the gaseous flow according to thermophoretic and viscous forces. Heavier particles are attracted to low temperature regions due to thermophoretic effect, based on expressions for thermophoretic forces first derived by Epstein<sup>18</sup> and later corrected by Brock.<sup>19</sup> Since nuclei are typically of the order of the molecular mean free path, viscous forces were modeled using the Stokes-Cunningham equation which accounts for non-continuum effects coincident with water particles sizes of the molecular mean free path in the suspending fluid.<sup>20</sup> Assuming that thermophoretic and viscous forces are the only forces acting on the particle, the equation of motion describing particle dynamics can be written as:

$$\frac{4}{3}\pi R_p^3 \rho_p \frac{dv_p}{dt} = F_v + F_T \quad (9)$$

Actually a terminal velocity is reached when the net force acting on particles is equal to zero, that is when thermophoretic and viscous force are equal and opposite. The time needed to reach this mechanical equilibrium, which expression may be easily obtained and estimated for representative conditions, is by several order of magnitude smaller than the other representative times, so it is possible to consider that particle velocity is instantaneously equal to its terminal velocity given by:

$$v_{p,terminal} = v - \Theta \frac{1}{T} \frac{\partial T}{\partial r} \quad (10)$$

The expression of  $\Theta$  is function of particles radius, of the ratio of thermal conductivity for gaseous flow and water particles, gaseous viscosity, and of coefficients used in the expression of viscous forces. The influence of thermophoretic forces is rather small and terminal velocity is very close to gas phase velocity. Furthermore, since the particle radius effect is entirely included in this term, the overall effect of condensed particle size is then expected to be small or even negligible. A full treatment of water condensation process would require a different treatment of each condensed particle depending on its size. Since each particle would grow or decrease depending on the local saturation conditions, and since each particle may collide with other particles, tracking each particle size and position would necessitate a sophisticated modelization. From previous considerations, such modelization is unnecessary and all condensed particles are assumed to have the same radius, taken to be equal to  $10^{-2} \mu m$ .

The condensation process may then be reduced to the addition of mass sink term,  $-\dot{m}_{cond,H_2O}$  in the balance equation of mass, Eq.(1), and a source term,  $\Delta H_{vap,H_2O} \dot{m}_{cond,H_2O}$  in the balance equation of energy, Eq.(3). The clear parallelism existing between water condensation process and oxygen vaporization process leads us to express these terms with a method similar to that used for oxygen vaporization, which is described later in the text. Neglecting the contribution of Brownian motion of condensed particles to the pressure, we still can use Eq.(11) where  $\rho$  is the gas density.

Besides, we assume that the total volume is the sum of each phase volume. The condensed mass volume is related to its mass by the particle density, which is considered as independent of pressure and temperature.

## 2.5 Property Evaluation

Transport and thermodynamic properties play a decisive role in determining droplet vaporization behavior. The former dominates mass and energy transfer, whereas the latter affects the equilibrium conditions and energy needed for phase change. These properties dictate the conditions of occurrence of supercritical regimes, and as such, accurate predictions of thermodynamic and transport properties are needed. Furthermore, the property evaluation scheme must be the same for both liquid and gaseous phases to avoid consistency problem as the supercritical vaporization regime is reached.

### 2.5.1 Thermodynamic Properties

All the thermodynamic properties are derived from the Soave-Redlich-Kwong equation of state. It represents a good compromise between computation complexity and physical accuracy.<sup>5</sup> This equation of state takes the form:<sup>21</sup>

$$p = \frac{\rho R_u T}{(W - b\rho)} + \frac{a\alpha}{W} \frac{\rho^2}{(W + b\rho)} \quad (11)$$

where  $a$  and  $b$  are computed from classical mixing rules.  $a$  and  $b$  accounts for attractive forces and repulsive forces between molecules, respectively. All the thermodynamic properties required in the present analysis can be obtained by substituting Eq.(11) into appropriate thermodynamic relations.<sup>15</sup>

### 2.5.2 Transport Properties

Transport properties determine the mass and energy transport which dictate the interface conditions and consequently the vaporization rate and the occurrence of supercritical regimes. The major properties of interest are thermal conductivity, and mass diffusivity. Classical gas kinetic theory fails to predict correctly transport properties for high pressures. However it is always possible to estimate a low pressure value and then correct it by taking into account high-pressure effects.

For thermal conductivity we use the corresponding-state model proposed by Ely and Hanley.<sup>22,23</sup> This model is able to predict transport properties over a large domain of temperatures and pressures, from compressed liquid to dilute gas. The method requires the characteristic values of each species: critical coordinates and acentric factor. Details of the procedure may be found in the literature,<sup>23,24</sup> and only a brief summary is presented here. The mixture thermal conductivity is divided in two contributions as follows:

$$\lambda_m(\rho, T, Y_i) = \lambda'_m(T, Y_i) + \lambda''_m(\rho, T, Y_i) \quad (12)$$

$\lambda'_m(T, Y_i)$  represents the internal contribution to thermal conductivity, whereas  $\lambda''_m(\rho, T, Y_i)$  represents the translational and collisional parts. For a mixture the first term may be evaluated by means of an empirical mixing rule:

$$\lambda'_m = \frac{1}{2} \sum_i^N \sum_j^N X_i X_j \left( \frac{1}{\lambda'_i} + \frac{1}{\lambda'_j} \right)^{-1}, \quad (13)$$

in conjunction with the Eucken correlation modified for polyatomic gases:

$$\lambda'_i = 1.32 \mu_i^0 \left( C_{p,i}^0 - \frac{5}{2} \frac{R_u}{W_i} \right) \quad (14)$$

where the low pressure estimations of viscosity and specific heat are obtained from polynomial adjustments of existing experimental data.<sup>25</sup>

The collisional and translational part  $\lambda''_m(\rho, T, Y_i)$  is scaled to the correspondent property of the reference fluid using the extended corresponding-state method.

$$\lambda''_m(\rho, T, Y_i) = \lambda''_{rf}(\rho_{rf}, T_{rf}) \mathcal{F}_\lambda \mathcal{X}_\lambda \quad (15)$$

$\mathcal{F}_\lambda$  and  $\mathcal{X}_\lambda$  are the scaling factor and a correction factor respectively. The latter compensates the non-correspondent behavior of the mixture. For the reference fluid, the collisional and translational contribution of thermal conductivity is divided into three parts:

$$\begin{aligned} \lambda''_{rf}(\rho_{rf}, T_{rf}) &= \lambda^0_{rf}(T_{rf}) + \Delta\lambda_{exc}(\rho_{rf}, T_{rf}) \\ &+ \Delta\lambda_{crit}(\rho_{rf}, T_{rf}) \end{aligned} \quad (16)$$

$\lambda^0_{rf}(T_{rf})$  is the value at the dilute-gas limit for the reference fluid which may be evaluated by:

$$\lambda^0_{rf}(T_{rf}) = \frac{15R_u}{4W_{rf}} \mu^0_{rf}$$

$\Delta\lambda_{exc}(\rho_{rf}, T_{rf})$  and  $\Delta\lambda_{crit}(\rho_{rf}, T_{rf})$  correspond to the dense-fluid correction and the critical enhancement, respectively. They may be computed from analytical expressions fitted to experimental data. However, since properties which diverge strongly for pure components diverge only weakly for mixtures,<sup>26</sup> and the critical enhancement of thermal conductivity has not been observed for mixtures,  $\Delta\lambda_{crit}(\rho_{rf}, T_{rf})$  is not implemented in the present study.

Our desire to get a unified evaluation technique for mass diffusivity for both liquid and gaseous phases is inhibited for two reasons. First, such a technique does not exist in the literature, second, extension of existing modelizations valid one phase to the other may lead to erroneous errors. For gaseous phase, the approach proceeds in two steps. A low pressure binary mass diffusivity is first obtained using the Chapman-Enskog theory in conjunction with the Lennard-Jones intermolecular potential-energy function.<sup>25</sup> The coefficient is corrected with Takahashi correlation to take into account high pressure effects. Liquid diffusivity is estimated with the Wilke-and-Chang procedure. As the supercritical regime is reached, the estimation technique for liquids is applied for temperature below the mixture critical temperature. These methods are matched at the interface by using a correcting factor for the liquid estimation.

## 2.6 Interfacial Boundary Conditions

Before the surface temperature reaches the mixture critical value, thermodynamical phase equilibrium, characterized by a minimum of the Gibbs function, is assumed to prevail at the interface. If surface tension is neglected, equilibrium relations may be written as

$$\begin{cases} T^g &= T^l \\ p^g &= p^l \\ \mu_i^g &= \mu_i^l \end{cases} \quad (17)$$

The conservation of mass, species and energy across the interface are

$$\dot{m} = \rho(v - \dot{R})A|_{r=R_+} = \rho(v - \dot{R})A|_{r=R_-} \quad (18)$$

$$\dot{m}_i = [\dot{m}Y_i + q_i A]_{r=R_+} = [\dot{m}Y_i + q_i A]_{r=R_-} \quad (19)$$

$$-\lambda \nabla T|_{r=R_-} = -\lambda \nabla T|_{r=R_+} + \sum_i^N \dot{m}_i (\bar{h}_i^g - \bar{h}_i^l) \quad (20)$$

## 2.7 Numerical Methods

The set of equations, Eqs (1)-(4), is solved using a fully implicit scheme. Balance equations are discretized on a time varying grid with a finite volume formulation. Two different scenarios occur, depending upon whether the vaporization regime is subcritical or supercritical. In both cases the grid follows the time regression of droplet interface. In supercritical regimes the droplet interface is defined by the critical characteristic line (such as temperature, composition or density). For each grid cell, we compute the mass, the mass fraction of constituents, the internal energy and the cell volume. Cell volume is derived from homothetic transformation of the initial grid and by use of Eq.(18), for tracking droplet regression. Thermodynamic quantities such as pressure and temperature are computed by means of a linearization technique using partial derivatives of temperature, and pressure, respectively with respect to the computed quantities. Expressions of these partial derivatives are derived from Eq.(11). Details of the numerical method are presented in other publications.<sup>15,27</sup>

Let us discuss now the special numerical procedure used in the treatment of interfacial conditions in the subcritical regime. The transfer of each species involved in the thermodynamical equilibrium between the two phases is realized by using the following pseudo-phenomenological or kinetic-like relationship:

$$\dot{m}_i = K_{vap,i} (\mu_i^l - \mu_i^g) \quad (21)$$

This expression is comparable to phenomenological laws such as Fourier's law for heat conduction or Fick's law for mass diffusion. The flux is proportional to the difference of potential via the diffusion coefficient. To ensure thermodynamical equilibrium, the value of the vaporization kinetic coefficient is set so that the difference between the chemical potentials is as small as needed. This technique requires an implicit expression which is obtained by means of a linearization technique. The method does not need any sub-iterative process, but requires accurate expressions of chemical potential derivatives. Once the thermodynamical equilibrium is initiated, the interface evolves on a thermodynamical equilibrium trajectory. This evolution is controlled by heat and mass fluxes at the interface. As soon as the interface reaches the mixture critical conditions, this procedure is no longer applied, and the analysis switches to a single-phase approach.

## 3 Droplet Vaporization in Hydrogen

In this section, we consider the case of pure vaporization of LOX droplets in hydrogen environments. In this pure vaporization case, there is only one length scale, that is the initial droplet diameter. A dimensional analysis shows that any characteristic time of the process may be related to the

initial droplet diameter by means of a representative diffusivity.<sup>6</sup> It follows that the response of a droplet to pressure oscillations will be identical for different initial droplet diameters as long as the product  $f D_0^2$ , or  $f R_0^2$ , is kept constant. Figure 2 illustrates this point, the solid lines correspond to a constant product  $f D_0^2$  whereas the dots correspond to the computations which have been carried out for different ambient conditions. Thus, a frequency of 5,000 Hz for a 100  $\mu m$  droplet corresponds to a frequency of 555.5 Hz for a 300  $\mu m$  droplet.

In the present analysis, the initial droplet diameter is equal to 100  $\mu m$ , the amplitude of the pressure oscillation is 5 %. The initial droplet temperature is 90 K. For this non-reactive case we are interested in the fluctuation of the vaporization mass flow rate related to that of pressure, defined as the pressure-coupled vaporization function as follows:

$$R_p = \frac{\dot{m}'}{p'} = \frac{(\dot{m} - \bar{\dot{m}}) / \bar{\dot{m}}}{(p - \bar{p}) / \bar{p}} \quad (22)$$

The Rayleigh criterion may be simply stated: a wave will grow or decay if sufficient energy is added in phase with the pressure. If the reactive mechanism is assumed to occur without phase delay with respect to the vaporization process, the later criterion may be characterized by the real part of the previous response function, which must be positive to sustain instability. An estimation of this real part may be obtained by the following formula:

$$\Re[R_p(t)] = \frac{\int_{t-1/2f}^{t+1/2f} \dot{m}' p' dt}{\int_{t-1/2f}^{t+1/2f} p'^2 dt} \quad (23)$$

Let us first consider the case where the vaporization regime is subcritical. In Fig. 3, we present for three different pressures the time variations of the droplet vaporization mass flow rate fluctuation  $\dot{m}'$ . The ambient temperature is 1500 K, and the oscillation frequency is 5,000 Hz. For each pressure, the magnitude of the fluctuation first increases, then decreases slowly until the end of droplet lifetime. The amplitude of the fluctuation increases with increasing pressure. However, before reaching any conclusion, one must look at the phase angle between pressure and vaporization-rate fluctuations.

In this pure vaporization case, the process is entirely driven by transport phenomena with all the characteristic times being related to the square of the instantaneous droplet radius. Furthermore, since the droplet response is identical for a given value of  $f R_0^2$ , it is thus legitimate to relate droplet response to the product  $f R^2$ . This product may be non-dimensionalized by considering the liquid thermal inertia time  $\alpha_l = \lambda_l / \rho C_{pl}$ . Figures 4 and 5 show the magnitude and phase angle of droplet vaporization response in terms of  $f R^2 / \alpha_l$  and for  $\bar{p} = 30 \text{ atm}$ . First, the magnitude and the phase angle vary throughout the droplet lifetime. However, each of the presented curves collapses in the later stage of the droplet lifetime on a single curve, which is obviously a function of the product  $f R^2 / \alpha_l$ . As time goes, this product decreases because of the decrease in droplet radius, so that the curves presented in Figs. 4 and 5 are described from right to left as the droplet surface regresses. In the later stage of the droplet lifetime, the droplet response becomes a function of the instantaneous product  $f R^2 / \alpha_l$ . This feature demonstrates that steady conditions are reached and the vaporization mass flow rate fluctuates around the steady conditions value. The amplitude and phase angle of the response function depend only on the instantaneous value of  $f R^2 / \alpha_l$  for given ambient conditions.

As the magnitude is an increasing function of  $f R^2 / \alpha_l$ , the phase angle decreases, and finally becomes less than to  $-90^\circ$ , so that the real part of the response function becomes negative. In Fig. 6, we have reported the real part of the droplet vaporization response, the real part is computed either



by means of the two previous figures or by use of Eq.(23), both techniques gives consistent results, even though the droplet response is not perfectly sinusoidal. The real part shows a maximum for the product  $f R^2/\alpha_l$  being around 300. The cut-off value, above which the real part of the response function is negative, is around 3,000.

A phenomenological description of the droplet vaporization response to ambient pressure oscillation is difficult to obtain because many different physical processes interact with each other in a fully coupled manner. Furthermore, a simplified formulation of the mechanism, which will simplify the analysis, does not provide a satisfying description. However, some basic explanations can be provided by considering the droplet surface conditions in terms of temperature and composition as well as the liquid thermal diffusivity at the interface. First, although the ambient pressure, and thus the ambient temperature are oscillating, the interface temperature gradient on the gaseous side of the interface is only weakly affected by the pressure oscillation. This is also due to the fact that the characteristic time of the gaseous thermal inertia is much smaller than the period of the pressure oscillation. For similar reasons, the interface composition on the gaseous side is almost not affected by the pressure oscillation. As the pressure oscillates, the surface temperature oscillates so ensuring the interface thermodynamic equilibrium. This surface-temperature oscillation creates an oscillation of the enthalpy of vaporization and, thus, of the vaporization mass flow rate. The average interface temperature and pressure determines the magnitude of the oscillation of the enthalpy of vaporization. The closer the interface is to its critical conditions, the higher is the oscillation of the enthalpy of vaporization. This later oscillation controls the oscillation of the vaporization mass flow rate. It results that the average interface conditions exerts a significant control on the magnitude of the droplet response.

The liquid heat-up process influences both the magnitude and the phase of the droplet vaporization response. The heat flux hitting the surface is shared between the vaporization process and the liquid heat-up process. As the liquid thermal-inertia characteristic time,  $R^2/\alpha_l$ , decreases with respect to the oscillation period, the liquid phase absorbs the heat in its bulk volume and thus decreases slightly the magnitude of the surface temperature oscillation. However, this temperature oscillation is in phase with the pressure oscillation. On the contrary, as the product  $f R^2/\alpha_l$  increases, the absorption of the heat by the liquid phase is less easy. Thus, only the droplet surface absorbs the heat and with a non-negligible phase delay.

The oxygen/hydrogen shows a very different behavior compared to hydrocarbon/air systems. For *n*-pentane droplet vaporization in air, Hsiao *et al.*<sup>7</sup> showed that the cut-off value of  $f R^2/\alpha_l$  is much smaller, and about 200. The value at which the droplet response is maximum (i.e., the resonant value) is much also smaller. So there is an order-of-magnitude between both systems. Heidmann<sup>10</sup> predicted that the resonant frequency, frequency at which the maximum of the response occurs, for hydrocarbon systems is 6.5 smaller than that for oxygen droplets. However, Heidmann's work did not show any cut-off frequency for the oxygen/hydrogen system for the frequency range he considered, probably because he only considered values of  $f R^2/\alpha_l$  below 200.

One important difference between hydrocarbon and oxygen droplets is the ratio of droplet lifetime to liquid thermal-inertia time. For hydrocarbon/air systems, the droplet thermal-inertia time is of the same order of magnitude as the droplet lifetime. The temperature is almost uniform throughout the droplet interior in the later stage of the droplet lifetime, whereas for the oxygen/hydrogen system, at the end of the droplet lifetime, significant temperature gradients still exist within the droplet. By arbitrarily increasing liquid thermal conductivity, the cut-off frequency is shifted to a smaller value, further manifesting this feature. This also demonstrates that simplified analysis of Heidmann may not

be applied to oxygen/hydrogen system, since such a theory postulates that liquid thermal diffusivity is infinite and liquid temperature is uniform. The same observation was made by Sirignano *et al.*<sup>14</sup> by neglecting the liquid interior temperature gradients, the surface temperature oscillations will be restrained to unrealistically low values. In fact, the amplitude of oscillation is only slightly affected, but an increase of liquid interior thermal diffusivity tends to increase the phase lag, as mentioned previously. This causes the real part of the droplet response function to be drastically reduced and eventually becomes negative.

Figure 7, shows the real parts of the vaporization response function for three different mean pressures in the subcritical regime,  $p = 10, 30$  and  $50 \text{ atm}$ , respectively. Two important effects of pressure on droplet response are noted. First, as pressure increases, both resonant and cut-off values of  $f R^2/\alpha_l$  are increased. Second, the maximum value of droplet response increases with increasing pressure. The maximum value is even slightly above unity for  $p = 50 \text{ atm}$ . As pressure increases, the droplet surface temperature increases and becomes close to its critical value. The corresponding enthalpy of vaporization decreases and becomes more sensitive to temperature fluctuation. Consequently, as discussed previously, the vaporization mass flow rate oscillates in a more important way. In addition, for low pressure cases, the response functions collapse in an earlier stage of the droplet lifetime with the envelope curve, showing that transient stage occupies a smaller part of the droplet lifetime.

The effect of ambient temperature has also been investigated, with the results reported in Fig. 8. As temperature increases, the maximum value of droplet response is only weakly affected; however, the cut-off frequency is increased. The phase delay is reduced, with increasing temperature. As temperature increases, the droplet lifetime decreases, whereas the liquid thermal-inertia is almost unchanged. As mentioned previously, this feature tends to reduce the phase angle of the droplet response function.

We now consider supercritical pressures. An oxygen droplet, initially with a subcritical temperature distribution, is injected into a supercritical environment, such that the vaporization regime may transit from subcritical to supercritical. The interface conditions evolve rapidly so that the liquid and gaseous phase become identical at the interface. In previous works in steady vaporization, once the supercritical regime is reached, the interface was defined based on the locus of the critical mixing temperature. One other definition based on critical mixing composition was also used<sup>15</sup> to account for the mixing process. When this latter definition is chosen, the critical interface tends to move away from the liquid core, mainly because of the difference between mass and thermal diffusion rates (i.e. Lewis number is not equal to unity). In any case, it results from the previous remarks that the droplet regression characteristic time is of the same order-of-magnitude that the characteristic mixing time in the gaseous phase, either considering temperature diffusion or molecular diffusion, which are the two only mixing processes involved.

For low-pressure condition, a large difference exists between the physical characteristics of the liquid phase and those of the gaseous phase issued from the vaporization process. The difference in the density enables, in spray modelization, to treat the vaporizing droplets as source points of mass and sink points of energy. The difference in the characteristics of both phases leads to an order-of-magnitude difference between the gaseous mixing process and the droplet regression due to the vaporization process, so that the gaseous mixing process is handled by the spray model. Thus, for low-pressure situations, the droplet vaporization mass flow rate is an interesting and necessary input to any spray model. For supercritical vaporization regimes, no difference exists between the physical characteristics of the liquid phase and those of the gaseous phase issued from the vaporization

process. It results that the characteristic times of the gaseous mixing and of the droplet regression are of the same order-of-magnitude, as mentioned previously. Moreover, the absence of any disparity of density between both phases makes inappropriate the treatment of the droplets as source points of mass in a spray model under supercritical conditions. This is especially true when considering non-steady conditions of ambient pressure and velocity, where the droplet vaporization response is significantly affected by the somehow arbitrariness of the critical interface definition. However, numerical limitations prevent spray models to treat droplets without vaporization sub-models, thus it might be interesting to have some qualitative information about the droplet vaporization response to pressure oscillation under supercritical vaporization regime.

In this study, the critical interface is defined as the critical density line. As discussed previously, there is no good definition of the critical interface. Different critical interface definitions lead to significant change of the phase delay between the vaporization response and the pressure oscillation, but only slightly affect the magnitude of the response. The chosen definition leads to a behavior of the response which shares some common features with the sub-critical vaporization response, in term of phase angle. For supercritical regimes, vaporization mass flow rate is computed as the mass flux going through the critical interface.

Figure 9 shows the time evolution of mass vaporization rate fluctuation for two different ambient pressures of 100 and 200 atm, respectively. As pressure increases, the magnitude of the droplet response increases also. For a 5 % pressure oscillation amplitude, the maximum amplitude of mass vaporization rate fluctuation is around 10 % for 200 atm. No visible effect on the droplet vaporization is noticeable as the interface reaches its critical conditions mainly because it occurs in the very early stage of droplet lifetime. Figure 10 presents the real part of droplet response in terms of  $f R^2/\alpha_l$  for both pressures. The different curves correspond to various values of  $f R_0^2$ . Contrary to the subcritical case, those curves do not collapse on an envelope curve. The process becomes transient in nature throughout the entire droplet lifetime. At the beginning of the vaporization process, the response function reaches a maximum, between 1 and 2. For  $p = 200$  atm, the phase angle becomes very quickly smaller than  $-90^\circ$  so that the real part of the droplet response function becomes negative, although the amplitude of the mass vaporization rate fluctuation is higher, as shown in Fig. 9. This result is, however, very sensitive to the definition of critical interface and must be handled with care.

## 4 Droplet Combustion in Hydrogen

In this section, the combustion process between oxygen and hydrogen is considered. The oxygen droplet vaporizes in an atmosphere composed initially of both hydrogen and water. Ambient mass fractions of both hydrogen and water are arbitrary chosen to be 1/2. For droplet burning in quiescent atmospheres, the flame location is driven by the diffusion of reactants outside the flame, and by the value of the stoichiometric mixture ratio,  $\nu_{O_2} W_{O_2}/\nu_{H_2} W_{H_2}$ . In the oxygen/hydrogen system, the high values of the diffusion coefficient and stoichiometric mixture ratio render the flame to be close to the oxygen droplet surface. Thus, temperature gradients are important at the interface, which leads to a very thin condensation zone. However, condensation process is not negligible since it disables water to reach oxygen droplet surface.

After an initial transient, only oxygen is present at the interface: hydrogen is consumed at the flame, gaseous water condenses before reaching the droplet surface and condensed particles are blown away from the surface. Figure 11 demonstrates this feature by presenting the instantaneous distribu-



tions of species composition for the three species involved. The ambient mean pressure is  $p = 30 \text{ bar}$ . The spikes in the mass fraction of condensed water demonstrate that the condensation region is thin, and very close to the oxygen droplet surface. In subcritical gasification regimes, the surface temperature equals the oxygen saturation temperature corresponding to the instantaneous pressure. Our thermodynamic modelization is therefore not able to handle computational cases where ambient pressure oscillates around the critical pressure of oxygen. For such cases, the gasification regime will switch from a subcritical regime to a supercritical regime alternately.

In this reactive case, it is interesting to follow either gasification or burning response to pressure oscillations. The burning response is defined in a similar manner as the one depicted in Eq.(22) and with considering the burning mass flow rate, which is the rate of consumption of oxygen. Early theories were based on the assumption of quasi-steadiness of the gaseous phase, the mass burning rate was thus equal to the gasification rate. No vapor accumulation between the droplet surface and the flame were taken into account. In practice, vapor accumulation occurs, and consequently the flame stand-off ratio (i.e., ratio of flame radius to the instantaneous droplet radius) varies with time. Especially, at the end of droplet lifetime, this ratio becomes infinite during the time needed to burn the oxygen remaining inside the flame. This feature has also some important consequences considering both gasification and combustion response function. Figure 12 presents the time variations of the fluctuation of gasification and combustion rates for three different mean ambient pressures,  $\bar{p} = 10, 30, 40 \text{ atm}$  respectively. For the combustion case, the magnitude of the gasification response function increases with increasing pressure, although it is much smaller than for the pure vaporization case. However, the main interesting characteristic is the behavior of the combustion response. As one would expect, the burning response follows the vaporization with a phase delay. This delay may be simply related to the time needed for the oxygen vaporized at the droplet surface to reach the flame. If the acoustic time,  $1/f$ , becomes much greater than this characteristic time, combustion and gasification response should be in phase. But, the most significant feature of the combustion response function is its small amplitude compared to the gasification function. The diffusion flame properties may explain plausibly this point. As mentioned before, the location of the flame is determined by the diffusion of hydrogen towards the flame. On one hand, at the flame, the convection of oxygen from the droplet surface by the flow induced by the vaporization process is strongly influenced by the pressure oscillations. On the other hand, the diffusion of hydrogen, which feeds the flame, is almost not influenced by the pressure oscillations. There is thus an important damping in the combustion process provided by vapor accumulation and by the characteristics of the diffusion flame. Nevertheless, this is a specific feature of the one-dimensional formulation, the situation may be completely different under forced-convection conditions.

The magnitude of droplet combustion response is quite small, and its phase angle is almost always less than  $-90^\circ$ , so that the real part of droplet combustion response does not present any interesting aspects. Figure 13 reports the droplet gasification response for three different subcritical pressures. The droplet gasification response function shares some common features with the pure vaporization case. The real part increases with the average ambient pressure. However, for the range of the product  $fR_0^2$  investigated, neither maximum nor a cut-off value of the factor  $fR^2/\alpha_l$  is observed. Nevertheless, for the different cases simulated, the real part of the droplet gasification response remains small.

For ambient pressures above the oxygen critical pressure, the large temperature gradient induced by the combustion process allows the droplet surface to reach its critical conditions in the early stage of the droplet lifetime. Figure 14 reports the time evolution of the droplet gasification and

combustion responses for two supercritical pressure. The droplet response is similar to the subcritical regime case. The magnitude of droplet combustion response is much smaller than the corresponding gasification response. Besides, the reaction process responds with a more significant phase delay to pressure oscillations. One motivation of considering reactive cases was to overcome the difficulties encountered in the definition of critical interface for supercritical vaporization regimes, by analyzing droplet combustion response instead of gasification response. The former is insensitive to critical interface definition. However, since too much difference exists between these two droplet responses, comparing droplet gasification response to droplet combustion response for supercritical regime does not provide any interesting information, which might have justified *a posteriori* the definition of critical interface.

In Fig. 15, the real part of the droplet response is reported for two different supercritical ambient pressures. The behavior of the droplet response is different from the pure vaporization case at the same pressure. Contrary to the non-reactive case, after the initial period, the droplet response becomes a function of the instantaneous product  $fR^2/\alpha_l$ , regardless of the value of  $fR_0^2$ . This may be attributed to the fact that, contrary to the pure vaporization case, the temperature gradient at the droplet surface is almost time-constant, essentially because the flame location varies only weakly during most of the droplet lifetime. Once again, the droplet gasification response to pressure oscillations appears to be quite small.

## 5 Concluding Remarks

A comprehensive analysis of LOX droplet vaporization and burning response to ambient pressure oscillations in hydrogen and hydrogen/water environments at both sub- and supercritical conditions has been conducted. Special attention was given to evaluation of transport and thermodynamical properties. A sub-model was developed to treat the condensation of water vapor when it diffuses toward the oxygen droplet surface. Both pure vaporization and combustion cases were investigated. The sensitivity of results to the definition of critical interface has been discussed. In all the cases investigated in this study, the magnitude of the droplet vaporization response appears to be small although positive. Since only one-dimensional numerical simulations were carried out, only responses to pressure oscillation were analyzed. Droplet response to velocity fluctuations in a convective environment will be treated elsewhere.

### Acknowledgment

This research was supported in part by the European Space Agency, and in part by the US Air Force Office of Scientific Research with Dr. Mitat A. Birkan as the program manager.

## References

- <sup>1</sup> Hsieh, K.C., Shuen, J.S., Yang, V. "Droplet Vaporization in High-Pressure Environments 1: Near Critical Conditions," *Combust. Sci. and Tech.* vol. 76, 1991, 111-132.
- <sup>2</sup> Curtis, E.W., Farrel, P.V. "A Numerical Study of High Pressure Vaporization," *Combustion and Flame*, 1992, 85-102.

- <sup>3</sup> Shuen, J.S., Yang, V., Hsiao, C.C. "Combustion of Liquid-Fuel Droplets in Supercritical Conditions," *Combustion and Flame* vol. 89, 1992, 299-319.
- <sup>4</sup> Delplanque, J.P., Sirignano, W.A. "Transient Vaporization and Burning for an Oxygen Droplet at Sub- and Near-Critical Conditions," *AIAA Twenty-ninth Aerospace Sciences Meeting & Exhibit, Reno, NV* vol. 91-0075, 1991.
- <sup>5</sup> Yang, V., Lin, N.N., Shuen, J.S. "Vaporization of Liquid Oxygen (LOX) Droplets in Supercritical Hydrogen Environments," *Combustion Science and Technology* vol. 97, 1994, 247.
- <sup>6</sup> Daou, J., Haldenwang, P., Nicoli, C. "Supercritical Burning of Liquid (LOX) Droplet with Detailed Chemistry," *Combustion and Flame*, 1995, 153-169.
- <sup>7</sup> Hsiao, C.C., Yang, V., Shuen, J.S. "Pressure-Coupled Vaporization Response of Liquid Fuel Droplets at High Pressure," *Submitted to Journal of Propulsion and Power*, 1995.
- <sup>8</sup> Strahle, W.C., A Theoretical Study of Unsteady Droplet Burning: Transients and Periodic Solutions PhD thesis, Princeton University, 1960.
- <sup>9</sup> Priem, R.J., Guentert, D.C. "Combustion Instability Limits Determined by a Nonlinear Theory and a One-Dimensional Model," Technical report, NASA TN D-1409, 1962.
- <sup>10</sup> Heidmann, M.F. Wieber, P.R. "Analysis of *n*-Heptane Vaporization in unstable Combustor with Travelling Transverse Oscillations," Technical report, NASA TN D-3424, 1965.
- <sup>11</sup> HARRJE, D.T., REARDON, F.H., Ed. Liquid Propellant Rocket Combustion Instability NASA SP-194, Washington, D.C., 1972.
- <sup>12</sup> Tong, A.Y., Sirignano, W.A. "Oscillatory Vaporization of Fuel Droplets in an Unstable Combustor," *Journal of Propulsion and Power* vol. 5, 1989, 257-261.
- <sup>13</sup> Bathia, R., Sirignano, W.A. "One-Dimensional Analysis of Liquid-Fueled Combustion Instability," *Journal of Propulsion and Power* vol. 7, 1991, 953-961.
- <sup>14</sup> Sirignano, W.A., Delplanque, J.-P., Chiang, C.H., Bhatia, R. "Liquid-Propellant Droplet Vaporization: a Rate-Controlling Process for Rocket Combustion Instability," *AIAA Progress in Astronautics and Aeronautics*, September 1995.
- <sup>15</sup> Lafon, P., Yang, V., Habiballah, M. "Supercritical Vaporization of Liquid Oxygen in Hydrogen and Water Environments," *Submitted to Journal of Fluid Mechanics*, 1995.
- <sup>16</sup> Williams, F.A., Combustion Theory, 2nd ed. The Benjamin/Cummings Publishing, Inc., 1985.
- <sup>17</sup> Bird, R.B., Stewart, W.E., Lightfoot, E.N., Transport Phenomena John Wiley & Sons, Inc., New York-London, 1960.
- <sup>18</sup> Epstein, P.S., *Z. Phys.* vol. 54, 1929, 537.
- <sup>19</sup> Brock, J.R. "On the Theory of Thermal Forces Acting on Aerosol Particles," *Journal of Colloid Science* vol. 17, 1962, 768-780.

- <sup>20</sup> Carlson, D.J., Haglund, R.F. " Particle Drag and Heat Transfer in Rocket Nozzles," *AIAA Journal* vol. 2, 1964, 35-58.
- <sup>21</sup> Graboski, M.S., Daubert, T.E. " A Modified Soave Equation of State for Phase Equilibrium Calculations. 3. Systems Containing Hydrogen," *Industrial and Engineering Chemistry Process Design and Development* vol. 18, no. 2, 1979, 300.
- <sup>22</sup> Ely, J.F., Hanley, H.J.M. " Predictions of Transport Properties. 1. Viscosity of Pure Liquids and Mixtures," *Industrial and Engineering Chemistry Fundamentals* vol. 20, no. 4, 1981, 323.
- <sup>23</sup> Ely, J.F., Hanley, H.J.M. " Predictions of Transport Properties. 2. Thermal Conductivity of Pure Liquids and Mixtures," *Industrial and Engineering Chemistry Fundamentals* vol. 22, no. 4, 1983, 90.
- <sup>24</sup> Hsiao, C.C., Yang, V., Shuen, J.S. " Vaporization of Liquid Oxygen (LOX) Droplets in Supercritical Hydrogen Convective Environments," *Submitted to Journal of Fluid Mechanics*, 1995.
- <sup>25</sup> Reid, R.C., Prausnitz, J.M., Sherwood, T.K., *The Properties of Gases and Liquids*, 3rd ed. Mac Graw Hill, New York, 1977.
- <sup>26</sup> Bruno, T.J., Ely, J.F., *Supercritical Fluid Technology: Reviews in Modern Theory and Applications* CRC Press, Inc., Boca Raton, 1991.
- <sup>27</sup> Lafon, P. " Modélisation et Simulation Numérique de l'Evaporation et de la Combustion de Gouttes à Haute Pression," *Thèse de doctorat, Université d'Orléans*, 1994.

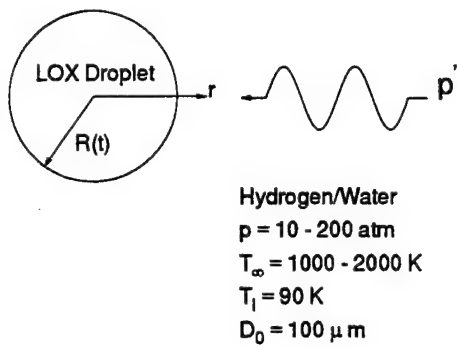


Figure 1: Schematic of a vaporizing LOX droplet in hydrogen and water environments and pressure oscillations.

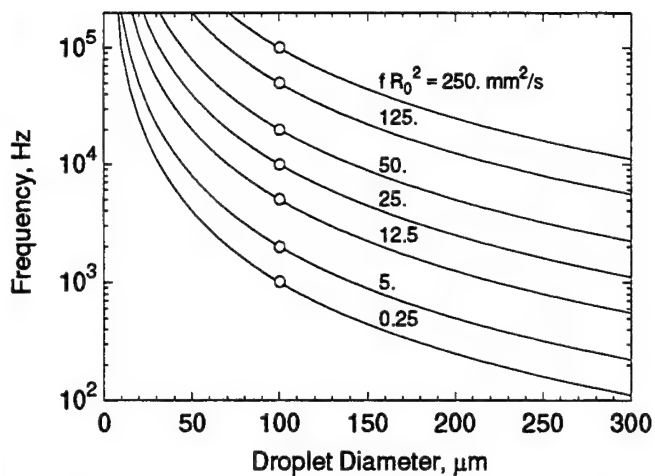


Figure 2: Frequency function of initial droplet diameter for different computational cases.

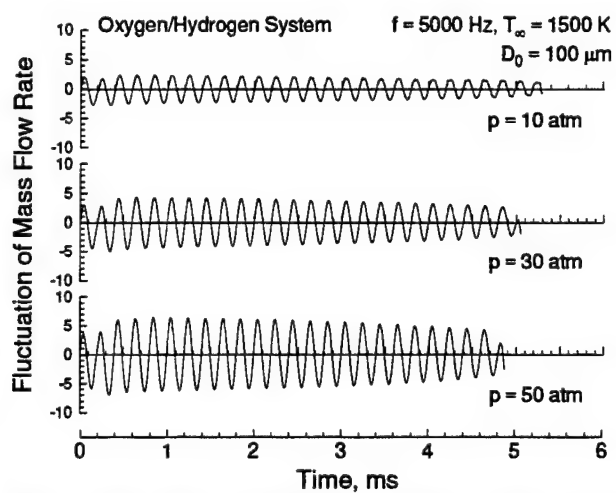


Figure 3: Time variations of fluctuation of vaporization mass flow rate for different pressures.

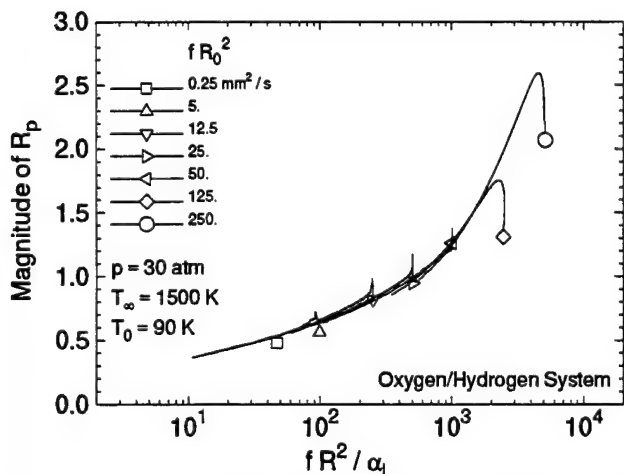


Figure 4: Magnitude of droplet vaporization response function;  $p = 30 \text{ atm}$ .

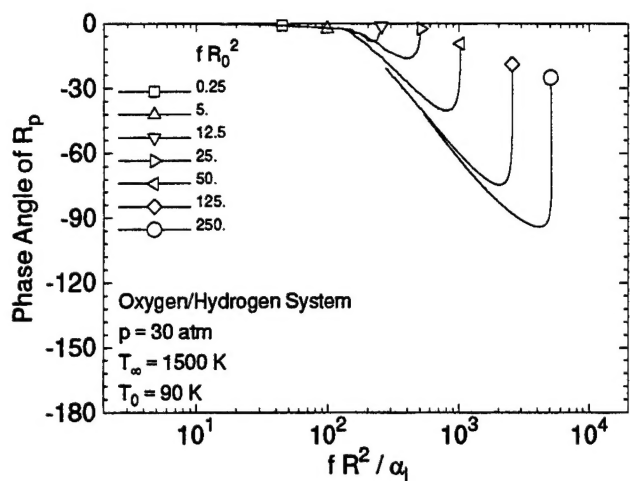


Figure 5: Phase angle of droplet vaporization response function;  $p = 30 \text{ atm}$ .

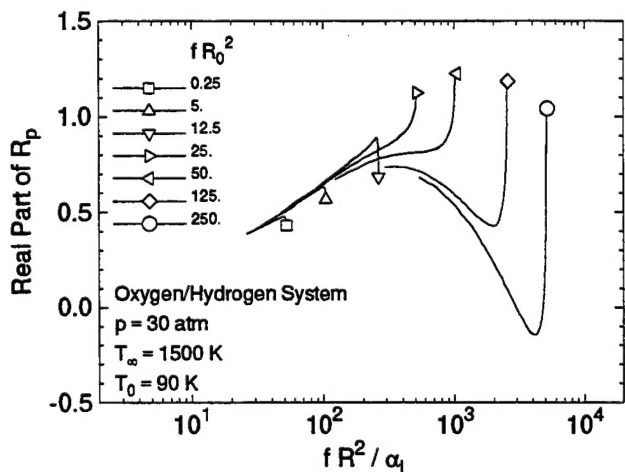


Figure 6: Real part of droplet vaporization response function;  $p = 30 \text{ atm}$ .

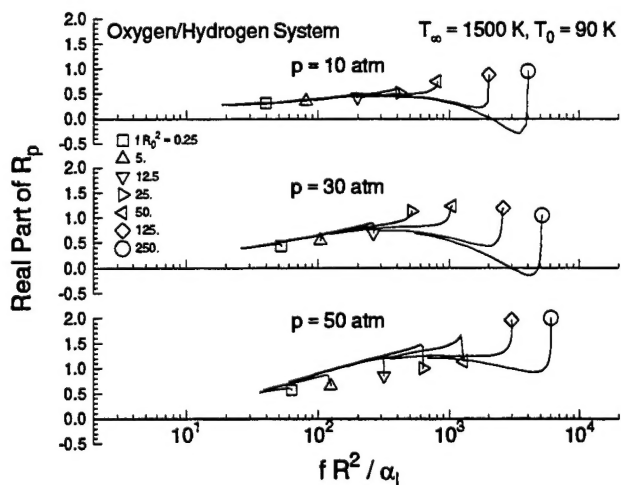


Figure 7: Real parts of droplet vaporization response function for three different mean pressures; subcritical vaporization regime.

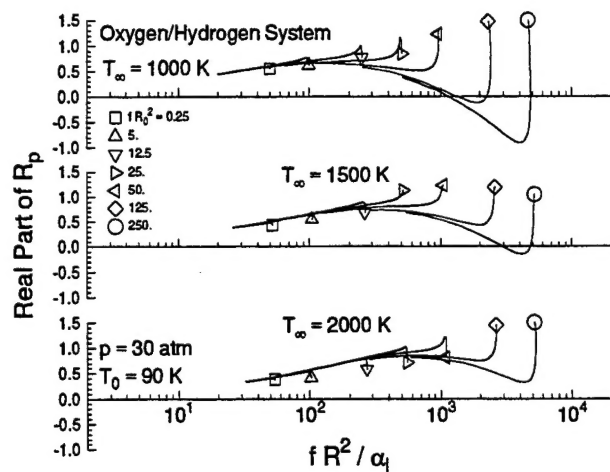


Figure 8: Real part of droplet vaporization response function for three different ambient temperatures;  $p = 30$  atm.

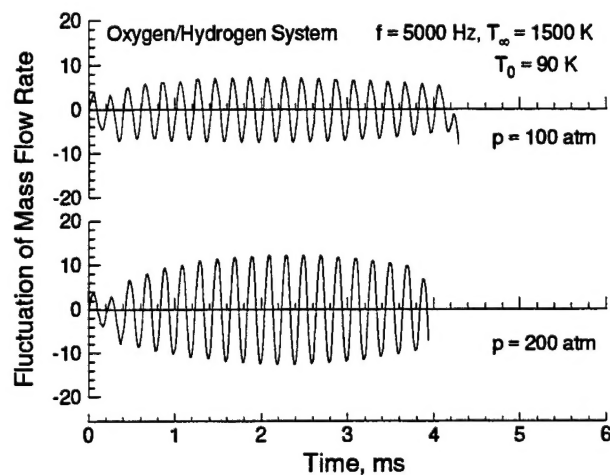


Figure 9: Time variations of fluctuation of vaporization mass flow rate for different mean pressures; supercritical vaporization regime.

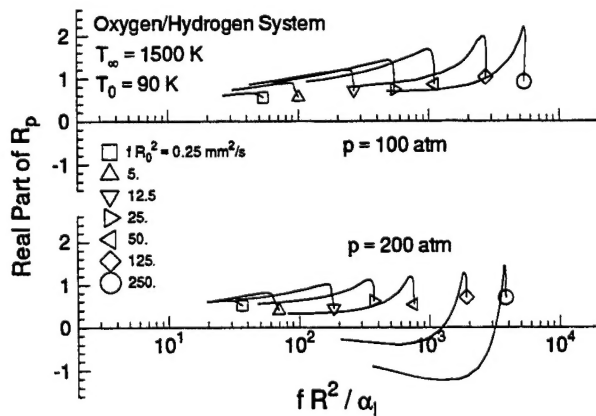


Figure 10: Real part of droplet vaporization response function; supercritical regime of vaporization.



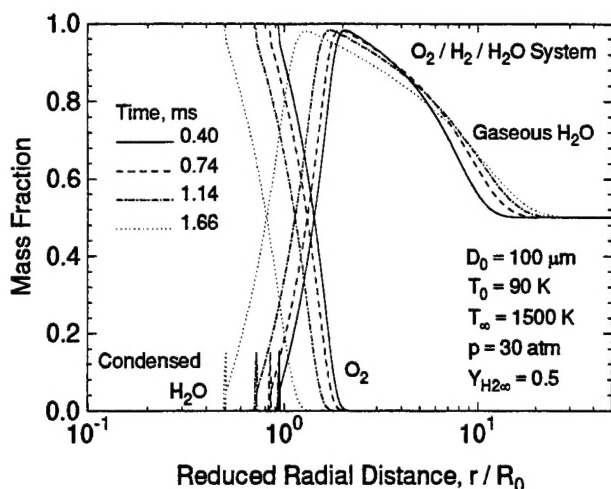


Figure 11: Instantaneous distributions of species compositions in the entire field for various times, LOX/H<sub>2</sub>/H<sub>2</sub>O system.

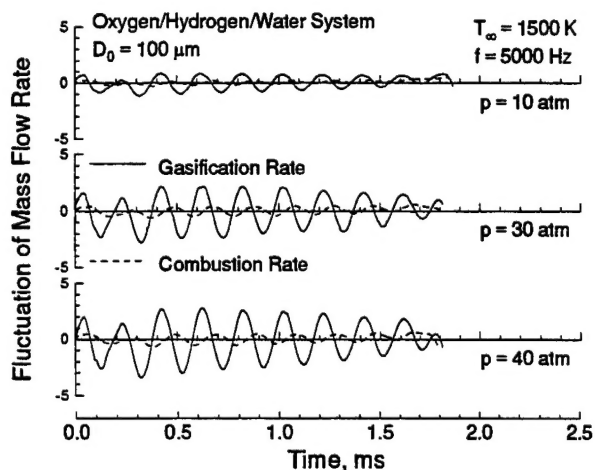


Figure 12: Time variations of the fluctuation of gasification and combustion rates for different pressures; LOX/H<sub>2</sub>/H<sub>2</sub>O system; subcritical gasification regime.

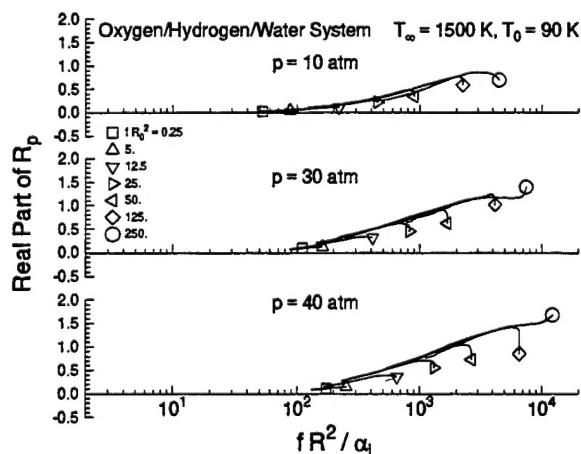


Figure 13: Real part of droplet gasification response function for different pressures; subcritical gasification regime.

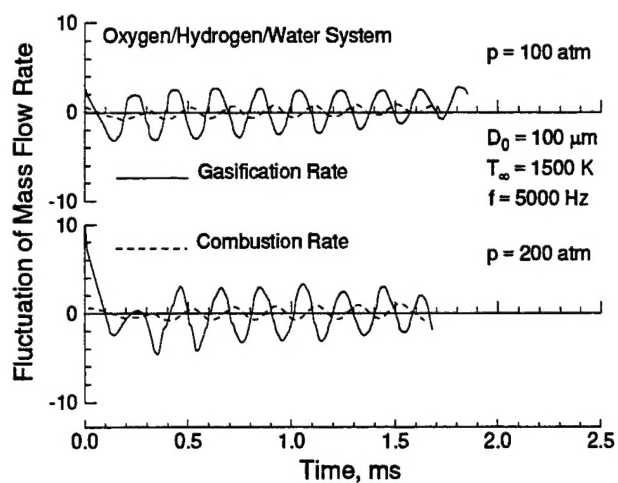


Figure 14: Time variations of fluctuation of gasification and combustion rates for different pressures; supercritical gasification regime.

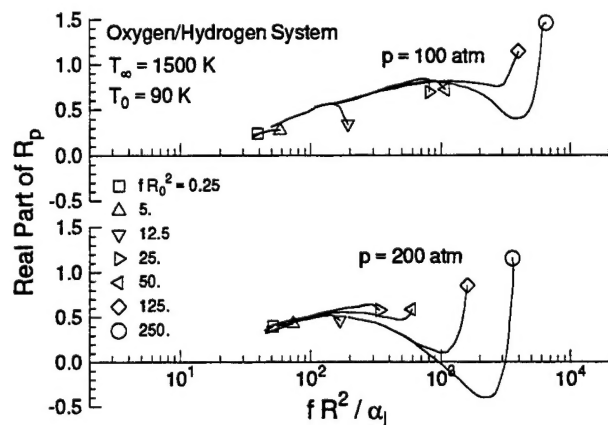


Figure 15: Real part of droplet gasification response function for different pressures; supercritical gasification regime.